R-717
CU-286
NEVIS-182

Nevis Laboratories
Columbia University
Physics Department
Irvington-on- Hudson
New York

A Search for Evidence of $\omega \to \pi^+\pi^-$ in $\pi^- p \to \pi^+\pi^- n$ and a Study of the $\omega \to \pi^+\pi^-\pi^0$ Dalitz Plot

THOMAS NASH

Reproduction in whole or in part
is permitted for any purpose of the
United States Government

Submitted in partial fulfillment of
the requirements for the degree
of Doctor of Philosophy in the Faculty
of Pure Science, Columbia University

FERMILAB
LIBRARY

1970

United States Atomic Energy Commission
Contract AT(30-1)-1932 Task I

Main AAF-5091
Dept 40078286

Nach Christi geburt/1513 Jar Adi 1. May hat man dem grossmechtigisten König Emanuel von Portugal/gen Lysabona aus India pracht/ ain solch lebendig Thier. das nennen sie Rhinocerus/Das ist hie mit all seiner gestalt Aconterfect. Es hat ein farb wie ein gepfreckelte schildkrot/vnd ist von dicken schalen vberleget sehr fest/vnd ist in der grösse als der Heilffandt/aber niderichter von baynen vnd sehr wehrhafftig es hat ein scharffstarck Horn vorn auff der Nassen /das begundt es zu wetzen wo es bey staynen ist / das da ein Sieg Thir ist/des Heilffandten Todtfeyndt. Der Heilffandt fürchts fast vbel /den wo es Jhn ankompt/so laufft Jhm das Thir mit dem kopff zwischen die fordern bayn /vnd reist den Heilffanten vnten am bauch auff/vnd er würget jhn des mag er sich nicht erwehren. dann das Thier ist also gewapnet/das jhm der Jelffandt nichts Thun kan/Sie sagen auch/das der Rhinocerus/Schnell/frayng/vnd auch Lustig / sey.

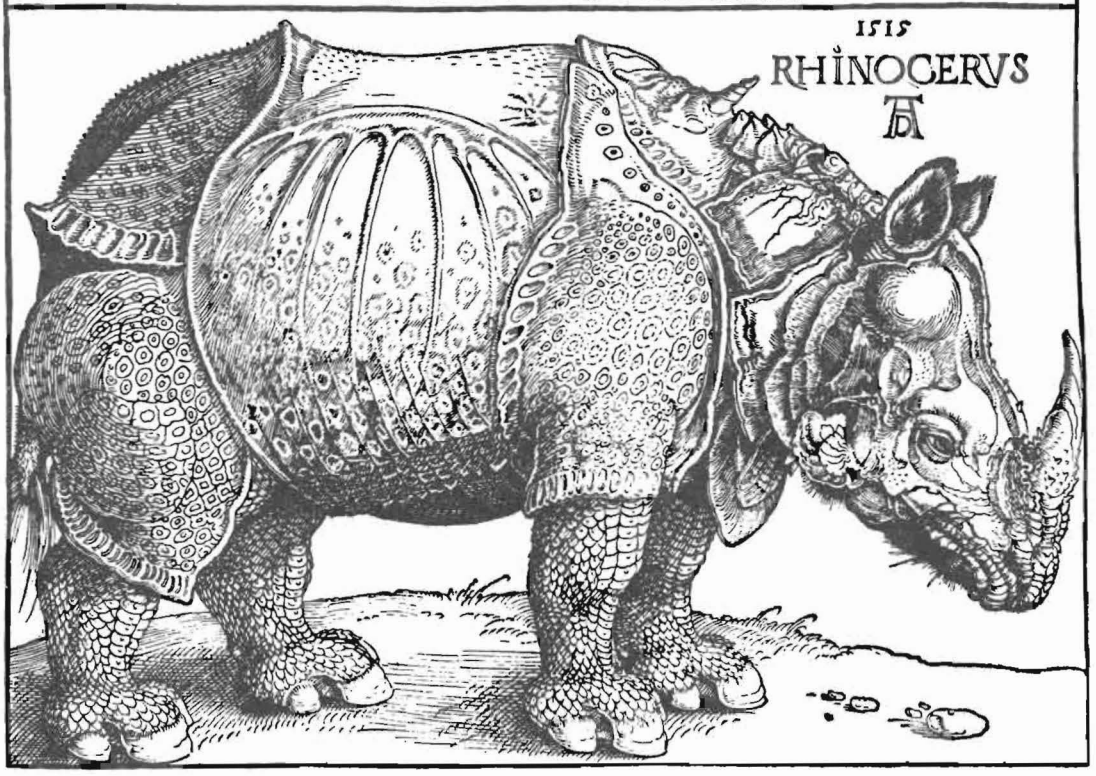

A Search for Evidence of $\omega \to \pi^+\pi^-$ in $\pi^- p \to \pi^+\pi^- n$ and a Study of the $\omega \to \pi^+\pi^-\pi^0$ Dalitz Plot

THOMAS NASH †

Columbia University, New York, N.Y.

---

* Research supported in part by the United States Atomic Energy Commission.

† Submitted in partial fulfillment of the requirements for the degree of Doctor of Philosophy in the Faculty of Pure Science, Columbia University.

ABSTRACT

We have searched for evidence of $\omega \to \pi^+\pi^-$ in a sample of 9696 $\pi^- p \to \pi^+\pi^- n$ events taken at a beam momentum of 1245 MeV/c. We have measured the branching ratio, $B = N_{\omega\to 2\pi}/N_{\omega\to 3\pi}$ for a series of assumptions of ρ-ω coherence and relative phase angle, ϕ. The results set upper limits at the 90% confidence level of $B < 2.9\%$ for incoherence, $B < 17.9\%$ for coherence and destructive interference ($\phi = +\frac{\pi}{2}$), $B < 0.51\%$ for constructive interference ($\phi = -\frac{\pi}{2}$), and $B < 3.0\%$ for $\phi = \pi$. We have also measured the Dalitz plot asymmetry of an accompanying sample of about 7600 $\omega \to \pi^+\pi^-\pi^0$ events in $\pi^- p \to \pi^+\pi^-\pi^0 n$ to be $A = -0.014 \pm 0.028$. The non-resonant background was subtracted from these data in 28 independent Dalitz plot regions. The Dalitz plot distribution of the ω events agrees very well with the simplest matrix element for a $J^P = 1^-$ particle and shows no evidence of any rho dominance effects.

I. INTRODUCTION

The possibility that omega decays to two pions was suggested first by Glashow in 1961[1] shortly after the vector meson was first observed by Maglic et al.[2] Omega was observed to decay heavily to 3π through the strong interactions and so its G parity[3] was known to be negative at a very early stage. A decay to 2π would violate G parity and isotopic spin and would be forbidden under the strong interactions. But it was quickly noticed by Glashow[1] and Nambu and Sakurai[4] and Feinberg,[5] and others that the mass of the ω (m_ω = 783.4 MeV, Γ_ω = 12.2 MeV) was very close to the mass of another new vector meson, the ρ (m_ρ = 765 MeV, $\Gamma_{\rho o}$ = 125 MeV). In fact, ρ is so wide that the narrow ω would sit right on top of the ρ if it decayed to 2π. These theorists suggested that since the only essential quantum number difference between ρ and ω is G parity or I spin, the electromagnetic interaction cannot distinguish between the two particles and electromagnetic transitions between ρ and ω are allowed and likely. They suggested that this would raise the likelihood of $\omega \rightarrow 2\pi$ significantly.

Many searches for evidence of ω in the 2π mass spectrum were made. The first significant statistical sample was obtained when Lütjens and Steinberger compiled all the early results.[6] These authors were aware of the ρ-ω interference problem (to be discussed shortly), and of the fact that when they cited upper limits on the branching ratio

$$B = N_{\omega\to 2\pi}/N_{\omega\to 3\pi}$$

based on the compilations, these upper limits depended on the assumptions made about coherence of ρ and ω production. Their result, assuming complete incoherence, was $B < 0.008$ with 90% confidence.

In 1966, Flatte et al reported evidence of a possible $\omega \to 2\pi$ effect in a new high statistics sample observed in the single reaction[7]

$$K^- p \to \Lambda\omega \ .$$

Their recently[8] revised conclusion is that $B > 0.002$ but that no upper limit may be set without assumptions about coherence.

In this experiment, we search for evidence of $\omega \to 2\pi$ in $\pi^- p \to \pi^+\pi^- n$. Before describing this experiment and citing other recent results on the subject, we will prepare a theoretical framework for the experimental analysis of later sections. The various historical approaches to the problem of $\omega \to 2\pi$ can be shown to be essentially equivalent.[9] We will follow here the ω-ρ mass mixing scheme which shows the equivalence of this problem with the K_1K_2 system. This approach was first used (for the ω-ρ problem) by Bernstein and Feinberg in 1962.[10,11]

A. Theory of ω-ρ Mixing

When dealing with the K_1-K_2 problem, one is interested in the time development of a given combination of K_o and $\bar{K}_o$. For this reason, the mixing is dealt with by starting with a

set of coupled Schroedinger equations that connect the two states of interest, amplitudes a_K and $a_{\bar{K}}$, and all other available states. The problem may be treated in a way similar to that used by Wigner and Weisskopf for atomic states[11] if one first assumes an exponential time dependence for a_K and $a_{\bar{K}}$, $e^{\gamma t}$, and then, in sums over the energy of connecting states, neglects the widths of the states compared with their energies. The problem is thus reduced to a two dimensional eigenvalue equation,

$$\underset{\sim}{M}\begin{pmatrix} a_K \\ a_{\bar{K}} \end{pmatrix} = \gamma \begin{pmatrix} a_K \\ a_{\bar{K}} \end{pmatrix} \tag{1}$$

where

$$\underset{\sim}{M} = \begin{pmatrix} m_1 + i\,\frac{\Gamma_1}{2} & -\delta_{12} \\ -\delta_{21} & m_2 + i\,\frac{\Gamma_2}{2} \end{pmatrix}$$

The elements of $\underset{\sim}{M}$, which we will call the mass matrix, are related to the elements of the Hamiltonian which connect the states 1 and 2 to the continuum of states. The eigenvalue equation may be solved to obtain the time dependence in the problem. In this experiment, however, we are dealing with particles of such short lifetime that we have no experimental interest in the actual time dependence. Rather we wish to know the form of the energy spectrum of the two pions which contains all the experimentally available information on the problem. Following Bernstein and Feinberg[10], we could obtain the energy dependence as the Fourier transform of the time dependence. Another approach is to start with a propagator equation for

the 2π production amplitude. The propagator is just the Fourier transform of the Green's function of the relativistic Schroedinger equation $(P^2 \underset{\sim}{1} - \underset{\sim}{M}^2)\underset{\sim}{\Psi} = 0$, where the four momentum operator $P = P_{\pi+} + P_{\pi-}$ and $\underset{\sim}{1}$ is the unit matrix. In this way, we may include in the 2π production amplitude the ρ and ω production amplitudes,

$$\underset{\sim}{A} = \begin{pmatrix} A_\rho \\ A_\omega \end{pmatrix} = \begin{pmatrix} \langle \rho n | H | \pi^- p \rangle \\ \langle \omega n | H | \pi^- p \rangle \end{pmatrix}$$

and the transition probabilities of ρ and ω to 2π,

$$\underset{\sim}{T} = \begin{pmatrix} T_\rho \\ T_\omega \end{pmatrix} = \begin{pmatrix} \langle 2\pi | H' | \rho \rangle \\ \langle 2\pi | H' | \omega \rangle \end{pmatrix} .$$

The prime on H' indicates that T includes all possible transitions except those that involve transitions connecting ω and ρ which will be included in the mass matrix.

We consider $|\rho\rangle$ and $|\omega\rangle$ to be eigenstates of G parity with eigenvalues $G_\rho = 1$ and $G_\omega = -1$. Then $\langle 2\pi | H_{ST} | \omega \rangle = 0$, so that the only non-zero part of T_ω comes from $\langle 2\pi | H_\gamma' | \omega \rangle$, where H_γ' represents isospin violating transitions (presumably second order electromagnetic) that do not involve ρ. If present theoretical understanding of such terms is correct, they will be so small that within the available experimental sensitivity it is reasonable to assume T_ω is negligible. Then the possibility of $\omega \to 2\pi$ comes from the small electromagnetic mixing term, δ, of the ω-ρ mass matrix

$$M = \begin{pmatrix} M_\rho & -\delta \\ -\delta & M_\omega \end{pmatrix} = \begin{pmatrix} m_\rho - i\,\frac{\Gamma_\rho}{2} & -\delta \\ -\delta & m_\omega - i\,\frac{\Gamma_\omega}{2} \end{pmatrix} \qquad (2)$$

(The fact that $\delta_{\omega\rho} = \delta_{\rho\omega} = \delta$ is a consequence of CPT invariance.[9]) One must note that there are no absolute grounds for assuming $T_\omega = 0$. As Gourdin, Stodolsky and Renard suggest,[12] it may turn out to be necessary to set $T_\omega \neq 0$ in order to understand experimental results. For this reason, in what follows we will assume $T_\omega \neq 0$.

$\underset{\sim}{A}$ and $\underset{\sim}{T}$ are functions of phase space variables like momentum transfer and decay angle in the rest frame, as well as of spin variables. In the subsequent analysis, we will assume $\underset{\sim}{A}$ and $\underset{\sim}{T}$ to be averaged over the spin states and the small region of phase space accepted by the experiment. This will introduce some degree of incoherence into the results and reduce the size of any ω-ρ interference effect. For the time being, however, we will ignore this problem.

In terms of $\underset{\sim}{A}$, $\underset{\sim}{T}$, and $\underset{\sim}{\underset{\sim}{M}}$, we may write the propagator equation for the amplitude, Ψ, of the reaction $\pi^- p \to \pi^+\pi^- n$ proceeding through ρ or ω as[9]

$$\Psi = \underset{\sim}{T} \frac{1}{(m\underset{\sim}{1})^2 - \underset{\sim}{\underset{\sim}{M}}^2} \underset{\sim}{A} \tag{3}$$

where m is the 2π invariant mass.

After inverting the propagator matrix and carrying out the multiplication, we find for the amplitude squared

$$|\Psi|^2 = \frac{|A_\rho|^2 |T_\rho|^2}{|m^2 - M_\rho^2|^2} + \frac{|a_\omega|^2 |T_\rho|^2}{|m^2 - M_\omega^2|^2} + 2\mathrm{Re}\left[\frac{A_\rho^* a_\omega |T_\rho|^2}{(m^2 - M_\omega^2)(m^2 - M_\rho^2)^*}\right] \tag{4}$$

where

$$a_\omega \simeq A_\omega \frac{(m_\omega+m_\rho)}{(m^2-M_\rho^2)} [\delta(1+\beta A_\rho/A_\omega)+\beta(m_\omega-m_\rho+i\frac{\Gamma_\rho}{2})] \tag{4a}$$

with $\beta = T_\omega/T_\rho$. The details of the algebra that lead up to Eqs. (4) and (5) may be found in Appendix I. With obvious justification, it is assumed here that $\delta^2 << M_\rho^2$ or M_ω^2, and that the widths may be neglected in $(M_\omega + M_\rho)$. Note that a_ω (the amplitude of the $\omega \to 2\pi$ effect) is a slowly varying function of m, and that the numerator of a_ω in Eq. (4a) has been evaluated at $m = m_\omega$. In Eq. (4), the squared denominators are just the Breit-Wigner quadratic denominators. For example,

$$|m^2-M_\rho^2|^2 \simeq (m^2-m_\rho^2)^2 + m_\rho^2\Gamma_\rho^2 \quad .$$

Using Eq. (4) we may obtain the experimental distribution of 2π events, $N_{2\pi}(m)$, by integrating $|\Psi|^2$ over the $2\pi n$ phase space. After integrating over the neutron variables we have[13]

$$N_{2\pi}(m)\,dm^2 = n\int|\Psi|^2\epsilon_{2\pi}(m,\theta)\phi(m)\frac{q}{4m}2\pi\ d\cos\theta\ dm^2 \quad . \tag{5}$$

Here $\epsilon_{2\pi}(m,\theta)$ is the experimental efficiency function of m and the 2π center of mass angle θ, n is a normalization constant, and q is the momentum of either pion in the 2π rest frame. $\phi(m)$ is the phase space function of m that results from the integration over the neutron variables. Carrying out the integral in Eq. (5), we write $N_{2\pi}(m)$ in a general form useful for fitting:

$$\begin{aligned} N_{2\pi}(m) = [&|A_\rho|^2 BW_\rho^2 + |a_\omega(m^2-M_\rho^2)|^2 BW_\rho^2 |F_\omega|^2 \\ &+2|A_\rho^* a_\omega(m^2-M_\rho^2)|\cos\phi\, BW_\rho^2 \mathrm{Re}F_\omega + 2|A_\rho^* a_\omega(m^2-M_\rho^2)| \\ &\sin\phi\ BW_\rho^2 \mathrm{Im}F_\omega + \text{Background}]\epsilon_{2\pi}(m)\phi(m) \end{aligned} \tag{6}$$

Here

$$\phi = \arg(A_\rho^* a_\omega(m^2-M_\rho^2)) \tag{7a}$$

is the relative phase of the $\rho \to 2\pi$ amplitude and $a_\omega(m^2-M_\rho^2)$. The function $\epsilon_{2\pi}(m)$ is the efficiency averaged over $\cos\theta$. In this equation, we use Jackson's form of the ρ Breit-Wigner amplitude squared.[13] We have

$$BW_\rho^2 = n\int \frac{|T_\rho|^2}{|m^2-M_\rho^2|^2}\,\frac{q}{4m}\,2\pi d\cos\theta = n\,\frac{m_\rho\Gamma_\rho}{(m^2-m_\rho^2)^2+m_\rho^2\Gamma_\rho^2} \tag{7b}$$

since

$$\Gamma_\rho(m) = \frac{1}{2m_\rho}\int |T_\rho|^2\,\frac{q}{4m}\,2\pi d\cos\theta = \Gamma_{\rho o}\left(\frac{q}{q_o}\right)^3\frac{m}{m_\rho}$$

where $q_o = q$ when $m = m_\rho$. F_ω is the Breit-Wigner amplitude function for ω in the 2π spectrum:

$$|F_\omega|^2 = \frac{1}{|m^2-M_\omega^2|^2} \simeq \frac{1}{(m^2-m_\omega^2)^2+m_\omega^2\Gamma_\omega^2}\ ,$$

$$\mathrm{Re}F_\omega = |F_\omega|^2(m^2-m_\omega^2+\tfrac{1}{4}\Gamma_\omega^2)\ ,$$

and

$$\mathrm{Im}F_\omega = -|F_\omega|^2(m_\omega\Gamma_\omega)\ . \tag{7c}$$

The ω production amplitude, A_ω, may be determined in this experiment from a large sample of $\omega \to 3\pi$ in $\pi^+\pi^-\pi^o n$ final state events. Corresponding to Eq. (6) for 2π, we have for the distribution of events in the 3π mass spectrum

$$N_{3\pi}(m) = [|A_\omega|^2 BW_\omega^2 + \text{Background}]\,\epsilon_{3\pi}(m)\,\phi(m) \tag{8}$$

where $\epsilon_{3\pi}(m) \neq \epsilon_{2\pi}(m)$ is the efficiency function for the 3π events. Here a $3\pi n$ phase space has been integrated to get Eq. (8), and $\epsilon_{3\pi}(m)$ is averaged over the Dalitz plot. BW_ω^2 has the same form as BW_ρ^2 of Eq. (6):

$$BW_\omega^2 = n\int \frac{|T_{\omega\to 3\pi}|^2\pi^2 dE_1 dE_2}{|m^2-M_\omega^2|^2} = n\,\frac{m_\omega\Gamma_{\omega\to 3\pi}}{(m^2-m_\omega^2)^2+m_\omega^2\Gamma_\omega^2} \tag{8a}$$

with the partial width assumed to be $\Gamma_{\omega\to 3\pi} = 0.9\ \Gamma_\omega$, (see Ref. 30) and the same normalization constant as in Eq. (7b).

Integrating over the various terms of Eqs. (6) and (8) allows us to relate the ρ and ω amplitudes to the number of ρ and ω experimentally observed in the 2π and 3π spectra. These integrations were carried out with Monte Carlo techniques that included the experimental efficiencies. The details of the calculations are discussed in Appendix I. We find

$$|A_\omega|^2 = 2.193\ N_{\omega\to 3\pi} \tag{9a}$$

$$|A_\rho|^2 = 1.775\ N_{\rho\to 2\pi} \tag{9b}$$

In a later section we shall see that in this experiment, $N_\rho/N_{\omega\to 3\pi} \approx 0.38$. Thus, $|A_\rho|/|A_\omega| \approx 0.56$. This combined with an estimate of the upper limit of β justifies dropping the $\beta A_\rho/A_\omega$ term of Eq. (4a) for a_ω. To see this we relate β to the branching ratio $B = \Gamma_{\omega\to 2\pi}/\Gamma_{\omega\to 3\pi}$, remembering that the direct $\omega \to 2\pi$ transition (T_ω) contributes only a small part of the $\omega \to 2\pi$ rate:

$$\beta = T_{\omega\to 2\pi}/T_\rho \le (\Gamma_{\omega\to 2\pi}/\Gamma_\rho)^{1/2} = (B\Gamma_{\omega\to 3\pi}/\Gamma_\rho)^{1/2} \approx (B/10)^{1/2}\ .$$

If we assume $B < 10\%$ with considerable justification then $\beta A_\rho/A_\omega \leqslant 0.56$. Thus with an error that must be considerably less than 6%, we may drop this term leaving

$$\begin{aligned} a_\omega &\simeq A_\omega \frac{(m_\omega+m_\rho)(\delta+\beta(m_\omega-m_\rho)+i\ \Gamma_\rho/2)}{(m^2-M_\rho{}^2)} \\ &\simeq A_\omega \frac{(m_\omega+m_\rho)\delta'}{(m^2-M_\rho{}^2)} \end{aligned} \tag{4a'}$$

where $\delta' = \delta + (m_\omega - m_\rho + \frac{\Gamma_\rho}{2})\beta$. Given the possibility that δ is very small, which has not been ruled out experimentally,

there is no justification for neglecting β at this stage. And δ' not δ is the physical parameter measured by experiments studying $\omega \to 2\pi$.

Just as we did for A_ω and A_ρ, we can relate $|a_\omega|^2$ to $N_{\omega\to 2\pi}$, which is the experimental number of events corresponding to the second term of Eq. (6). $N_{\omega\to 2\pi}$ is the number of $\omega \to 2\pi$ events not including the interference effects. Knowing the magnitude of a_ω from the number of ω events in the 2π spectrum and the magnitude of A_ω from the number of ω in the 3π spectrum, we can determine the magnitude of δ' in the experiment by solving Eq. (4a'):

$$|\delta'| = 20.2 \left(\frac{\epsilon_{3\pi}(m_\omega)}{\epsilon_{2\pi}(m_\omega)} \frac{N_{\omega\to 2\pi}}{N_{\omega\to 3\pi}}\right)^{1/2} = 20.2\ B^{1/2}\ \text{MeV}. \tag{9c}$$

Here B is the branching ratio, $B = \Gamma_{\omega\to 2\pi}/\Gamma_{\omega\to 3\pi}$, and as discussed later the ratio of experimental efficiencies is determined using a Monte Carlo calculation.

As is evident from Eq. (7c), Im f_ω is experimentally indistinguishable from $|F_\omega|^2$, so that in practice we are forced to combine the fourth and second terms of Eq. (6). Thus the coefficient of $BW_\rho^2|F_\omega|^2$ in Eq. (6) is

$$|a_\omega(m^2-M_\rho^2)|^2 - 2m_\omega\Gamma_\omega|A_\rho^* a_\omega(m^2-M_\rho^2)|\sin\phi\ . \tag{10}$$

Since the second term of this coefficient may clearly be either positive or negative, the fact that experimentally the whole coefficient turns out to be zero does not necessarily imply that $a_\omega = 0$. This was pointed out as long ago as 1964 by Lütjens and Steinberger,[6] and has been the source of much difficulty in efforts to understand what really is going on

with respect to $\omega \to 2\pi$. The problem is compounded by the fact that we have no way of really knowing how valid is the complete coherence of ω and ρ in the 2π mass spectrum that is implied by Eq. (4) or (6). The complete coherence of these equations is clearly valid for that impossible situation where all events come from the same point in phase space. But for real experiments in which events come from a finite range of momentum transfer, for example, some degree of incoherence will creep in, and the size of the interference terms will be reduced. This will happen since the relative phase, ϕ, may vary over the phase space accepted by the experiment. Then $\cos\phi$ and $\sin\phi$ in the third and fourth terms of Eq. (6) must be averaged over the range of phase space variables. This can only reduce the magnitudes of these terms.

The degree of coherence may be parameterized by multiplying the two interference terms of Eq.(6) by the variable c. For complete coherence c=1, and for total incoherence c=0. Taking this into account the experimentally measurable distribution (Eq.(6)), becomes in practice:

$$N_{2\pi}(m) = [\alpha_1 BW_\rho{}^2 + \alpha_2 BW_\rho{}^2 |F_\omega|^2 + \alpha_3 BW_\rho{}^2 \mathrm{Re}F_\omega + \mathrm{Background}]\phi(m)\epsilon_{2\pi}(m), \quad (11)$$

where

$$\alpha_1 = |A_\rho|^2$$

$$\alpha_2 = |a_\omega(m^2 - M_\rho{}^2)|^2 - 2cm_\omega\Gamma_\omega |A_\rho{}^* a_\omega(m^2 - M_\rho{}^2)| \sin\phi$$

$$\alpha_3 = 2c|A_\rho{}^* a_\omega(m^2 - M_\rho{}^2)| \cos\phi \ . \quad (11a)$$

Theoretical efforts to predict the rate of $\omega \to 2\pi$[12,14,15] are aimed in two directions: the magnitude and phase of δ,

and the relative production amplitude phase, ϕ. With knowledge of these quantities, the magnitude and shape of the $\omega \to 2\pi$ effect may be predicted.

By limiting the region of momentum transfer in their experiment, G. Goldhaber et al were able to observe a negative interference dip at the ω mass,[16] clear evidence that their data was at least partially coherent and that $\alpha_2 < 0$ and $\phi \approx \frac{\pi}{2}$. That experiment studied the 2π spectrum in the reaction

$$\pi^+ p \to \pi^+ \pi^- \Delta^{++} , \tag{12}$$

and the theorists, A. Goldhaber et al, have predicted that if negative interference is observed in reaction (12) with $\phi \approx \frac{\pi}{2}$, then positive interference should be observed in our reaction,

$$\pi^- p \to \pi^+ \pi^- n$$

with $\phi \approx -\frac{\pi}{2}$.[14] Their calculations assume a momentum transfer considerably smaller than that of this experiment. However, as we will see later, if this phase is assumed for our data, it provides a very strong restriction on the result.

Recently, evidence for a positive ρ-ω interference peak, $\phi \approx -\pi/2$, was reported by a French group for the clashing beam reaction[17]

$$e^+ e^- \to \pi^+ \pi^- .$$

A. Goldhaber et al predict $\phi \approx \pi$ for this reaction,[14] which has been studied independently by Gourdin, Stodolsky and Renard[12] who also find the clashing beam results[17] in contradiction with their expectations that $\phi \approx \pi$.

The subject definitely is not closed, and in the

following sections, we describe still another experiment studying the ephemeral decay of omega to 2π.

II. EXPERIMENTAL APPARATUS AND RUNNING PROCEDURE

In this experiment, omegas were detected in the reaction $\pi^- p \rightarrow \omega n$. The three pion decay mode was studied in

$$\pi^- p \rightarrow \pi^+ \pi^- \pi^o n \tag{13}$$

and the search for effects of ω in the two pion spectrum was made in the reaction

$$\pi^- p \rightarrow \pi^+ \pi^- n \ . \tag{14}$$

The experiment was run at the Brookhaven AGS in 1967 using equipment designed for a study of the charged decays of the η. The apparatus and running procedure for that experiment are described in detail in the Ph.D. dissertation of Stephen Stein.[18] Essentially no changes were made to the apparatus for the ω experiment.[19]

A beam of negative pions at a momentum of 1245 MeV/c ± 3/4% was produced by circulating protons inside the AGS incident on a 0.050 in. Be wire and defined by a beam transport system that included two electrostatic separators (Fig. 1). A beam spot of about 1 in. diameter was focused on the end of a 2 in. diameter by 1 ft cylindrical liquid hydrogen target. An incident pion on target was defined electronically by the coincidence of signals from four small scintillation counters ($T_1 T_2 T_3 T_4$) that formed a telescope at the end of the beam line after the last bending magnet. T_4 was placed directly in front of the target and was 1.25 in. in diameter. A fifth counter T_5 was placed immediately behind the target,

and the anti-coincidence of T_5 with a coincidence in the telescope provided a signal (called pi-disappearance) that indicated a pion interaction inside the hydrogen target.

The target was suspended in the well of a U-shaped array of nine spark chambers, three in each of three quadrants (left side, right side, and bottom). This array of chambers was itself suspended inside a large magnet as shown in Fig. 2. During this experiment, the magnitude of the B-field within the magnet was about 6.9 kG. The direction of the field was the same as that of the beam so that the beam was not affected by the field. However, the charged pions of Reactions 13 and 14 coming out in general transverse to the beam did have their trajectories curved by the field. This curvature, and thus the momenta of the pions, was measured by the spark chambers. But before a commitment was made to fire the spark chambers and invest about 20 msec of deadtime, it was necessary to know whether two charged pions had actually passed through two different spark chamber quadrants. This information was determined very rapidly from signals from three pairs of overlapping counters directly behind the outermost spark chamber in each quadrant. If two (and only two) of these so-called "logic counters" signalled in different quadrants and no signals came from a variety of anti-counters placed at other points surrounding the magnet, the decay pion requirements were assumed to be satisfied.

The charged pions in the beam that did not interact in the target were swept to one side by a wide gap bending magnet

immediately following the analyzing magnet. This beam, after passing through a large helium bag (in order to reduce scattering that might confuse the neutron detection), was dumped in a wall of concrete. The neutrons resulting from reaction 13 or 14 in the target were detected by a bank of nine neutron detectors about thirty feet away from target. These nine detectors, each a 2 ft cube of liquid scintillator, were arranged in three rows of three. An overall view of the experiment is shown in Figs. 3 and 4. Directly in front of each liquid counter was a charged particle counter which was used in anti-coincidence with the liquid counters to indicate the presence of a neutral particle. The spark chamber trigger requirement from the neutron counters was the presence of one and only one neutral particle arriving in a specified time gate. The clock for this time was started when a beam particle went through T_3 and was stopped at a pulse from the neutron counters. If there was a "pi-disappearance" signal, this clock measured the time of flight (TOF) of the neutron from the target to the neutron counters. The time of flight gate was adjusted so that it included the unique time of flight of a neutron scattering off an ω in the reaction $\pi^- p \rightarrow \omega n$. The gate opened about 4 nsec before this ω TOF and remained open about 10 nsec. A very clear peak can be seen in the $\pi^+\pi^-\pi^o n$ final state events at the ω TOF. After corrections (which will be discussed in detail later) were made for the location of the interaction vertex and for the delay in the detectors correlated with pulse height, a Gaussian fit to the ω peak in the TOF

spectrum gave a width of 0.839 ± 0.016 nsec. Part of this width is due to the intrinsic ω width. If this is removed, one finds that the timing resolution is 0.78 ± 0.02 nsec. This excellent resolution enables one to use the neutron TOF information in studying the two pion mass spectrum in Reaction 14 as we shall see later. The mass resolution in this spectrum was determined, using a Monte Carlo technique, to have a half width of about 13 MeV.

Summarized below are the requirements that had to be satisfied before the fast logic fired the spark chambers:

pi disappearance -- $(T_1T_2T_3T_4)\bar{T}_5$

logic counters -- 2 logic counters in 2 different quadrants and no antis

neutron counters -- 1 neutron counter and no anti

neutron time of flight -- within 10 nsec gate surrounding ω TOF.

If all these requirements were satisfied, a high voltage pulse was applied to the spark chambers. During the ω experiment, the chambers were fired about five times per AGS beam spill. The spills lasted about 400 msec and were repeated every 2.4 sec.

In order to handle the large amount of data, it was necessary to use some kind of automated spark chamber system. Sonic techniques which work reliably inside a magnetic field were used in the experiment. Within each chamber a set of four microphones, one at each corner, sensed the sound wave produced by a spark. The time when the sound of the spark

reached each microphone was digitized and transmitted to an IBM 360/30 computer on line. The computer also received the neutron time of flight and information indicating which logic and neutron counters were hit. All this information was written on magnetic tape from which the data were later reconstructed and analyzed on the Nevis 360/44. The on-line computer reconstructed spark positions, calculated spark chamber constraint quantities, maintained tables of chamber and counter triggers, and displayed this information on a typewriter at the request of experimenters. The displays enabled the experimenters to monitor equipment performance and correct malfunctions at a very early time. The computer also did a preliminary momentum reconstruction on-line and displayed histograms of kinematic quantities and the neutron time of flight on an oscilloscope. These histograms provided information on the rate of production of ω in Reaction 13 and on the kinematic cleanliness of the data being taken. An alarm system independent of the computer sounded when the spark chamber pulser fired without a trigger from the fast logic. This provided early warning of pulser failure.

The quality of the beam was monitored without help from the computer by routine checks of the ratio of certain rates in the beam telescope. For example, the ratio of $(T_1T_2T_3T_4)/(T_1T_2T_3)$ indicated how well the beam was focused on the target. If these checks indicated a problem in the beam, the beam tuning was touched up in the beam trailer or the AGS control was requested to replace the Be target.

Reversing the magnetic field in the analyzing magnet has the effect of cancelling out asymmetrical biases in the geometry. Reversing the spark chamber electric field reverses the direction of drift of ions between the chamber plates and reverses the direction of the E x B drift that can bias the momentum measurement. Removing the magnetic field entirely allows a later study of straight line tracks to determine the relative position of the spark chambers. Taking all these factors into consideration, the running procedure called for the following schedule: Every two hours the magnetic field in both the analyzing and sweeping magnets was reversed; every four hours the electric field was reversed; and every ten hours the magnetic field was turned off for a two hour run.

III. RECONSTRUCTION AND EVENT DEFINITION

A. Sonic Determination of Spark Position

The sonic spark chambers used in this experiment each consisted of a pair of 1 mil aluminum foil plates separated by a gap of 1/4 in. with four ceramic cylindrical microphones near the corners. A test spark device made of two needles with a small gap was accurately positioned near one edge of the chamber. A schematic layout of a typical chamber is shown in Fig. 5. The nine spark chambers were contained in a large air tight vacuum box through which a gas mixture of 90% neon 10% helium was slowly circulated so that the gas temperature was nearly the same in different chambers.

The propagation of sound in the close vicinity of such cataclysmic events as sparks in spark chambers and atomic bomb explosions is known to be non-linear because of the initial shock wave. The effects of this non-linearity can be accounted for in the linear region away from the spark by a constant shift in the time scale, t_p. In terms of t_p and the velocity of sound in the gas V, the distance d from the spark at a measured time t_m is

$$d = V(t_m + t_p) = Vt$$

where $t \equiv t_m + t_p$. Referring to Fig. 5, it is easy to compute the spark coordinates u and z in terms of the sonic times t_i measured at each microphone (including the t_p factor):

$$u = \frac{V^2}{8a}\,(t_3{}^2 - t_1{}^2 + t_4{}^2 - t_2{}^2)$$
$$z = \frac{V^2}{8b}\,(t_2{}^2 - t_1{}^2 + t_4{}^2 - t_3{}^2) \qquad (15)$$

It remains to determine V and t_p for each chamber. If d_i represents the distance from the test spark to microphone i, then the velocity may be determined from test spark events. Using microphones 1 and 3 for example, we have

$$V = \frac{d_1 - d_3}{t_1 - t_3} \quad .$$

Note that this result is independent of the shock wave factor t_p. The test spark in each chamber was fired five times every 256 AGS pulses. The velocity calculated from these test spark firings (typically $V \approx 0.047$ cm/μsec) was averaged for each data taking run of one to two hours. Run to run changes in V due to temperature changes were taken into account

in the reconstruction using these numbers. However, the test spark velocities in different chambers differed from each other and from an optical calibration by a small constant amount. A better understanding of V and a determination of t_p can be made on an event by event basis using the extra information available from the four microphones in each chamber which over-determines the spark coordinates. Details of this method and its relation to the test spark velocities along with a discussion of corrections for sparks occurring near a microphone have been described by Stephen Stein in Ref. 18. Using these techniques, the parameter t_p was determined for each event and the coordinates u and z calculated according to Eq. (15). Also computed was the constraint quantity

$$DT = t_1^2 - t_2^2 - t_3^2 + t_4^2$$

which may be used to eliminate double spark events and chamber malfunctions. Note that DT is proportional to the difference in the coordinate u or z as determined by adjacent pairs of microphones. Normally DT should be zero.

B. Magnetic Field Map

The pion momentum reconstruction technique which will be described in the next section requires a point by point knowledge of the magnetic field in the analyzing magnet. A mapping of the field was carried out at irregular spacing of about 3 in. in the x and y directions and 2 in. in the z directions using a Hall probe.[20] (The coordinate directions are shown in Fig. 2.) Measurements were made of the three

field components. The data was corrected for the fact that the probe axis of sensitivity was not actually in the precise direction it was supposed to be. The axis was determined by enclosing the probe in a carefully machined 4 in. cube and taking measurements at the same place in the field but with the cube in a series of different orientations. With the axis known, one can effectively rotate the data so that one gets the three components wanted.

Using a three dimensional quadratic interpolation technique, the measured data points were converted into a new set of points, at a more convenient regular 2 in. spacing in all directions. Small measuring errors in the data points are enormously magnified when one takes differences of nearby points in order to calculate the first and second derivatives that are needed by the reconstruction program. It is therefore necessary to smooth the data in some manner. The method chosen was to fit the interpolated data to a hypothetical field function $\underset{\sim}{B}$ that satisfies Maxwell's equation:

$$B_i(\underset{\sim}{r}) = \sum_{\ell m} A_{\ell m} H_{\ell m i}(r,\theta,\phi)$$

where

$$H_{\ell m i} = \frac{\partial}{\partial r_i}\left(r^{\ell} Y_{\ell m}(\theta,\phi)\right) \qquad i = 1,2,3.$$

The derivatives of the harmonic polynomials, $H_{\ell m i}$, are solutions of Maxwell's equations since the harmonic polynomials are solutions of $\nabla^2\phi = 0$ and $\underset{\sim}{B} = \underset{\sim}{\nabla}\phi$, and these two equations are equivalent to the magnetic field Maxwell's equations in a region of no magnetic sources or changing electric field.

The hypothesis therefore constrains the data to the requirements of Maxwell's equations.

The estimated measurement errors for the three different field components used in the fit were $\sigma_x = 50$ G, $\sigma_y = 40$ G, and $\sigma_z = 15$ G. Since the major component of $\underset{\sim}{B}$ is in the z direction, a slight rotation of the probe when measuring the other two components will cause a large error. This is why σ_x and σ_y are larger than σ_z. As a result of a circular hole in both pole pieces, through which the beam passed, the magnitude of the field, scanned across the x or y direction, had a dip in the center as well as the two sides. It was thus necessary to use terms up to sixth order in the fit. Using all 63 polynomials up to sixth order, we were able to get a good fit with a $\chi^2 = 5343$ for 3988 degrees of freedom. The original plan was to select a subset of the 63 polynomials that would provide an adequate fit and allow rapid access to the magnetic field at any point in the reconstruction program. It turned out to be possible to pick 25 out of the 63 polynomials of sixth order or less and fit to them without significantly increasing the χ^2. (For 4026 degrees of freedom, $\chi^2 = 5879$ for the 25 polynomial fit.) However, it turned out that this method of accessing the field data would be very time consuming since the reconstruction program requires a variety of derivatives of the field. These derivatives are obtained automatically during interpolation. So the method of storing and accessing the field that we used was first to set up a table of smoothed field points

at 2 in. spacing using the best fit of Maxwell polynomials to the field. Then within the reconstruction program, a three dimensional quadratic interpolation technique was used to get the field at a desired point. A one-dimensional quadratic interpolation to determine B at point S when we have a table of B_i at points S_i is given by[21]

$$B = B_1+(B_2-B_1)\frac{S-S_1}{h} + \frac{B_3+B_1-2B_2}{2h^2}(B-B_1)(B-B_1-h)$$

where h^2 is the spacing of points in the table. One may extend this to three dimensions by using the 27 points in the table closest to the needed location (x,y,z) as follows: First, interpolate across the 9 rows in the x direction to the value x; using these 9 values, interpolate down the three y columns to the points at y; finally interpolate these 3 values in the z direction to the point z. In the process, first and second derivatives of the field are automatically determined from the various differences.

During the ω run at Brookhaven, the field inside the magnet was kept constant at about 6.9 kG by monitoring a Hall probe attached near the upstream pole piece. By extrapolating the mapped field to this location and taking into account the calibration of the Brookhaven Hall probe, it was possible to normalize the field map to the actual field strength used during the experiment. This normalization agreed with the magnet excitation curves measured with still another Hall probe.

C. Pion Momentum Reconstruction

The variation in the magnetic field in different parts of the magnet was at the most about ±7% according to the field map described in the previous section. The reconstruction program took this variation into account in determining the momenta of the pions. This was done by starting with an estimate of the momentum determined assuming a flat field of 6.9 kG in the z direction. An imaginary particle with this momentum was then traced through the actual field by the program. The momentum was then corrected to compensate for the deviations of the traced track chamber intersections from the actual sparks. After one or at most two iterations of this sort, the program was able to find a momentum which had a trajectory that intersected the three sparks within very good tolerance. In order to illustrate in detail how this technique works, we will consider an event in quadrant 1 with the coordinate system as defined in Fig. 2.

In a flat magnetic field pointing in the z direction, the trajectory of a charged particle is a helix spiralling around the field lines. Five parameters completely define this helix: x_o, y_o and r which define the center and radius of the circle projected in the x-y plane by the helix, and α and z_o which define the pitch and orientation of the helix. We are interested in the intersection of this helix with the three chamber planes, i = 1,2,3. Writing the nine equations of intersection in terms of an angle θ which is a measure of the time along the trajectory we have

$$x_i = x_o + r\cos\theta_i$$
$$y_i = y_o + r\sin\theta_i \qquad (16)$$
$$z_i = z_o + \alpha\theta_i \quad .$$

These nine equations determine the eight unknowns (the five helix parameters plus the three θ_i) and allow one further constraint on the data. By not using the z equation for the outer chamber (i=3), we may calculate a projected value of z in the outer chamber z_{proj} using the values of α and θ_3 determined in the other equations. The difference of the measured z coordinate in the outer chamber from z_{proj}

$$DZ = Z_3 - Z_{proj} \qquad (17)$$

should differ from zero only because of measurement error. However, events with serious scattering in the plates of the middle chamber will show a gross deviation from DZ = 0. DZ may thus be used to get rid of events with bad scattering. This will be discussed further in a later section. With a knowledge of the five helix parameters and the magnitude of the field, it is a simple matter to find the momentum of the particle at any point on the trajectory $\underset{\sim}{r} = (x,y,z)$:

$$P_x = \mp \frac{eB}{c}(y-y_o)$$
$$P_y = \pm \frac{eB}{c}(x-x_o) \qquad (18)$$
$$P_z = \frac{eB}{c}\alpha$$

where $\frac{eB}{c} = 0.3$ B MeV/cm for B in kG. The sign of the particle charge is known from the curvature of the track and the direction of the magnetic field.

Before outlining the iteration procedure, we define a number of simple quantities:

$\underset{\sim}{P}_{FLAT}(\underset{\sim}{r}_i)$ $i = 1,2,3$ is the momentum vector at the inner chamber (point $\underset{\sim}{r}_1$) obtained assuming a <u>flat</u> magnetic field of magnitude 6.9 kG in the z direction. $\underset{\sim}{P}_{FLAT}(\underset{\sim}{r}_i)$ is a function of three spark coordinate measurements, $\underset{\sim}{r}_i$, which are close to but not necessarily equal the real spark position measurements. $\underset{\sim}{P}_{FLAT}$ is determined from the three points $\underset{\sim}{r}_i$ by the standard flat field method described above using Eqs. (16) and (18).

$\underset{\sim}{R}_i(\underset{\sim}{P}, \underset{\sim}{r}_{start})$ is the set of three points obtained by tracing through the <u>mapped</u> field a particle that starts at $\underset{\sim}{r}_{start}$ with momentum $\underset{\sim}{P}$. The tracing technique will be described later. $\underset{\sim}{r}_i^{spark}$ are the true measured spark positions.

With these definitions, the program follows the following iterative procedure letting $\underset{\sim}{r}_i = \underset{\sim}{r}_i^{spark}$ and $\underset{\sim}{r}_{start} = \underset{\sim}{r}_1^{spark}$ for the first iteration:

1. Calculate $\underset{\sim}{P}_{Flat}(\underset{\sim}{r}_i)$.
2. Trace through the field and get the 3 chamber intersections $\underset{\sim}{R}_i = \underset{\sim}{R}_i(\underset{\sim}{P}_{Flat}(\underset{\sim}{r}_i), \underset{\sim}{r}_{start})$.
3. Minimize

$$\chi^2 = \sum_{i=1}^{3} \left(\frac{\underset{\sim}{R}_i - \underset{\sim}{r}_i^{spark}}{\sigma_i}\right)^2$$

allowing $\underset{\sim}{R}_i \rightarrow \underset{\sim}{R}_i + \underset{\sim}{\Delta}$, and determine $\underset{\sim}{R}_i = \underset{\sim}{R}_i + \underset{\sim}{\Delta}$ at the minimum. This minimization insures that by starting the trace at the inner chamber, we do not force the track through that spark in blind preference to the other two

sparks. The errors σ_i used in this procedure will be discussed later.

4. With the new values of $\underset{\sim}{R}_i$, calculate $\underset{\sim}{D}_i = \underset{\sim}{R}_i - \underset{\sim}{r}_i^{spark}$. Let $\underset{\sim}{r}_i = \underset{\sim}{r}_i - \underset{\sim}{D}_i$, and $\underset{\sim}{r}_{start} = \underset{\sim}{r}_{start} + \underset{\sim}{\Delta}$. Continue the iteration by returning to Step 1 with the new values of $\underset{\sim}{r}_i$ and $\underset{\sim}{r}_{start}$, until χ^2 changes by less than 0.1 from one iteration to the next. The iterative procedure is said to have failed if this criterion is not reached after 8 interations.

Since this is a fitting method, one must consider the question of what errors to attribute to the various chamber measurements. However, it is worth noting first that the momentum obtained from this method is extremely insensitive to the relative errors of the three chambers. In tests, the relative chamber error was allowed to vary over a large range and there was no significant change in the momentum. (The vertex calculation to be discussed below was affected an observable amount by large variations in errors.) The errors that were used were

$$\sigma_i^2 = \sigma_{RES}^2 + S_i^2 \quad . \tag{19}$$

Here $\sigma_{RES} \approx 0.3$ mm is a resolution error identical for all three chambers and S_i is the error introduced by multiple scattering in the chamber foils. S_i is computed for each event by first calculating the quantity[22]

$$\langle\theta^2\rangle = 4\pi N\left(\frac{2Ze^2}{P\beta}\right) \ln(210\ Z^{-1/3})\, t \ . \tag{20}$$

With Z = 13, this is the mean squared angle of scattering projected on a plane for a singly charged particle of momentum P and velocity β going through t mils of aluminum with N atoms/cm^3. The multiple scattering width for the middle chamber S_2 is determined by multiplying $\langle\theta^2\rangle$ by the distance traveled by the particle between the inner and middle chambers, a quantity easily obtained in the trace procedure. For the outer chamber scattering in the middle chamber is also included in quadrature.

In order to trace the trajectory of a particle of given momentum through a known varying magnetic field, the following procedure which is based on a Taylor expansion of the trajectory was used:

1. Starting at point $\underset{\sim}{r} = \underset{\sim}{r}_{start}$ with momentum $\underset{\sim}{P}$ and energy E calculate the velocity $\dot{\underset{\sim}{r}} = \frac{c\underset{\sim}{P}}{E}$.
2. Fetch the field and derivatives at the point $\underset{\sim}{r}$. (If this is the first iteration for this track, get the field using the three dimensional quadratic interpolation described earlier. Store the relevant numbers so that they may be fetched more rapidly on subsequent iterations of the track.)
3. Calculate

$$\ddot{\underset{\sim}{r}} = \frac{e}{mc}\,(\dot{\underset{\sim}{r}} \times \underset{\sim}{B})$$

$$\dddot{\underset{\sim}{r}} = \frac{e}{mc}\,(\ddot{\underset{\sim}{r}} \times \underset{\sim}{B} + \dot{\underset{\sim}{r}} \times (\dot{\underset{\sim}{r}} \cdot \underset{\sim}{\nabla})\underset{\sim}{B})$$

$$\ddddot{\underset{\sim}{r}} = \frac{e}{mc}\,(\dddot{\underset{\sim}{r}} \times \underset{\sim}{B} + 2\ddot{\underset{\sim}{r}} \times (\dot{\underset{\sim}{r}} \cdot \underset{\sim}{\nabla})\underset{\sim}{B} + \dot{\underset{\sim}{r}} \times (\dot{\underset{\sim}{r}} \cdot \underset{\sim}{\nabla})^2\underset{\sim}{B})$$

using the values of $\underset{\sim}{B}$ and the derivatives obtained in

step 2. Note that $m = m_o\gamma = E$ is the relativistic mass of the pion.

4. Calculate the coordinate position of the track after the next step:

$$\underset{\sim}{r}_{new} = \underset{\sim}{r} + h\dot{\underset{\sim}{r}} + \frac{h^2}{2}\ddot{\underset{\sim}{r}} + \frac{h^3}{6}\dddot{\underset{\sim}{r}} + \frac{h^4}{24}\ddddot{\underset{\sim}{r}}$$

where h, the step size in seconds, is determined for each step by making the last term $\frac{h^4}{24}\ddddot{\underset{\sim}{r}} = 0.01$ cm. If the track did not cross the next chamber calculate the new velocity

$$\dot{\underset{\sim}{r}}_{new} = \dot{\underset{\sim}{r}} + h\ddot{\underset{\sim}{r}} + \frac{h^2}{2}\dddot{\underset{\sim}{r}} + \frac{h^3}{6}\ddddot{\underset{\sim}{r}}$$

and go back to 2 to take another step.

5. If the new track x position, x_{tr}, did cross the next chamber, carry out the following iteration procedure to determine the step size h necessary to get from the old x position, x_{old}, to within 0.005 cm of the chamber x_{ch}:

   a. Let $h = h\,\frac{(x_{ch}-y_{old})}{(x_{tr}-x_{old})}$.

   b. Calculate $x_{tr}=x_{old}+h\dot{x}+\frac{h^2}{2}\ddot{x}+\frac{h^3}{6}\dddot{x}+\frac{h^4}{24}\ddddot{x}$.

   c. If $|x_{tr}-x_{ch}|$ is still greater than 0.005 cm go back to a and try again.

   This simple technique normally converges after one iteration. When the iteration is successful, calculate the other coordinates (y,z) where the track intersects the chamber plane. If this is the last chamber, the trace procedure is complete. If not, calculate the new $\dot{r}$ and go back to 2 to take another step.

Similar tracing methods may be used to follow the two pions back from the inner chambers to the point of closest approach of the tracks. This point is assumed to be the interaction vertex which should be somewhere within the hydrogen target volume. The distance of separation at the vertex of the reconstructed tracks is a measure of multiple scattering errors in the first chambers and the hydrogen. Cuts on this quantity perform a similar function as cuts on DZ discussed earlier.

After the iteration procedure for both tracks is completed as described above and the momenta at the two inner chambers known, the program traces back, one track then the other, searching for the point of closest approach. On the first step back, the time of intersection with the hydrogen target is determined in an iterative procedure identical to that used in getting the intersection with a chamber. This time is stored and later subtracted from the total time from inner chamber to vertex to get the time spent by the pion in the hydrogen. This time is then multiplied by

$$\frac{dE}{dt} = c\beta \frac{dE}{dx} = 0.307\ c\beta\rho[\frac{E^2}{P^2}\ \ell n(2.81\ P^2)-1]\text{MeV/sec}$$

where $\frac{dE}{dx}$ is the Bethe-Bloch expression,[23] to determine the amount of energy lost by the pion in passing through the liquid hydrogen (density $\rho = 0.0586\ \text{gm/cm}^3$). The pion energy is then corrected by this amount. All other contributions to energy loss are negligible compared to the loss in the hydrogen which typically amounted to 5 MeV.

The size of the first step back is determined by using as an estimate the time from vertex to inner chamber using the flat field technique to get the helix angle and multiplying by radius/βc to get time. After this first large step, a minimization procedure is used to get the appropriate step size for each track in order to converge on a solution for the point of closest approach: Let s^2 be the separation squared of the two tracks at times t_1 and t_2 and at positions $\underset{\sim}{r}_1$ and $\underset{\sim}{r}_2$ respectively on the two tracks. Then use the derivatives

$$\frac{\partial s^2}{\partial t_1} = 2\dot{\underset{\sim}{r}}_1 \cdot (\underset{\sim}{r}_1 - \underset{\sim}{r}_2)$$

$$\frac{\partial s^2}{\partial t_2} = -2\dot{\underset{\sim}{r}}_2 \cdot (\underset{\sim}{r}_1 - \underset{\sim}{r}_2)$$

$$\frac{\partial^2 s^2}{\partial t_1^2} = 2(\dot{\underset{\sim}{r}}_1^{\,2} + (\underset{\sim}{r}_1 - r_2) \cdot \ddot{\underset{\sim}{r}}_1) \quad \text{etc.}$$

to search for the point where $\frac{\partial s^2}{\partial t_1} = \frac{\partial s^2}{\partial t_2} = 0$. This is called the point of closest approach. (The method does not work if one searches for the point where $s = 0$ since there is in general no such point for two arbitrary helices.) The new step sizes Δt_1 and Δt_2 are found by solving the equations

$$0 = \frac{\partial s^2}{\partial t_1} + \Delta t_1 \frac{\partial^2 s^2}{\partial t_1^2} + \Delta t_2 \frac{\partial^2 s^2}{\partial t_1 \partial t_2}$$

$$0 = \frac{\partial s^2}{\partial t_2} + \Delta t_1 \frac{\partial^2 s^2}{\partial t_1 \partial t_2} + \Delta t_2 \frac{\partial^2 s^2}{\partial t_2^2} \quad .$$

The necessary derivatives are found easily in the trace program. The method typically converges satisfactorily in one iteration. This vertex technique gives results as good or

better than flat field techniques[18] when judged from distributions of vertex separation. It is obviously sensitive to the direction of the reconstructed momentum at the inner chamber and so is somewhat sensitive to the choice of σ_i in the momenta iteration-trace procedure. The method worked best when the errors corresponding to multiple scattering were used (Eq. 19).

As the last step in the reconstruction of the two tracks, the momentum at the point of closest approach was determined using Eq. (18).

D. TOF Calibration and Neutron Reconstruction

As has already been mentioned, a clear peak in the time of flight spectrum can be seen at the neutron time of flight corresponding to ω production. The peak is even more sharply enhanced if kinematic cuts (of a type to be discussed in detail later) are used to isolate events with three pions in the final state. This peak was used to calibrate the time of flight measurement. It was expected from previous experience that the location of the ω peak would show a correlation with the neutron counter pulse height. This results from the slight dependence on pulse height of the propagation time down the coaxial cable connecting the neutron counters with the discriminators. The data were separated into several pulse height ranges, and for each of the nine neutron counters the time of flight spectrum was fit to a gaussian plus a polynomial

background. The fitted centers of the ω peaks showed a linear dependence on pulse height. For each neutron counter, a straight line was fitted to the ω peak channels, and a parameter relating time of flight delay to pulse height was determined. Using this information the data were corrected for the pulse height effect and refitted to a gaussian peak plus a polynomial background. The center of the gaussian ω peak so determined and the pulse height correction factor were used in the initial neutron reconstruction. (In fact, after the final 3π kinematic definitions were made (see Sec. III.G), the TOF spectrum for each neutron counter was refit and ω peak centers determined from this final fit were used in the 2π mass spectrum analysis. This second fit made a very small correction of about 0.1 nsec which compares to the fit error in the gaussian center of about 0.04 nsec in each neutron counter.) The time of flight spectrum for all neutron counters combined and corrected for the pulse height effect is shown in Fig. 6.

The calibration of the time of flight analyzer electronics was performed using a pulse generator and calibrated delay lines. It was determined in this manner that one analyzer channel corresponded to 0.2125 nsec. In reconstructing the neutron momentum for a given event, we first determined the TOF channel relative to the ω channel as determined for an average $\omega \rightarrow 3\pi$ event in the calibration procedure described above. The mean vertex position in the z direction, $\bar{V}_z = \Delta$, for such events is not equal to zero because the geometrical

efficiency of the spark chambers favors upstream vertices. In fact, $\Delta = -3.60$ cm. Also correcting for pulse height, we calculate TOF for each event to be

$$\text{TOF} = (\text{measured channel}) - (\omega \text{ channel}) - (\text{pulse height factor}) \times (\text{pulse height} - 250) .$$

TOF represents the time of flight of the given event relative to the time of a neutron in the center of the ω peak coming from the mean vertex position, Δ. It is now necessary to remove the vertex dependence from TOF and correct for the time of flight of the beam pion that is still included in TOF. The corrected time of flight CTOF is

$$\text{CTOF} = \text{TOF} - (V_z - \Delta)/\beta_\pi c$$

where c is measured in cm/channels. CTOF is the time it took the neutron to travel from the vertex to the neutron counter relative to an ω neutron coming from the mean vertex position. From simple kinematics, we may calculate the time T_o for an ω neutron to travel from the mean vertex position to the center of the given neutron counter (a distance D_o). Then the velocity of the neutron is simply

$$\beta_n = \frac{|\underset{\sim}{r}|}{\text{CTOF}+T_o}$$

where $\underset{\sim}{r}$, as shown in Fig. 7, is the distance vector connecting the actual vertex and a point $(\bar{x}_n, \bar{y}_n)$ near the center of the neutron counter. The point $(\bar{x}_n, \bar{y}_n)$ is the average neutron intersection with the particular neutron counter. This point is determined from the four constraint $\pi^+\pi^-n$ data by

projecting the missing neutron momentum vector as determined from the pion momenta and averaging for each neutron counter. At this stage, it is easy to finish the reconstruction of the neutron momentum

$$\underset{\sim}{p}_n = m_n \beta_n \gamma_n \frac{\underset{\sim}{r}}{|\underset{\sim}{r}|} \quad .$$

For display purposes and the time of flight resolution measurement, we have further corrected CTOF so that all events appear to come from the same point eliminating a false widening of the CTOF ω peak due to the variation in vertex position:

$$\text{CTOF} = \text{CTOF} + \frac{D_o - |\underset{\sim}{r}|}{\beta_n c} \quad .$$

This is the variable that is histogrammed in Fig. 6.

E. Event Selection

In this section, we will describe the selection criteria that were applied to the data to provide a clean sample of events for analysis. In making these cuts, care was taken to study correlations between parameters being cut and other factors in order to avoid biasing the data. Each cut was determined by studying histograms of the variable of interest after the data had been cleaned up with a preliminary set of cuts for the other variables.

During the data taking runs considered in this experiment, the spark chambers were fired 144,763 times. At a very early stage, events were eliminated in which at least one of the six chambers did not fire in the quadrants where a logic counter detected a particle. Also removed were events

in which more than one neutron counter signaled and those in which sparks reconstructed outside the chamber foils. After these preliminary cuts, 88941 events remained.

A class of events that would anyway have failed later cuts like DZ and vertex separation failed during reconstruction and were removed leaving 67544 events. For example, these included situations for which the reconstruction iteration could not converge.

Serious failures in the sonic spark chambers such as double sparks or falsely triggering microphones are detected by looking at the variables DT and TP defined earlier. Neither the width nor the center of the TP distributions showed a dependence on such other factors as track momentum or spark position in the chamber. On the other hand, the width of DT in two chambers showed a significant dependence on the distance r from the chamber center. This effect resulted from occasional misfirings of certain microphones in these chambers. The DT cuts for these two chambers took this r dependence into account. The DT and TP cuts for all nine chambers are listed in Table I. Plots of the DT and TP distributions in a typical chamber are shown in Fig. 8. After these two cuts, 56907 events remained.

The constraint quantity DZ is designed to eliminate effects of serious scattering. The dependence of the width of DZ distributions on the multiple scattering factor $1/p\beta$ is evident even at the high values of pion momentum seen in this experiment. The multiple scattering width also depends on the

angle θ the track makes in the x-z plane with the perpendicular to the chambers (θ is shown in the inset to Fig. 9). By including such effects as the extra path lengths between chambers and in the chamber foils as θ increases, a dependence of $\sec^{5/2}\theta$ can be accounted for easily. In fact, the width of DZ distributions in the data shows an even stronger dependence on θ. It was found by dividing the data into 70 bins of different momentum and angle and performing a simple fit, that a good 3σ cut on DZ at all angles and momenta is

$$|DZ| \leq 0.25 \sqrt{1+\left(\frac{90}{p\beta}\right)^2 \sec^7\theta} \quad .$$

Plots of the distribution and this cut for various angles and values of $p\beta$ are shown in Fig. 9. After this cut, 52734 events remained.

The separation $\underset{\sim}{s}$ of the two helices at the point of closest approach provides another important means for eliminating false events. A variation in the angle of intersection θ affects the resolution widths of s. As a result, the s_x and s_y distributions for events with pions that went into quadrants 1 and 3 (Q 13) are different from those that had a pion in the bottom quadrant 2 (Q12 and Q23). Furthermore, these distributions have a non-gaussian appearance with wider tails than a gaussian. In order not to remove good events in the tails, these distributions were cut somewhat more loosely than normal. The cuts on s_x and s_y were:

Q13: $-0.25 < s_x < 0.11$ cm
$|s_y| < 0.40$ cm

Q12 and Q23: $|s_x| < 0.35$ cm

$$-0.47 < s_y < 0.54 \ .$$

Distribution of s_x and s_y are shown along with the cuts in Fig. 10. Though the multiple scattering factor $1/p\beta$ apparently does not significantly affect the x and y components of $\underset{\sim}{s}$, s_z does depend on momentum. This is most easily handled by separating the data kinematically into $\pi^+\pi^-n$ and $\pi^+\pi^-\pi^0n$ final state events in a manner to be described in the next section. The momentum spectrum of 3π events is lower than that of 2π events, and for these events multiple scattering effects mask the resolution sensitivity to the opening angle θ. In the 2π data, with higher momentum events, a dependence on $\cos\theta$ in the width of s_z becomes evident, and this dependence is taken into account in making the cut. The cuts on s_z are:

3π: $|s_z| \leq 0.46$ cm

2π: $|s_z| \leq (0.353 - 0.561\ (1+\cos\theta))$.

These cuts and typical distributions of s_z are also shown in Fig. 10. At this point, all events that did not satisfy the 2π or 3π kinematic criteria described in Sec. III.F were removed and there remained 16735 3π events and 15799 2π events. Then 369 events with two tracks of the same apparent electric charge were eliminated.

In making cuts on the vertex location $\underset{\sim}{V}$, the objective is to insure first that events came from interactions in the liquid hydrogen and second to eliminate events that clearly passed through metal supporting pieces near the target. By

studying distributions of the x and y locations of the vertex at different regions of z along the target, it was possible to determine that the center axis of the target was essentially parallel to the z axis but shifted slightly from zero in one direction. Thus, the basic vertex cuts are:

$$-15.8 < V_z < 15.0 \text{ cm}$$

$$V_r = [(V_x-0.29)^2 + (V_y-0.06)^2]^{1/2} < 2.45 \text{ cm} .$$

A schematic drawing of the target with the V_z cuts indicated is shown in Fig. 11. Visible in the drawing are three metal supports running the length of the target at the top and sides. Essentially no events that passed through these supports could also make it into the chamber geometry and so no data cut was needed. The drawing shows a small metal contraption (through which the target was filled with hydrogen) near the upstream end. All events that intersected this piece of metal at any point were eliminated. There were about 1000 such events.

Consideration was given to removing a small sample of events that went through another set of minor obstructions. These were chamber support posts, narrow aluminum dowels near the extreme end of the middle chambers. It was concluded that any event that was so significantly affected by a post to warrant cutting would have a false reconstructed track which would not pass through the post anyway. Those with tracks that reconstructed correctly through the post need not be removed. Therefore, no post cut was included.

In the next section, we describe the kinematic selection of $2\pi n$ and $3\pi n$ events that we have already mentioned.

F. Kinematic Event Definition

When searching for evidence of ω in the 2π n final state events of reaction (14) ($\pi^- p \rightarrow \pi^+\pi^- n$), it is important to have a sample of data that is free of reaction (13) ($\pi^- p \rightarrow \pi^+\pi^-\pi^o n$). In order to divide the data into these two classes of events, we studied distributions of two missing masses, M_y^2 and M_x^2, and took advantage of energy conservation for the 4 constraint 2π n events. M_y^2 is the mass squared of y in

$$\pi^- p \rightarrow \pi^+\pi^- y$$

and M_x^2 is the mass squared of x in

$$\pi^- p \rightarrow \pi^+\pi^- xn \ .$$

Ignoring the effects of resolution, for reaction (14)

$$M_y^2 = M_n^2$$

$$M_x^2 = 0$$

and for Reaction (13)

$$M_y^2 > (m_{\pi o} + m_n)^2 = 1.308\ m_n^2$$

$$M_x^2 = M_{\pi o}^2 \ .$$

A distribution of M_y^2 for all quadrant 1 and 3 events at this stage is shown in Fig. 13. Two clearly defined peaks corresponding to the two reaction channels of interest are visible. The M_y^2 cuts that were used to isolate these peaks were

Q13:

2π $\quad 0.73\ m_n^2 < M_y^2 < 1.23\ m_n^2$

3π $\quad M_y^2 > 1.27\ m_n^2$

Q12 and Q23:

$2\pi \qquad 0.70\ m_n^2 < M_y^2 < 1.22\ m_n^2$

$3\pi \qquad M_y^2 > 1.30\ m_n^2$.

The quadrant 1 and 3 cuts are shown on Fig. 12. Different cuts are used for the different quadrant combination because the resolution widths are not quite the same. It should be noted that the geometry of the experiment accepts virtually no $2\pi n$ events in other than quadrant 1 and 3.

The M_x^2 distributions of the preliminary samples of 2π and 3π events as defined above are shown in Fig. 13. The striking difference in the widths of the two peaks is at first surprising. This may be understood by writing out to first order the equation relating the width of M_x^2 to the various momentum resolutions. This is most profitably done by first writing M_x^2 in terms of the $2\pi n$ energy and momentum conservation variables ΔE and $\underset{\sim}{\Delta P}$:

$$M_x^2 = (\Delta E)^2 - (\underset{\sim}{\Delta P})^2$$

where

$$\Delta E = E_{beam} + E_{target} - E_n - E_{\pi+} - E_{\pi-}$$

and

$$\underset{\sim}{\Delta P} = \underset{\sim}{P}_{beam} + \underset{\sim}{P}_{target} - \underset{\sim}{P}_n - \underset{\sim}{P}_{\pi+} - \underset{\sim}{P}_{\pi-} \ .$$

Then we have for the resolution width of M_x^2

$$(\delta M_x^2) = (2\Delta E)^2(\delta E_{\pi-}^2 + \ldots) + (2\Delta P_x)^2(\delta P_{\pi-}^2 + \ldots) + \ldots$$

Each term of this expression includes as a factor one of the energy or momentum conservation variables, ΔE or ΔP, which are all zero for the $2\pi n$ events. To first order, then,

$\delta M_x^2 = 0$ for reaction (14) data. ΔE and ΔP are decidedly non-zero for reaction (13) events and so $\delta M_x^2 > 0$ for these events. This explains why the 2π peak is so much narrower than the 3π peak in the distributions of M_x^2 in Fig. 13. The narrowness of the 2π peak suggests that a cut on M_x^2 will be a good way to remove remaining 3π events from the 2π data. The following cuts (shown on Fig. 13) were made:

$$Q13: \quad -0.65\ m_{\pi o}^2 < M_x^2 < 0.20\ m_{\pi o}^2$$

$$\text{and } \left.\begin{matrix} Q12 \\ Q23 \end{matrix}\right\}: \quad -0.65\ m_{\pi o}^2 < M_x^2 < 0.35\ m_{\pi o}^2 \qquad 2\pi$$

On the other hand, no $2\pi n$ events would be removed from the 3π data by cutting on M_x^2 at this stage. Instead we look at the ΔE distribution (Fig. 14) in which the 3π events are better separated and make the following cuts.

$$Q13: \quad 70\ \text{MeV} < \Delta E < 550\ \text{MeV}$$

$$\text{and } \left.\begin{matrix} Q12 \\ Q23 \end{matrix}\right\}: \quad 25\ \text{MeV} < \Delta E < 582\ \text{MeV}\ . \qquad 3\pi$$

Finally to remove any last vestiges of contaminating events from the two samples of data, we use up the available information in these last two cuts:

$$-130 < \Delta E < 150 \qquad 2\pi$$

$$Q13 \quad -0.9\ m_{\pi o}^2 < M_x^2 < 3.25\ m_{\pi o}^2 \qquad 3\pi$$

$$\text{and } \left.\begin{matrix} Q12 \\ Q23 \end{matrix}\right\}: \quad -1.1\ m_{\pi o}^2 < M_x^2 < 3.2\ m_{\pi o}^2\ .$$

Defined in this way, we have a sample of 15801 reaction (13) (3π) events and 15281 reaction (14) (2π) events. From a Monte Carlo calculation, we estimate that there are less than

five $\omega \rightarrow 3\pi$ events contaminating the reaction (14) sample.

G. Final Input Parameter Calibration

Errors in the assumed values of such parameters as the field normalization, the beam momentum P_{beam}, and the distance of the neutron counters from the center of the hydrogen target d_o may shift the means of the $\Delta \underset{\sim}{P}$, ΔE, M_x^2 and M_y^2 distributions from their correct values. However, these correct values may be shifted somewhat from the expected values stated earlier by the kinematic definition cuts. Using a Monte Carlo program which includes resolution effects (see Sec. IV.B), we were able to simulate the effect of the kinematic selection and determine the correct centers of the various distributions for comparison with the $2\pi n$ data. If the field normalization is assumed to be correct, then in principle, any error in P_{beam} or d_o may be determined from the shifts of the ΔP_z and ΔE distributions. It was found that for the initially assumed values, P_{beam} = 1245 MeV/c and d_o = 31 ft, the centers of these distributions agreed with the Monte Carlo predictions within a few MeV. The field normalization assumed here has been checked as discussed in the section on the field map and in Sec. IV.e.

IV. ANALYSIS OF THE DATA

A. Outline of the Analysis

The focus of this analysis is on the 2π mass spectrum of reaction (14). In a spark chamber experiment of this nature, an understanding of the geometric efficiency of the apparatus

in different regions of phase space is essential. This information can best be determined with Monte Carlo techniques. Those used in this analysis are discussed in Sec. IV.B. In the following section, the $\omega \to 3\pi$ events are studied. Information on the dynamics of the $\omega \to 3\pi$ Dalitz plot is also obtained and the number of $\omega \to 3\pi$ events that were detected in the experiment is determined. The efficiency of the experiment at the ω mass in the 2π spectrum depends on possible correlations of the pion momenta due to alignment or polarization of the spin of their "parent" particle. In the event the parent particles are truly omegas, it is possible for us to determine their degree of alignment by studying the copious sample of $\omega \to 3\pi$ that is available in the data. The polarization theory that enables us to relate $\omega \to 2\pi$ pion correlations to $\omega \to 3\pi$ is discussed in Sec. IV.D and the degree of ω alignment found from the 3π data. Finally in the last group of sections, the 2π data are studied first with an eye to understanding the various components in the data and then to estimates of the possible size of any $\omega \to 2\pi$ effects.

B. Monte Carlo Programs

Monte Carlo programs were used in this analysis to simulate as accurately as possible the experimental apparatus and learn the efficiency and resolution of the equipment in different areas of the phase space of reactions (13) and (14). The efficiency programs can all be divided into three basic sections: An initial section generates events for the reaction being considered; A geometry section which never changes

determines if a given event will be accepted by the apparatus; and finally an analysis section provides histograms of appropriate quantities as the result.

Once an event has been accepted by the neutron counter geometry and time of flight restrictions, it has a 3-5% chance of passing acceptably through the spark chambers. The geometric efficiency of the neutron counters depends on the mass of the pion system but is always about 2%. As a result, a naively conceived program that generates events with the same weight in all parts of phase space will take an incredible amount of computer running time. It is possible, however, to study the dependence of the efficiency on various phase space variables. When this dependence is very strong, it is profitable to weigh the generation of events so that more are generated in the regions of high efficiency. As will be explained later, it is a simple matter to remove this weighting in the analysis section. Situations in which this technique may be applied are often very obvious. For example, because the neutron counters subtend a small angle in the forward direction, no events are accepted which are generated beyond a certain center of mass neutron angle θ. This cutoff angle comes at about $\cos\theta_c = 0.85$ for a pion system mass near 780 MeV and decreases at higher mass. Thus, one may cut off the neutron angle during generation at a number of different angles for different pion system masses and increase the Monte Carlo program efficiency from about a tenth of a percent to 10% or better. The relative weights W of events at different masses m may be determined from

$$W(m) = \frac{\int_{c(m)}^{1} f(\cos\theta)\,d\cos\theta}{\int_{-1}^{1} f(\cos\theta)\,d\cos\theta} \tag{21}$$

Here c(m) is the cutoff cosine at mass m, and $f(\cos\theta)$ is the shape of the $\cos\theta$ distribution after generation including any reaction dynamics. If the generation is pure phase space and no dynamics are assumed, then $f(\cos\theta) = 1$ and the calculation of W(m) is trivial.

This cutoff and weighting method has been applied wherever it seemed worthwhile in the Monte Carlo programs of this experiment and it has always reduced computing time. In the case of $2\pi n$ events, there are so many correlations that it was possible to increase the speed of the program from about 3300 to 50,000 events/hour on the Nevis 360/44 computer.

As will be seen in later sections, it was often necessary to include a large variety of production and decay dynamics in the Monte Carlo. This may be done, of course, during the generation phase of the Monte Carlo. Then one must rerun the whole program, geometry and all, each time a new dynamics is called for. However, as a glance at $f(\cos\theta)$ in Eq. (21) will show, the dynamic functions are just weighting functions that may be treated in the analysis section like the other weights. This made it possible to carry out three pure phase space high statistics Monte Carlo runs through the generating and geometry stages writing only successful events on tape. The tape was then read as often as necessary by the high speed analysis section of the Monte Carlo program which included various dynamic weightings and histogrammed relevant quantities.

In the few situations when it was necessary to analyze events with different dynamics at the generation stage (without geometry) it was simple and quick to regenerate the data.

In order to understand how the desired weighting and unweighting is handled at the analysis stage, it is useful to be somewhat mathematical. Let

$$d^nP = W(\underset{\sim}{\alpha}) \prod_i d\alpha_i \tag{22}$$

be the n-dimensional differential probability for an event to be generated in a volume of phase space defined by the n element vector $\underset{\sim}{\alpha}$. The n elements of $\underset{\sim}{\alpha}$ correspond to any complete set of phase space coordinates. The weight of the various regions of phase space at generation time is $W(\underset{\sim}{\alpha})$. If we want to know d^nP after the events are subjected to the geometry selection, we include a function

$$G(\underset{\sim}{\alpha}) = \begin{cases} 0 & \text{if events with phase space variables } \underset{\sim}{\alpha} \text{ fail geometry} \\ 1 & \text{if these events are accepted by the geometry.} \end{cases}$$

Then after geometry, we have simply

$$d^nP = G(\underset{\sim}{\alpha})W(\underset{\sim}{\alpha})\prod_i d\alpha_i \ . \tag{23}$$

When we histogram one of the phase space variables, say α_i, in the Monte Carlo analysis, we are just integrating over all of the elements of $\underset{\sim}{\alpha}$ except α_i. Normalized to one, the histogram distribution (in the limit of high statistics) will be just

$$N(\alpha_j)d\alpha_j = \int G(\underset{\sim}{\alpha})W(\underset{\sim}{\alpha}) \prod_{i\neq j} d\alpha_i \ . \tag{24}$$

(If we histogram a quantity that is not one of the α_i, we transform to a new set of α_i and include the Jacobean of the

transformation in the integral.) It is clear that if we wish to change the weight at generation time from $W(\underset{\sim}{\alpha})$ to, say $W_a(\underset{\sim}{\alpha})$, we just multiply the right side of Eq. (22) or (23) by $W_a(\underset{\sim}{\alpha})/W(\underset{\sim}{\alpha})$. To see the effect of such a change of weight on the histogram distribution $N(\alpha_i)$, this factor is included inside the integral of Eq. (24). But in practice, this just means that at the analysis stage, we add $W_a(\underset{\sim}{\alpha})/W(\underset{\sim}{\alpha})$ instead of 1 to the histogram bin corresponding to a given event. In this way, we will have changed weights just as effectively as if we regenerated the events. This is the technique that was used to remove the generation stage weights described earlier and to vary the dynamics at will while events were histogrammed.

In order to calculate the statistical errors of such weighted histograms, a second unweighted histogram was carried along. The percentage error $n_i^{-1/2}$, for n_i the number of events, was computed for each bin of the unweighted histogram and multiplied by the number in that bin of the weighted histogram to get the error of the main histogram.

Special techniques were used in the analysis section to reproduce the experimental resolution. Each event that was on the tape (and had already passed geometry) was passed through a program similar to the geometry program. This program redetermined the spark positions of the events and then moved them randomly with a gaussian width that included the chamber position resolution and multiple scattering combined in quadrature as was done during reconstruction in Eqs. (19)

and (20). The tracks were then reconstructed and new values of momentum and other quantities determined. To get the resolution of the neutron the time of flight of the neutron was calculated and then moved randomly with a gaussian width corresponding to the time resolution. The neutron momentum was then recalculated assuming the neutron hit the same point near the center of the neutron counter as was assumed in the reconstruction of actual events. The new values of the various quantities were written on a tape which then would be passed through the analysis program exactly as the no-resolution tape. The whole procedure depends on only two variables, σ_{ch} and σ_{TOF}, the chamber and time of flight measurement resolutions. Histogram distributions of various quantities (like ΔE and M_x^2) for resolution Monte Carlo events and real data can be compared for different values of σ_{ch} and σ_{TOF}. It was possible to obtain very good agreement between the two if σ_{TOF} was set at the value determined from the ω peak width (as described in Sec. II), $\sigma_{TOF} = 0.78$ nsec, and the chamber resolution set at $\sigma_{CH} = 0.037$ cm and these were the values finally used. Examples of the good agreement for these values in DZ, ΔE and Δm^2 distributions are shown in Fig. 15. The perfect agreement in the DZ distribution shows that σ_{CH} has been well set and that the spark chamber part of the Monte Carlo program is very accurate. The ΔE distribution also shows a good agreement except in the positive side tail which extends further in the data than the Monte Carlo. This

is because neutron scattering and complications in the beam momentum profile, two effects difficult to include, are not in the Monte Carlo. Later, we will need estimates from the Monte Carlo of the mass resolution in the 2π mass spectrum, and the Δm^2 distribution is a direct test of the mass resolution predictions. The quantity Δm^2 will be explained in Sec. IV.e. In this distribution, also, there is very good agreement between data and Monte Carlo except for the neutron scattering effect which shows up in the negative side tail.

C. Analysis of $\pi^- p \rightarrow \pi^+ \pi^- \pi^o n$ Data

The 15801 events which correspond to Reaction (13) according to the criterion described in Sec. III.F contain a large sample of omegas decaying to three pions. In order to determine exactly how many omega events there were, the omega Dalitz plot was divided up into 28 regions. These regions (shown on Fig. 16) each contain about the same number of events. They are bounded by contours in the Dalitz plot on which the quantity

$$q^2 = |\underset{\sim}{P}_+ \times \underset{\sim}{P}_-|^2 \tag{25}$$

is constant and by orthogonal lines where

$$\theta = \tan^{-1}\left(\frac{x}{y}\right) = \left\{\begin{matrix} \pm\pi \\ \pm 2 \\ \pm 0 \end{matrix}\right. .$$

The variables

$$x = \frac{\sqrt{3}}{Q}\,(T_{\pi^+} - T_{\pi^-}) \tag{25a}$$

and

$$y = \frac{3T_{\pi^o}}{Q} - 1$$

are the Dalitz plot coordinates in terms of the kinetic energies of the three pions $T_{\pi+}$, $T_{\pi-}$ and $T_{\pi o}$, and $Q = m_\omega - m_{\pi+} - m_{\pi-} - m_{\pi o}$. The time of flight spectrum of the data in each region was fit to a Gaussian plus a cubic polynomial background. The number of events in the Gaussian peak represents the number of omega events in the region. A fit to the complete sample of data from all regions gave $\sigma = 0.836 \pm 0.015$ nsec as the width of the Gaussian peak. The width and center of the Gaussian were set to the values determined in this overall fit in making the fits for each region. (The fit by regions was also done allowing the individual widths and centers to vary, and the results were essentially unchanged.) This technique is necessary because the fraction of background events varies over different regions of the Dalitz plot as may be seen from the representative time of flight spectra shown in Fig. 17. In Table II for each Dalitz plot region are listed the number of omega events and the fraction these are of the total. The error in the number of omegas in each region is calculated assuming the number of background events (N_{BG}) is statistically independent of the total number of events (N) in the region. Then the error in the number of omegas is the error in $N-N_{BG}$. By adding up all the regions, we find the total number of $\omega \rightarrow 3\pi$ events in our data:

$$N_{3\pi} = 7582 \pm 217 \ .$$

Here the error is just the statistical error of all the regions combined in quadrature. There is to be considered in addition

the systematic error resulting from the error in the width of the Gaussian which was held fixed in the fits. To determine the effect of the error in this width, we have also carried out the time of flight fits for each region assuming the width to be 0.855 nsec which is one standard deviation wider than the best value. These results are also listed in Table II, and the total number of $\omega \to 3\pi$ events computed with this width is

$$N_{3\pi} = 7698 \pm 209 \ .$$

Including both the statistical error and the error due to the width, we have

$$N_{3\pi} = 7582 \pm 325 \ .$$

In order to determine the asymmetry parameter, A, which is a test of C invariance, we sum the number of events on the left and right side of the Dalitz plot. Then

$$A = \frac{N_{LEFT} - N_{RIGHT}}{N_{3\pi}} = -0.014 \pm 0.028 \ .$$

The systematic error of the Gaussian width is included here just as for $N_{3\pi}$, but it does not increase the error of A. This result for the asymmetry is clearly consistent with zero and no C violation.

It is also interesting to use this information to study the matrix element dependence in the ω Dalitz plot. Here we must make use of an $\omega \to 3\pi$ Monte Carlo run to learn the efficiency of the experiment in different parts of the Dalitz plot. From the considerations to be discussed in Sec. IV.D, we would expect the simplest form of the matrix element squared for a $J^P = 1^-$ particle to be

$$|M|^2 \propto q^2 = |\underset{\sim}{P}_1 \times \underset{\sim}{P}_2|^2 ,$$

where the $\underset{\sim}{P}_i$ are the momenta of the pions in the ω rest frame. The background corrected data as a function of q^2 was compared with the expected form of this distribution as determined by the Monte Carlo for a simple q^2 dependence and a χ^2 computed using only the statistical error to test how good the agreement is between the data and Monte Carlo for this assumed matrix element. For 6 degrees of freedom, $\chi^2 = 5.1$. The data divided by the results of a pure phase space Monte Carlo run is shown in Fig. 18 and has the expected linear dependence on q^2. As Zemach has shown, the basic form of the Dalitz plot dependence recurs for every other spin value.[24] We would therefore expect a distribution peaking at the center and falling off at the edges, as it does in the data, if the spin of the omega were 1^- or 3^-. Flatte et al have pointed out that it is very hard to rule out 3^- absolutely on the basis of the Dalitz plot distribution, because it is always possible that the form factors conspire in such a manner that the Dalitz plot distribution of a 3^- omega reproduce the available data. Angular momentum barrier would tend to make the decay rate of a 3^- particle smaller than that of a 1^- particle. The relatively large 12.4 MeV width therefore supports the choice of 1^- for ω.[7]

The possibility of ρ dominance showing up in the matrix element was also investigated. A matrix element of this type would have the form[25]

$$|M|^2 \propto \frac{m_\rho^2 \Gamma_\rho^2}{(m^2-m_\rho^2)^2+m_\rho^2\Gamma_\rho^2} |\underset{\sim}{P}_1 \times \underset{\sim}{P}_2|^2 + \text{cyclic permutations.}$$

Here m_ρ = 760 MeV, Γ_ρ = 125 MeV and m_{ij} is the mass of the $\pi^i\pi^j$ system. We have looked for the possible effects of this matrix element in the data in two ways. First, we have prepared a Monte Carlo distribution of q^2 assuming ρ dominance. This curve is shown on Fig. 18 for comparison with the simple q^2 matrix element and the data. To see how well these matrix elements fit the data, we have computed χ^2 for each of the two hypotheses. Only the normalization of the Monte Carlo curves was allowed to vary in making the fits. For 6 degrees of freedom, χ^2 = 16.4 for ρ dominance and, as we stated earlier, χ^2 = 5.1 for the simple q^2 matrix element. We have also studied the dynamics of the ω Dalitz plot by looking directly at distributions of the 2π mass, m_{ij}, for each of the three combinations of two pions. Because of conservation of energy and momentum, the mass of one pair of pions depends only on the kinetic energy of the third pion. Thus, each of the three mass distributions is essentially just a projection of the Dalitz Plot density on one of the three pion kinetic energy axes. Studying these three mass distributions is therefore a test of the two matrix element hypotheses in different regions of the Dalitz plot. The distributions of data as a function of m_{ij} were prepared by subtracting the background in each bin using the same technique described earlier for the background subtraction as a function of q^2 and θ in the Dalitz plot. The distributions were then divided by a Monte Carlo determined distribution assuming the simple q^2 dependence and including the experimental efficiency. The resulting plots are shown

in Figs. 19a,b,c. If the matrix element is of the simplest 1^- form, $|M|^2 \propto q^2$ and free of ρ dominance, we would expect the data in these plots to fit a straight line. The best fit to this hypothesis is shown on each of the plots. Also shown is the best fit to a curve produced by the Monte Carlo assuming ρ dominance. Note that not only does this curve rise at the high end of the mass scale (which is about 100 MeV below the ρ pole) but it also rises slowly at the low end. This is a result of the fact that the three mass combinations are related through the energy and momentum conservation laws, so that if one mass combination tends to be high for a given event, the others will be low. The χ^2 for the two hypotheses for the q^2 plot and the three mass plots are summarized below:

plot	degrees of freedom	χ^2 no ρ dominance	χ^2 ρ dominance	
q^2	6	5.1	16.4	Fig. 18
m_{+0}	9	8.4	12.4	Fig. 19a
m_{-0}	9	6.5	13.3	Fig. 19b
m_{+-}	9	18.4	36.2	Fig. 19c

The effect of the ρ dominance matrix element is a tendency to pull events into the three outside corners of the Dalitz plot. The outside of the Dalitz plot, however, is heavily depleted by the required q^2 dependence of $J^P = 1^-$. This makes it difficult for any experiment to search for ρ dominance in ω decay with any precision. In spite of this, the results listed above are clearly more likely if the matrix element does not include ρ dominance than if it does.

D. Measurement of the Polarization Parameters and the Relative Experimental Efficiency

We now wish to use the distribution of events in the large sample of $\omega \to 3\pi$ to predict the pion angular correlations for a Monte Carlo study of $\omega \to 2\pi$. To understand the theory behind the technique we shall use, we need first to write the most general form of $d\sigma$ for the two reactions

$$\pi^- p \to \omega n$$
$$\hookrightarrow \begin{cases} \pi^+ \pi^- \pi^0 \\ \pi^+ \pi^- \end{cases}$$

and in doing this we will follow the approach of C. Zemach aimed at three pion decays of unstable particles.[24] In Zemach's scheme, we work in the ω-rest frame. We must find for both the ω production and decay states all distinguishable combinations of physical variables that, after including the intrinsic properties of the relevant particles, transform in the same way as an object with the intrinsic properties of the ω, $J^P = 1^-$. The most general combinations of variables of the production and decay states are then coupled to form a rotational invariant and get the general angular dependence of the matrix element.

The key to the value of this approach is that the only difference between $\omega \to 2\pi$ and $\omega \to 3\pi$ appears in the decay state. There we find that for $\omega \to 3\pi$ the only combination which transforms as a vector when the intrinsic 0^- character of three pions is included is

$$(3\pi) \quad \underset{\sim}{q} = \underset{\sim}{P}_+ \times \underset{\sim}{P}_- = \underset{\sim}{P}_- \times \underset{\sim}{P}_0 = \underset{\sim}{P}_0 \times \underset{\sim}{P}_+ \quad .$$

Here $\underset{\sim}{P}_+$, $\underset{\sim}{P}_-$, $\underset{\sim}{P}_o$ are the rest frame momenta of π^+, π^- and π^o. (The last two equalities follow from conservation of momentum, $\underset{\sim}{P}_+ + \underset{\sim}{P}_- + \underset{\sim}{P}_o = 0$.) For $\omega \to 2\pi$, there is also only one vector available:

$$(2\pi) \quad \underset{\sim}{q} = \underset{\sim}{P}_+ = - \underset{\sim}{P} \quad .$$

The neutron of the final state is thought of as going backward in time to join the π^- and proton and form the two nucleon and one pion production state. This state has negative intrinsic parity so it must transform as a pseudovector. There are six pseudovectors that may be made out of $\underset{\sim}{P}$ (the beam momentum), $\underset{\sim}{P}_T$ (the target nucleon momentum), and $\underset{\sim}{\sigma}$ (the spin vector of the nucleon). They are

1. $\underset{\sim}{Q} = \underset{\sim}{P} \times \underset{\sim}{P}_T$
2. $\underset{\sim}{\sigma}$
3. $(\underset{\sim}{\sigma} \cdot \underset{\sim}{P})\underset{\sim}{P}$
4. $(\underset{\sim}{\sigma} \cdot \underset{\sim}{P})\underset{\sim}{Q} \times \underset{\sim}{P} \equiv (\underset{\sim}{\sigma} \cdot \underset{\sim}{P})\underset{\sim}{R}$
5. $(\underset{\sim}{\sigma} \cdot \underset{\sim}{R})\underset{\sim}{P}$
6. $(\underset{\sim}{\sigma} \cdot \underset{\sim}{R})\underset{\sim}{R}$.

All these production and decay vectors are shown in Fig. 20.

We are now in a position to write the angular dependence of $d\sigma$ for an unpolarized beam:

$$d^n\sigma \propto \sum_{\pm\frac{1}{2},\pm\frac{1}{2}} \left| \langle \pm\tfrac{1}{2} | [f_1 \underset{\sim}{Q} + f_2 \underset{\sim}{\sigma} + f_3 (\underset{\sim}{\sigma}\cdot\underset{\sim}{P})\underset{\sim}{P} + f_4 (\underset{\sim}{\sigma}\cdot\underset{\sim}{P})\underset{\sim}{R} + f_5 (\underset{\sim}{\sigma}\cdot\underset{\sim}{R})\underset{\sim}{P} + f_6 (\underset{\sim}{\sigma}\cdot\underset{\sim}{R})\underset{\sim}{R}] \cdot \underset{\sim}{q} | \pm\tfrac{1}{2} \rangle \right|^2 \prod_i d\alpha_i \quad . \tag{26}$$

Here the bra and ket vectors indicate the nucleon spin state before and after the event, the f_i are form factors

independent of angle that may depend on any scalar like P^2, and the α_i represent a set of phase space variables just as in Sec. IV.B. If we carry out the sums and square, we end up with four different types of terms. For A and B any two general real vectors, these four types of terms are

$$\Sigma|\langle\pm|\underset{\sim}{A}\cdot\underset{\sim}{B}|\pm\rangle|^2 = |\underset{\sim}{A}\cdot\underset{\sim}{B}|^2 \qquad \text{(I)}$$

$$\begin{aligned}\Sigma|\langle\pm|\underset{\sim}{\sigma}\cdot\underset{\sim}{A}|\pm\rangle|^2 &= |\langle+|\sigma_z A_z|+\rangle|^2+|\langle-|\sigma_z A_z|-\rangle|^2 \\ &\quad + |\langle+|\tfrac{1}{2}\sigma_+ A_-|-\rangle|^2+|\langle-|\tfrac{1}{2}\sigma_- A_+|+\rangle|^2 \\ &= A^2(\tfrac{1}{4}\cos^2\theta+\tfrac{1}{4}\cos^2\theta+\tfrac{1}{4}\sin^2\theta+\tfrac{1}{4}\sin^2\theta) \\ &= \tfrac{1}{2}A^2 \qquad \text{(II)}\end{aligned}$$

$$\begin{aligned}\Sigma 2\mathrm{Re}(f_a f_b^*\langle\pm|\underset{\sim}{\sigma}\cdot\underset{\sim}{A}|\pm\rangle\langle\pm|\underset{\sim}{\sigma}\cdot\underset{\sim}{B}|\pm\rangle^*) &= (2\mathrm{Re}[f_a f_b^*(\tfrac{1}{4}A_z B_z+\tfrac{1}{4}A_z B_z \\ &\quad +\tfrac{1}{4}A_+ B_+^*+\tfrac{1}{4}A_- B_-^*)] \\ &= \mathrm{Re}(f_a f_b^*)\underset{\sim}{A}\cdot\underset{\sim}{B} \qquad \text{(III)}\end{aligned}$$

$$\Sigma 2\mathrm{Re}(\langle\pm|\underset{\sim}{A}\cdot\underset{\sim}{B}|\pm\rangle\langle\pm|\underset{\sim}{\sigma}\cdot\underset{\sim}{B}|\pm\rangle^*) = 2\mathrm{Re}(\underset{\sim}{A}\cdot\underset{\sim}{B}(\tfrac{1}{2}B_z-\tfrac{1}{2}B_z)) = 0 \ . \qquad \text{(IV)}$$

We are now able to compute all terms of Eq. (26) using these results. We collect terms and make use of the fact that $\underset{\sim}{P}\cdot\underset{\sim}{R} = 0$ and that

$$(\underset{\sim}{Q}\cdot\underset{\sim}{q})^2 + (\underset{\sim}{P}\cdot\underset{\sim}{q})^2 + (\underset{\sim}{R}\cdot\underset{\sim}{q})^2 = 1$$

since $\underset{\sim}{P}$, $\underset{\sim}{Q}$, and $\underset{\sim}{R}$ are perpendicular.

Finally, we have

$$d^n\sigma = [F_1+F_2(\hat{\underset{\sim}{P}}\cdot\hat{\underset{\sim}{q}})^2+F_3(\hat{\underset{\sim}{R}}\cdot\hat{\underset{\sim}{q}})^2+F_4(\hat{\underset{\sim}{P}}\cdot\hat{\underset{\sim}{Q}})(\hat{\underset{\sim}{R}}\cdot\hat{\underset{\sim}{q}})]\prod_i d\alpha_i \ . \qquad (27)$$

The F_i are a new set of form factors that include all but the purely angular dependence. In the limit of forward production of the neutron

$$\underset{\sim}{Q} = \underset{\sim}{P} \times \underset{\sim}{P}_T = 0$$

and R = 0 so

$$\frac{d\sigma}{du} = (F_1+F_2u^2)P(u)du = n[(1-\alpha)+\alpha u^2]du \qquad (28)$$

where $u = \hat{\underset{\sim}{P}}\cdot\hat{\underset{\sim}{q}}$ and P(u) contains the phase space dependence that remains after integrating Eq. (27) over every variable but u. In the alternate parameterization given in Eq. (28) n is a normalization factor and α measures the amount of alignment ranging from 0 to 1.

Since neutrons in our experiment were produced so predominately forward, it became apparent very early in our analysis that very little information could be learned from the data regarding F_3 and F_4. Accordingly, we concentrated on Eq. (28) in analyzing the spin alignment of the omegas. It is, of course, possible to calculate u for each $\omega \to 3\pi$ event and fit Eq. (28) to a histogram distribution of u. However, u is an ω rest frame quantity and its determination involves a Lorentz transformation that requires a good knowledge of the neutron momentum. In order to avoid the complications introduced by the resolution functions of the neutron counters, the alignment was studied in terms of the quantity

$$q_z^{lab} = (\underset{\sim}{P}_+ \times \underset{\sim}{P}_-)_z$$

which is evaluated in the lab. A background corrected histogram of q_z^{lab} is shown in Fig. 21. The background subtraction was performed for each bin of q_z^{lab} as described in the last section. The data distribution was fit to a linear sum of

normalized curves corresponding to Monte Carlo calculations of the expected q_z^{lab} distributions for complete and no alignment, $\alpha = 1$ and $\alpha = 0$ respectively. The best fit shown on Fig. 21 gave $\alpha = 0.004 \begin{smallmatrix}+0.16\\-0.004\end{smallmatrix}$ and $\chi^2 = 26$ for 19 degrees of freedom. (When only central neutron counter events were included, the results for α remained the same but χ^2 reduced to 14.) We conclude from this that the omegas are essentially unaligned.

This information may now be used in conjunction with two Monte Carlo runs to determine the relative efficiency of the experiment to the decays $\omega \to 3\pi$ and $\omega \to 2\pi$. With q as defined earlier for two and three pions, a Monte Carlo run determined the efficiency for each of the reactions for ten different values of α. The results are shown in Table III. Taking into account the error in the fit value of α, we determine the ratio of efficiencies to be

$$\frac{\epsilon_{3\pi}}{\epsilon_{2\pi}} = 0.6474 \begin{smallmatrix}+0.014\\-0.004\end{smallmatrix} \quad .$$

E. The 2π Mass Spectrum and Its Calibration

The mass of the two pions, m, for events classified in the reaction $\pi^- p \to \pi^+ \pi^- n$, may be computed in two different ways in this experiment since all final state momenta (including that of the neutron) have been measured. The mass may be computed directly from the two pion momenta

$$m_{2\pi} = ((E_+ + E_-)^2 - (\underset{\sim}{P}_+ + \underset{\sim}{P}_-)^2)^{1/2} \quad ,$$

or it may be computed from the missing mass of **z** in $\pi^- p \rightarrow zn$

$$m_z = ((E_{beam} + m_p - E_n)^2 - (\underset{\sim}{p}_{beam} - \underset{\sim}{p}_n)^2)^{1/2} ,$$

which essentially depends on the time of flight measurement. Monte Carlo studies indicate that the mass resolutions of $m_{2\pi}$ and m_z are virtually identical at the ω mass. It is thus profitable to use $m \doteq \frac{1}{2}(m_{2\pi}+m_z)$ and improve the resolution of m by a factor of $\sqrt{2}$. This is the definition of the two pion mass that will be used in analyzing the 2π mass spectrum.

The techniques used in the Monte Carlo generation of the experimental resolution were discussed in Sec. IV.B. A histogram of the quantity

$$\Delta(m^2) = m_{2\pi}^{\ 2} - m_z^{\ 2}$$

in the data and the curve predicted by the Monte Carlo are shown in Fig. 15. The good agreement is the best test of the accuracy of the Monte Carlo resolution program in the 2π mass spectrum itself since the shape and width of Δm are obviously closely related to the resolution functions of $m_{2\pi}$ and m_z.

The quantity Δm is very useful in checking the final calibration of the absolute mass scale. This is so since m_z which depends only on the neutron measurement has been precisely calibrated at the ω mass ($\pm \leqslant 1.0$ MeV by the fit to the ω peak in the time of flight spectrum of the 3π data. Then by checking

to see if $\Delta m = 0$ at the peak of the Δm distribution for the 2π data, we may force $m_{2\pi}$ to be calibrated correctly ($\pm \sim 3$ MeV) at the ω mass. This checks the accuracy of the assumed normalization of the magnetic field in the pion spectrometer. It also allows us to be confident that the absolute value of m at the central ω mass is correct to $\pm \sim 1.6$ MeV.

In Fig. 22 a histogrammed distribution of m for events classified as belonging to the reaction $\pi^- p \rightarrow \pi^+ \pi^- n$ is compared with the phase space predicted by a Monte Carlo program assuming no matrix element dynamics. Events below a mass of 670 have been eliminated to avoid problems with the neutron time of flight gate electronics which begins to cut in at this point. There are 9696 events left in the distribution. The dynamical aspects of this spectrum become most obvious if we divide the data by the Monte Carlo distributions. This removes all phase space and efficiency dependence. The resulting distribution, which we shall be studying from here on, is shown in Fig. 23.

A first glance at this distribution shows that not only is there no striking effect at the ω mass, but that the ρ is not as prominent as one might expect. However, a moments thought explains why: ρ production governed, as it is, by one pion exchange tends to produce ρ that go forward and neutrons that go backward in the center of mass, or, equivalently, the ρ production cross section is largest for momentum transfer $t \leqslant 0.3$ $(\mathrm{BeV}/c)^2$. Since the neutron counters are very much forward in the lab, and because of the time of flight gate,

no neutrons that go backward in the CM are accepted by the experiment. As a result, the momentum transfer distribution looks as it does in Fig. 24 with $0.55 \leq t \leq 1.2$, and ρ production is not as heavy as would otherwise be the case. ρ still is produced in the experiment, and as we shall see, ρ production corresponds to about a third of all events. The ρ production becomes much more evident in the 2π mass spectrum if we remove some of the background. As will be discussed in the next section, this background is dominated by the N^{*-} resonance. Therefore, cuts of $M_{\pi^-n} > 1300$ MeV and $M_{\pi^-n} > 1360$ selectively remove a large fraction of the N^{*-} background. 2π mass spectrum plots of the data with these cuts are shown in Fig. 29. In these figures the ρ is more prominent than in Fig. 23. It is clear from these figures that a large background sloping down as m increases must accompany the ρ to account for the shape of the data in Fig. 23. In the next section, we will discuss this background. Limits on the minimum number of ρ in the data will be discussed in the section on systematic error.

F. Background in the 2π Mass Spectrum

Histograms of the π^-n and π^+n spectra are shown in Fig. 25. In the π^-n plot there is a heavy enhancement due to N^* near the low end of the spectrum near $M_{\pi^-n} = 1236$ MeV. A curve corresponding to pure phase space as predicted by the Monte Carlo is shown on these figures. Also shown on each histogram is a curve corresponding to 40% pure phase space and 60% an N^{*-} resonance in the π^-n spectrum at 1236 MeV with width 120 MeV. Fits to

the 2π mass spectrum that will be discussed later show that the background corresponds to about 2/3 of the data. The heavy N^* enhancement in these histograms indicates that N^* accounts for a large fraction of this. Therefore, as an order of magnitude, the N^{*-} resonance accounts for something like 60% of the data. This order of magnitude has been used in preparing the curves for Fig. 25 which are only meant to demonstrate the presence of data due to the N^{*-} resonance. Because of the shape of the kinematic boundary of the $M_{\pi^-n}^2$ vs $M_{\pi^+n}^2$ phase space, a resonance near the low end of the M_{π^-n} scale shows up as an enhancement near the high end of M_{π^+n}. The N^{*-} resonance therefore is reflected into a rise at the high end of the π^+n spectrum in the data. There is no evidence for a π^+n resonance near 1236 MeV. However, the two histograms of Fig. 25 clearly do show evidence of an N^* resonance of the π^- and the neutron.

The large amount of N^{*-} and lack of evidence for N^{*+} in this reaction is in agreement with a number of earlier experiments that have studied $\pi^-p \rightarrow \pi^+\pi^-n$ near 1-2 BeV/c.[26] The fraction of data corresponding to the N^{*-} resonance is also in rough qualitative agreement with these experiments.[26] The experiment of Banner et al[27] run at an incident momentum of 1000 MeV/c measured the center of mass production angle distribution of the π^-n system for this reaction. The distribution in the center of mass, corrected for efficiency, of

$$\cos\theta_c = \hat{\underset{\sim}{P}}_{\pi^- n} \cdot \hat{\underset{\sim}{P}}_{inc}$$

in our experiment for events in the N^* region ($M_{\pi^- n} \leq 1300$ MeV) is shown in Fig. 26. In making the efficiency correction, the Breit Wigner resonance form of the N^{*-} was assumed for the Monte Carlo calculation. In the region of sensitivity of this experiment the results agree well with a Legendre polynomial fit made by Banner et al to their data.[27] Their fit for events in the region 1200 MeV $\leq M_{\pi^- n} \leq$ 1300 MeV is shown on Fig. 26.

We noted in the last section that underneath the ρ in the 2π mass plot of Fig. 23 the background apparently slopes down towards small values at the upper limit of m. According to a Monte Carlo prediction, an N^* Breit Wigner in the $\pi^- n$ spectrum combined with the production angle distribution of Banner et al appears as a relatively flat curve in the 2π mass plot. Thus, it is not possible to explain the background shape in the 2π spectrum with the facts we have already mentioned about the N^* data. It is conceivable that momentum dependence at the vertices of the various possible diagrams for N^* could explain some part of the shape of this background. It is also possible that the efficiency of the neutron counters was dependent on the neutron momentum and therefore on the 2π mass. Since we know very little about this dependence, it was not included in the Monte Carlo calculations and therefore not corrected for. An explanation which is quite likely and at any rate easier to discuss is the possibility of correlations in θ_n, the neutron decay angle in the $\pi^- n$ rest frame. This

angle is very closely related to the 2π mass m, since in the center of mass

$$m^2 = (E_{inc} - E_n)^2 - \underset{\sim}{p}_n^{\,2}$$
$$= E_{inc}^{\,2} + m_n^{\,2} - 2E_{inc}E_n \quad .$$

The 2π mass m, thus, depends on the center of mass neutron energy, E_n, which in turn depends on the decay angle, θ_n, in the π^-n rest frame. Therefore, any decay angle correlation in the rest frame of a π^-n resonance will show up directly in a distribution of the 2π mass m. We choose to define θ_n as the angle the neutron makes in the π^-n rest frame with the z axis. (z is the direction of the incident pion in the lab or CM). It is shown in Appendix II that with this choice of axis the most general form of the distribution in θ_n for a spin 3/2 π^-n resonance in this experiment is

$$F(\theta_n) = 1 + a\cos^2\theta_n + b\cos\theta_n\sin\theta_n \tag{29}$$

providing the target is unpolarized and we average over the azimuthal decay angle. The Monte Carlo predicted effects of a flat distribution, of a $\cos^2\theta_n$ distribution, and of a $\cos\theta_n \sin\theta_n$ on the 2π mass spectrum are shown in Fig. 27. It is evident from this figure that both the $\cos^2\theta_n$ and $\cos\theta_n\sin\theta_n$ distributions have slopes in the same direction as the background of the data.

From the analysis in Appendix II, we see that if the N^* is produced as a pure partial wave, $F(\theta_n)$ will be a characteristic non-uniform distribution. For example, if the production is S-wave, then

$$F_S(\theta_n) = 1 + 3\cos^2\theta_n \quad .$$

(This is also the characteristic decay distribution of N^* in two body final states,[28] as well as of N^* produced forward in three body final states like that of this experiment.) It is well known that quite a number of partial waves contribute significantly to the production of N^* in $\pi^- p \to \pi^+\pi^- n$.[29] In principle, it is possible to predict the form of $F(\theta_n)$ if the relative weights of the various partial waves are known. The present knowledge of these weights, however, allows virtually any distribution consistent with Eq. (29). Most likely the parameter $a \neq 0$ since it would require a very fortuitous combination of partial waves for $F(\theta_n)$ to turn out to be uniform.

In concluding this discussion of the background, we note that it is very difficult to separate the N^* and ρ data in this experiment since there is a large overlap in the $M_{\pi^- n}^2 \times m^2$ Dalitz plot. This Dalitz plot (corrected for efficiency) is shown in Fig. 28. We have attempted to remove some of the N^* when studying the 2π mass m by cutting at 1300 MeV and 1360 MeV (corresponding to about one and two half widths of the N^* above 1236) as shown in Fig. 29. The ρ is clearly more prominent after these cuts are made than in Fig. 23. However, the loss of statistics will reduce the sensitivity of the measurement of $\omega \to 2\pi$ which is the main object of this experiment.

G. Fitting the 2π Mass Spectrum

When fitting the 2π mass distribution to measure the size of the $\omega \to 2\pi$ effect, we make the following assumptions:

a. The distribution of events takes the form of Eq. (11) derived in Sec. 1 with[30]

$$m_\rho = 765 \text{ MeV}$$
$$\Gamma_\rho = 125 \text{ MeV}$$
$$m_\omega = 783.4 \text{ MeV}$$
$$\Gamma_\omega = 12.2 \text{ MeV} .$$

b. The background is all N^{*-} (1236 MeV) produced according to the angular distribution of Banner et al,[27] and decaying in the general form of Eq. (29), discussed in the last section, with b = 0,

$$F(\theta_n) = 1 + a\cos^2\theta_n \quad . \tag{29}$$

We set b = 0 in making the fit to the 2π mass spectrum because the $\cos^2\theta_n$ and $\cos\theta_n\sin\theta_n$ distributions have similar shapes in the 2π mass spectrum (see Fig. 27), and in practice the fitting procedure cannot distinguish them.

c. There is no interference between the N^{*-} background and the ρ and ω. This assumption may be justified by the completely different production mechanisms involved for nucleon and pion resonances in our reaction.

The possible systematic errors introduced into the results by these assumptions are discussed in the next section.

The fit was made to the sum of a set of Monte Carlo generated distributions. Each distribution was prepared by reading the $\pi\pi n$ Monte Carlo tape that included the experiment's resolution (as described in Sec. IV.B) and making a histogram of the resolution shifted mass weighted by an appropriate function (of non-resolution shifted quantities) that defined the particular dynamical character of the distribution. Each distribution was then divided by the purely phase space Monte Carlo spectrum just as the data was for Fig. 23. These distributions automatically contain the Monte Carlo determined mass resolution function. They correspond to each of the three terms and background of Eq. (11) in Sec. 1. The background of Eq. (11) is here assumed to consist of two distributions each weighted by one of the first two terms of Eq. (29) for the decay distribution of N^*. These two terms which each include the N^{*-} Breit Wigner and production angular distribution will be referred to as BG_{flat} and BG_{cos^2}. All the distributions are shown in Fig. 27 and their weight functions defined in Table IV.

Since we have no way of knowing the degree of coherence of the ω-ρ interference, we analyze the data for a series of assumptions of relative ω-ρ phase and degree of coherence. We consider first the cases of complete coherence with constructive or destructive interference ($\phi = \pm \frac{\pi}{2}$) as well as the case of total incoherence, deferring until later such possibilities as $\phi = 0$ or π. A fit was therefore made to the hypothesis

$$N_{2\pi}(m) = \alpha_1 BW_\rho^{\ 2} + \alpha_2 BW_\rho^{\ 2}|F_\omega|^2 + b_1\ BG_{flat} + b_2\ BG_{cos^2} \qquad (30)$$

which corresponds to Eq. (11) with $\alpha_3 = 0$. The fit gave $\chi^2=29.6$ for 18 degrees of freedom and the best values listed below:

$$\alpha_1 = (5.15 \pm 0.76) \times 10^3$$
$$\alpha_2 = (1.05 \pm 1.39) \times 10^{11}$$
$$b_1 = (3.84 \pm 1.46) \times 10^{-2}$$
$$b_2 = (7.43 \pm 0.32) \times 10^{-1} .$$

(All errors cited in this section are purely statistical. Systematic errors will be considered in the next section.) The best fit to Eq. (30) is shown on Fig. 23. From the results of this fit, we find that the number of ρ and background events in the data are:

$$N_\rho = \alpha_1 I_{RHO} = 2887 \pm 424$$
$$N_{BG} = b_1 I_{BG_{flat}} + b_2 I_{BG_{\cos^2}} = 6657 \pm 380 .$$

The number of events corresponding to the experimental size of the $\omega \to 2\pi$ effect including the enhancement or suppressive effects of any ρ-ω interference is

$$N_{exp} = \alpha_2 I_{OMEGA} = 75 \pm 100 .$$

As we already noted in the theoretical introduction, the imaginary part of the Breit Wigner amplitude is indistinguishable in practice from the Breit Wigner amplitude squared. For this reason, we were forced to combine the second and fourth terms of Eq.(6) into the second term of Eq. (11) and Eq. (30) for the actual fit. Thus the experimental number, N_{exp}, includes both $N_{\omega\to 2\pi}$ (which would be the number of $\omega\to 2\pi$ in the absence of ρ) and an interference term. It is possible to separate

$N_{\omega\to 2\pi}$ from N_{exp} if we make assumptions about the relative phase, ϕ, and the degree of coherence, c, since we know the size of the ρ amplitude from the first term of the fit. To do this, we recall two of the relations of Eq. (11a):

$$\begin{aligned} \alpha_1 &= |A_\rho|^2 \\ \alpha_2 &= |a_\omega(m^2-M_\rho^2)|^2 - 2cm_\omega\Gamma_\omega|A_\rho^* a_\omega(m^2-M_\rho^2)|\sin\phi \\ &= |\tilde{a}_\omega|^2 - 2cm_\omega\Gamma_\omega|A_\rho^*\tilde{a}_\omega|\sin\phi \ . \end{aligned} \tag{11a}$$

We are interested in using these equations to solve for

$$|\tilde{a}_\omega| = |a_\omega(m^2-M_\rho^2)|$$

since $N_{\omega\to 2\pi} = |\tilde{a}_\omega|^2 \, I_{OMEGA}$ is the number we are looking for. For the cases of destructive and constructive interference, $\phi = \pm\frac{\pi}{2}$, we have the following quadratic equation for $|\tilde{a}_\omega|$:

$$|\tilde{a}_\omega|^2 - (\pm cm_\omega\Gamma_\omega\sqrt{\alpha_1})|\tilde{a}_\omega| - \alpha_2 = 0 \ .$$

Using the fit value of α_1 and defining

$$k = m_\omega\Gamma_\omega|A_\rho^*| = (6.86 \pm 0.50) \times 10^5 \ ,$$

the solution of the quadratic equation is

$$|\tilde{a}_\omega| = (\pm ck) + \sqrt{(ck)^2+\alpha_2} \ . \tag{31}$$

We have chosen the + sign in the quadratic formula of Eq. (31) so that $|\tilde{a}_\omega|>0$ since $ck > 0$. The case of destructive interference ($\phi = +\frac{\pi}{2}$) corresponds to Eq. (31) with the + sign before ck so that, if there is coherence ($c\approx 1$), $|\tilde{a}_\omega|^2$ may be very large even if the experiment observes no $\omega \to 2\pi$ effect. But for constructive interference ($\phi = -\frac{\pi}{2}$), a very small intrinsic $\omega\to 2\pi$ effect will result in a significantly large experimental effect, since in this situation,

$$|\tilde{a}_\omega| \simeq \left(\frac{\alpha_2}{4k^2}\right)\alpha_2 \approx \frac{1}{19}\,\alpha_2 \tag{32}$$

for the relative size of α_1 and α_2 in our data.

By squaring Eq. (31) and multiplying by I_{OMEGA}, we can determine $N_{\omega\to 2\pi}$ from the fit to Eq. (30) for $\phi = \pm \frac{\pi}{2}$ and any degree of coherence, c. Using earlier results for the value of

$$\frac{1}{N_{\omega\to 3\pi}} \frac{\epsilon_{3\pi}}{\epsilon_{2\pi}}$$

we may determine the branching ratio

$$B = \frac{N_{\omega\to 2\pi}}{N_{\omega\to 3\pi}} \frac{\epsilon_{3\pi}}{\epsilon_{2\pi}} = \frac{N_{\omega\to 2\pi}}{11700} \quad .$$

Also it will be recalled from the theoretical section that the mixing parameter $\delta' = \delta + (m_\omega - m_\rho + i\frac{\Gamma_\rho}{2}) T_{\omega\to 2\pi}/T_\rho$ is related to the branching ratio according to $\delta' = 20.6\ B^{1/2}$ MeV. The values of these quantities derived from the fit to Eq. (30) are listed below:

$N_{\omega\to 2\pi} = 75 \pm 100$ incoherence

$B = (0.64 \pm 0.86) \times 10^{-2}$

$\delta' = 1.65\ ^{+0.87}_{-1.65}$ MeV .

$N_{\omega\to 2\pi} = 1499 \pm 186$ coherence

$B = (12.8 \pm 1.6) \times 10^{-2}$ destructive interference

$\delta' = 7.36\ ^{+0.45}_{-0.48}$ MeV . $\phi = +\frac{\pi}{2}$

$N_{\omega\to 2\pi} = 3.8 \pm 9.9$ constructive interference

$B = (0.032 \pm 0.084) \times 10^{-2}$ $\phi = -\frac{\pi}{2}$

$\delta' = 0.37\ ^{+0.33}_{-0.37}$ MeV .

In order to consider the situation where $\phi = 0$ or π, we have also made a fit to

$$N_{2\pi}(m) = \alpha_1 BW_\rho^2 + \alpha_2 BW_\rho^2 |F_\omega|^2 + \alpha_3 BW_\rho^2 \mathrm{Re}F_\omega + b_1 BG_{flat} + b_2 BG_{cos^2} . \quad (33)$$

For 17 degrees of freedom, $\chi^2 = 22.0$, and

$$\alpha_1 = (2.90 \pm 1.11) \times 10^3$$
$$\alpha_2 = (1.98 \pm 1.43) \times 10^{11}$$
$$\alpha_3 = (-5.25 \pm 1.90) \times 10^7$$
$$b_1 = (9.0 \pm 2.4) \times 10^{-2}$$
$$b_2 = (6.72 \pm 0.41) \times 10^{-1} .$$

The best fit to Eq. (33) is shown on Fig. 23. For this fit, we find

$$N_\rho = 1630 \pm 620$$
$$N_{BG} = 7650 \pm 520$$

and the number of events corresponding to the $\omega \to 2\pi$ effect is

$$N_{exp} = \alpha_2 I_{OMEGA} + \alpha_3 I_{REOM} = 360 \pm 140 .$$

The results of this fit are consistent with a small $\omega \to 2\pi$ effect with $\phi = \pi$ and complete coherence. This is so since if we assume that ϕ equals either 0 or π and allow the degree of coherence, c, to vary, we find that $\phi=\pi$ (not 0) because α_3 is negative. We also have from Eqs. (11a), for $\phi=\pi$,

$$c = -\frac{\alpha_3}{\sqrt{\alpha_1\alpha_2}} = 1.1 \pm 0.6$$

which is consistent with complete coherence. For this assumption (from Eqs. (11a) again),

$$|\tilde{a}_\omega|^2 = \alpha_2$$

since $\alpha_4 = 0$ for $\phi = \pi$. Thus we have for the branching ratio and mixing parameter

$$B = (1.22 \pm 0.88) \times 10^{-2}$$
$$\delta' = 2.27^{+0.71}_{-1.08} \text{ MeV.} \qquad \phi = \pi$$

The Berkeley group[16] observed a change at the ω mass in the angular distribution of the pions in the 2π rest frame .

We have studied the distribution of

$$\cos\theta = \hat{\underset{\sim}{P}}_{\pi^+} \cdot \hat{\underset{\sim}{P}}_{beam}$$

for a succession of 20 MeV mass regions and can observe no change near the ω mass. A selection of these distributions, corrected by dividing out the Monte Carlo determined efficiency, is shown in Fig. 30. It should be noted that this experiment is completely insensitive near $\cos\theta = \pm 1$ because of the spark chamber geometry, and this is the region in which a change near the ω mass might be expected.

It was suggested earlier that the ω-ρ interference phase, ϕ, depends on production and decay variables like momentum transfer, t, and decay angle, θ. As a result, the fact that the experiment covers a finite range of such variables means that the ω-ρ interference will be reduced by some unknown amount. As a check to see if we might have missed some sharp effect at the ω mass by studying all the data at once, we have prepared 2π mass spectrum plots for several regions of $\cos\theta$. These are shown in Fig. 31 where it can be seen that there are no clear effects at the ω mass in any region of $\cos\theta$. This is no surprise since the only dependence of ϕ on decay variables like $\cos\theta$ is through the direct $\omega \to 2\pi$ transition amplitude T_ω which is presumed to be very small (see Eqs. (4a) and (7a). It is not possible to divide the data into different regions of momentum transfer, t, to study the mass distribution since the 2π mass, m, and t are very strongly correlated by the kinematics of the experiment. The data as a function of

m and t is shown in Fig. 32. The fact that the ω mass appears only for the limited range $0.6 \leqslant t \leqslant 0.9$ GeV/c^2 is further support for the possibility that ω and ρ are coherently produced in this experiment.

H. Systematic Errors

The results of the last section depend on the accuracy of the following:

a. The assumptions concerning the ρ mass and width.

b. The calibration of the 2π mass scale.

c. The Monte Carlo prediction of the resolution function which was implicit in each of the distributions used in the fits.

d. The assumed form of the background.

Each of these factors may contribute some error to the results. We will consider the magnitude of these systematic errors in this section.

The Particle Data Group has cited the following values of the mass and width of the ρ in their January 1969 listings:[30]

$$m_\rho = 765 \pm 10 \text{ MeV}$$

$$\Gamma_\rho = 125 \pm 20 \text{ MeV} .$$

In their words, these values "...are not average values from various experiments, but rather are intended to give the range where we believe the actual values are most likely to fall." In this spirit, we assume that the ρ mass and width may fall with equal probability anywhere in their ranges. In order to determine the effect of these uncertainties on our results, we have carried out the fits and calculations of the preceding

section for nine combinations of m_ρ and Γ_ρ corresponding to the two ends and center of the ranges of these two parameters in all combinations. The results are listed in Table V. The maximum and minimum values of the branching ratio and mixing parameter in Table V indicate the error caused by the lack of knowledge of the ρ parameters.

As discussed in Sec. IV.E, the mass scale calibration is accurate to ± ~1.6 MeV. This error is considerably less than the error in the ρ mass. Since the essential effect of a shift in the mass calibration is to shift the ρ peak, it is clear that the errors in the results due to the small uncertainty in scale calibration may be neglected compared with those due to the ρ mass.

The error in the width of the resolution function depends on the uncertainty in two quantities discussed in Sec. IV.B, the time of flight resolution width, $\sigma_{TOF} = 0.78 \pm 0.02$ nsec, and the chamber resolution width, $\sigma_{CH} = 0.037 \pm 0.002$ cm. The error in σ_{TOF} is known from the fit to the 3π time of flight spectrum (Sec. IV.C) and results in an error in our knowledge of the resolution width of m_z (the 2π mass determined from the neutron momentum) of about 2 1/2%. The error in σ_{CH} is known from comparisons of Monte Carlo distributions of DZ with the data (see Fig. 15a) for different values of σ_{CH}. The error in our knowledge of the pion momenta is due both to σ_{CH} and to multiple scattering. These two sources contribute in about equal proportions, so that it is fair to say that the error in our knowledge of the pion momentum resolution is 3%

or less. This is also the order of magnitude of the error in the resolution width of $m_{2\pi}$ (the 2π mass determined from the two pion momenta). All this is simply meant to justify the statement that the error in our knowledge of the resolution width of $m = (m_z + m_{2\pi})/2$ is clearly considerably less than 5%. This uncertainty shows up in our results only in the omega terms in the fits. However, since the statistical errors alone are always much larger than 5% of the values of the omega parameters, it is safe to ignore this possible source of error.

The assumed form of the background may contain errors from a number of sources. These include the errors in the production distribution of Banner et al.[27] that were assumed, the neglect of the $\cos\theta_n \sin\theta_n$ term (which is in practice indistinguishable from the $\cos^2\theta_n$ term), and the possibility of some sharp momentum dependence at one of the production vertices. The true shape may also be affected by as much as 10% of the data which is neither N^{*-} nor ρ or ω, and it is very possible that the efficiency of the neutron counters varies with the 2π mass. The primary effect of the uncertainty in the background on our results is on the number of ρ that are found in the fits. For example, if the background were more concave than we think it is, the parameter α_1, which indicates the number of ρ, would be larger than indicated by the fits. This uncertainty in the number of ρ affects our calculations of ρ-ω interference in the determination of the branching ratio at full coherence with $\phi = \pm \frac{\pi}{2}$. The branching ratio

for incoherence and for $\phi = \pi$ are unaffected. As we have already noted, by cutting the data at $M_{\pi-n} = 1300$ MeV, it is possible to remove a much larger fraction of the N^* events than of the ρ events. The 2π mass spectrum for data with $M_{\pi-n} > 1300$ MeV (Fig. 29a) shows a much clearer peak at the ρ mass than the plot of all the data (Fig. 23). Cutting at 1360 MeV (Fig. 29b) reduces the background even more leaving a large ρ peak. Fitting the data cut at 1300 MeV to Eq. (30), we find the number of ρ events to be

$$N_\rho = 2106 \pm 387$$

(for $m_\rho = 765$, $\Gamma_\rho = 125$ MeV). Since the background constitutes a smaller fraction of the data for this fit, any error in the assumed form of the background should have less of an effect, and this value for the number of ρ is a good check of N_ρ for the fit to all the data. According to the Monte Carlo, cutting at 1300 MeV will reduce the number of ρ events by a factor of 0.785 because of the smaller phase space. Correcting for this, we would expect $N_\rho = 2684$ for all the data. This agrees well with the actual value of $N_\rho = 2887 \pm 424$ determined from the fit to all the data. As a further check on the number of ρ we have fit the 2π mass distribution for three ranges of $M_{\pi-n}$. These were fits to Eq. (30) with the ω parameter, α_2, set to zero. In this way, the fit errors in the number of ρ were reduced over those determined from four parameter fits in which correlations between the errors in N_ρ and N_ω increase the uncertainty in N_ρ. The results were as follows:

Region	N_ρ	Fraction of Total Events in Region
$M_{\pi^-n} \leq 1300$ MeV	710±250	20%
$1300 < M_{\pi^-n} \leq 1360$	1205±190	37%
$M_{\pi^-n} < 1360$	1310±170	43%
sum of three regions	3225±357	
all events	3060±356	32%

The increase in the fraction of ρ as one moves away from the N^* region is further evidence that the clear peaking at the ρ mass in the $M_{\pi^-n} < 1360$ MeV 2π mass plot is not spurious. Because of the clear peak in this region one is assured that the fitted determination of $N_\rho = 1310$ is not far off because of a systematic misinterpretation of the background. The above results show that the ρ events extend into the regions closer to N^*.

As an upper limit, it is hard to believe that the value of N_ρ used in the ω-ρ interference calculations is more than 750 events off in either direction. Less than 2100 ρ events would be inconsistent with the number of ρ found in the fits to the mass plot in the two regions away from N^* and with the clear peaks seen at the ρ mass in the plots of data with M_{π^-n} cuts at 1300 and 1360. More than 3650 ρ events would make it hard to explain the large number of events involved in the N^{*-} peak of Fig. 25. To see how an error of 750 events in N_ρ would affect the results, we have computed the branching ratios for complete coherence and $\phi = \pm \frac{\pi}{2}$ just as we did in

the last section with only α_1 changed to correspond to 750 more and less ρ events. Changes of this magnitude in α_1 resulted in changes in the branching ratio of $\pm\ 3.0 \times 10^{-2}$ for $\phi = +\frac{\pi}{2}$ and $^{+0.010}_{-0.006}$ for $\phi = -\frac{\pi}{2}$. These limits on the systematic error due to the background shape are in some sense arbitrary since we do not know all the mechanisms involved in the background. However, they do give a good idea of the range of error from this source that seems to be consistent with the data. The only number that is significantly affected by this error is the branching ratio for $\phi = +\frac{\pi}{2}$ alone.

V. RESULTS AND CONCLUSIONS

Since there is no way of knowing the degree of coherence between ρ and ω in the data and since there is no clear $\omega \to 2\pi$ effect, the best way of reporting the branching ratio,

$$B = \frac{N_{\omega\to 2\pi}}{N_{\omega\to 3\pi}} \frac{\epsilon_{3\pi}}{\epsilon_{2\pi}}$$

and mixing parameter, δ', is to make a series of assumptions of coherence and relative ω-ρ phase angle. The results of this experiment's measurements of B and δ' are listed below. For each number the best value is listed first with the statistical error. This is followed in square brackets by the lower and upper limits of the systematic errors discussed in the last section.

$B = 0.64 \pm 0.86\%$	$[-1.16 \pm 1.03\%$	$1.91 \pm 0.79\%]$	<u>incoherence</u>
$\delta' = 1.62^{+0.85}_{-1.62}$ MeV	$[0.98^{+1.04}_{-0.98}$ MeV	$3.16^{+0.60}_{-0.74}$ MeV$]$	
$B = 12.8 \pm 1.6\%$	$[9.8 \pm 1.6\%$	$15.8 \pm 1.6\%]$	<u>coherence</u>:
$\delta' = 7.24^{+0.45}_{-0.47}$ MeV	$[5.98^{+0.42}_{-0.45}$ MeV	$8.72^{+0.51}_{-0.54}$ MeV$]$	destructive interference $\phi = +\pi/2$
$B = 0.032 \pm 0.084\%$	$[0.0002 \pm 0.0062\%$	$0.25 \pm 0.20\%]$	constructive interference
$\delta' = 0.36^{+0.33}_{-0.36}$ MeV	$[0.15^{+0.26}_{-0.15}$ MeV	$1.14^{+0.38}_{-0.60}$ MeV$]$	$\phi = -\pi/2$
$B = 1.22 \pm 0.88\%$	$[0.26 \pm 1.11\%$	$2.00 \pm 0.79\%]$	
$\delta' = 2.23^{+0.70}_{-1.06}$ MeV	$[0.90^{+1.16}_{-0.90}$ MeV	$3.23^{+0.59}_{-0.72}$ MeV$]$	$\phi = \pi$

Because events near the ω mass in this experiment are limited to a very narrow range of momentum transfer, which is, furthermore, a region in which the ρ and ω production amplitudes are very slowly varying, it is not unlikely that there is a good deal of coherence between ρ and ω. If this is the case, then the results listed above indicate that if the $\omega \to 2\pi$ effect is not of very small size, $\phi \neq -\frac{\pi}{2}$ in this experiment. The results are consistent with either a small effect or no effect for incoherence or if $\phi = \pi$. The χ^2 of the fit improves somewhat for this latter assumption, but not too much should be taken from this improvement in χ^2 because of the possibility of fluctuations.

We have also studied a large sample of $\pi^- p \to \pi^+ \pi^- \pi^0 n$ data including about 7600 $\omega \to \pi^+ \pi^- \pi^0$ events. We have measured the Dalitz plot asymmetry of these events to be

$$A = -0.014 \pm 0.028.$$

A is a measure of C-invariance, and this result is clearly consistent with no C-violation. The Dalitz plot distribution was found to satisfy the simplest $J^P = 1^-$ matrix element very well. No evidence was seen of a rho dominance effect in the matrix element.

ACKNOWLEDGEMENTS

Quite a number of people have helped me in one way or another in preparing this thesis. I am grateful to them all.

Most of all, I thank Prof. Wonyong Lee who as my sponsor has always given me the guidance and help I needed without ever taking over this first attempt at independent research.

The other members of the experimental group, who were all involved in the design, construction and running of this experiment were Emile Hyman, Michael Gormley, John Peoples, Claude Schultz and Stephen Stein.

I would like to thank Chang-li Yiu and William Cooper for very valuable discussions that helped to clarify my thinking particularly about the theoretical aspects of the experiment.

The whole Nevis Staff contributes to each Nevis thesis. I am particularly thankful to the following who, at one time or another, went above and beyond the call of duty to help me out: Edward Barnes, Christina Nobile, Vincent Savino, and especially, Ann Therrien whose typing was only one of her contributions to the completion of this thesis.

Most of the drawings were made by Norman Jensen and Robert Leins. Jim Cleary did the photography.

Finally, I would like to thank my parents and Madeleine for their patience.

APPENDIX I

Relating the 2π Mass Distribution to the ω-ρ Mixing Parameters

We start with the propagator equation for the $\pi\pi n$ reaction amplitude, Ψ, Eq. (3):

$$\Psi = \underset{\sim}{T} \frac{1}{(m\underset{\sim}{1})^2 - \underset{\sim}{M}^2} \underset{\sim}{A} = \underset{\sim}{T}\,\underset{\sim}{P}\,\underset{\sim}{A} \quad .$$

If we assume that

$$\delta^2 << M_\omega^{\ 2} \quad \text{and} \quad \delta^2 << M_\rho^{\ 2}$$

then we can determine the inverse of

$$\underset{\sim}{P}^{-1} = \begin{pmatrix} m^2 - (M_\rho^{\ 2} + \delta^2) & \delta(M_\omega + M_\rho) \\ \delta(M_\omega + M_\rho) & m^2 - (M_\omega^{\ 2} + \delta^2) \end{pmatrix}$$

The result is the propagator of Eq. (3):

$$\underset{\sim}{P} = \frac{1}{(m^2 - M_\omega^{\ 2})(m^2 - M_\rho^{\ 2})} \begin{pmatrix} m^2 - M_\omega^{\ 2} & \delta(M_\omega + M_\rho) \\ \delta(M_\omega + M_\rho) & m^2 - M_\rho^{\ 2} \end{pmatrix} \tag{AI.1}$$

Using Eq. (A.1), we may now write out Eq. (3) for Ψ:

$$\begin{aligned} \Psi &= A_\rho P_{11} T_\rho + A_\omega P_{21} T_\rho + A_\rho P_{21} T_\omega + A_\omega P_{22} T_\omega \\ &= \frac{A_\rho T_\rho}{(m^2 - M_\rho^{\ 2})} + (A_\omega T_\rho + A_\rho T_\omega) \frac{(M_\omega + M_\rho)\delta}{(m^2 - M_\rho^{\ 2})(m^2 - M_\omega^{\ 2})} + \frac{A_\omega T_\omega}{(m^2 - M_\omega^{\ 2})} \end{aligned}$$

Squaring, we get

$$\begin{aligned} |\Psi|^2 &= \frac{|A_\rho|^2 |T_\rho|^2}{|m^2 - M_\rho^{\ 2}|^2} + \left| \frac{(A_\omega T_\rho + A_\rho T_\omega)(M_\omega + M_\rho)\delta}{(m^2 - M_\rho^{\ 2})} + A_\omega T_\omega \right|^2 \frac{1}{|m^2 - M_\omega^{\ 2}|^2} \\ &\quad + 2\mathrm{Re}\left[\frac{A_\rho^{\ *} T_\rho^{\ *}}{(m^2 - M_\rho^{\ 2})^*} \left(\frac{(A_\omega T_\rho + A_\rho T_\omega)(M_\omega + M_\rho)\delta}{(m^2 - M_\rho^{\ 2})} + A_\omega T_\omega \right) \frac{1}{(m^2 - M_\omega^{\ 2})} \right] \\ &= \frac{|A_\rho|^2 |T_\rho|^2}{|m^2 - M_\rho^{\ 2}|^2} + \frac{|a_\omega|^2 |T_\rho|^2}{|m^2 - M_\omega^{\ 2}|^2} + 2\mathrm{Re}\left[\frac{A_\rho^{\ *} a_\omega |T_\rho|^2}{(m^2 - M_\omega^{\ 2})(m^2 - M_\rho^{\ 2})^*} \right] \end{aligned} \tag{4}$$

where

$$a_\omega = \frac{(A_\omega+\beta A_\rho)(M_\omega+M_\rho)\delta}{m^2-M_\rho^2} + \beta A_\omega$$

$$\simeq A_\omega \frac{(m_\omega+m_\rho)}{(m^2-M_\rho^2)} \left[\delta(1+\beta A_\rho/A_\omega)+\beta(m_\omega-m_\rho+i\frac{\Gamma_\rho}{2})\right] , \qquad (4a)$$

and

$$\beta = T_\omega/T_\rho .$$

This is Eq. (4) of Sec. I. In Eq. (4a) we have calculated the numerator of the second term at $m = m_\omega$ for clarity, and ignored the widths in $(M_\omega+M_\rho)$.

Combining $|\Psi|^2$ of Eq. (4) with the efficiency and phase space functions of mass gives the 2π mass distribution of Eq. (6). For the $3\pi n$ final state events we have a similar equation, Eq. (8). Integrating over the various terms of these two equations relates the ρ and ω amplitudes to the number of ρ and ω observed in the 2π and 3π spectra. For example, integration over the ω term of Eq. (8) determines the number of $\omega\to3\pi$ in the data for a given value of A_ω:

$$N_{\omega\to3\pi} = n\int|A_\omega|^2 m_\omega\Gamma_{\omega\to3\pi} \frac{\phi(m)\,\epsilon_{3\pi}(m)\,dm^2}{(m^2-m_\omega^2)^2+m_\omega^2\Gamma_\omega^2}$$

$$\simeq n|A_\omega|^2 m_\omega\Gamma_{\omega\to3\pi}\epsilon_{3\pi}(m_\omega)\int \frac{\phi(m)\,dm^2}{(m^2-m_\omega^2)^2+m_\omega^2\Gamma_\omega^2}$$

$$= |A_\omega|^2 m_\omega\Gamma_{\omega\to3\pi}\epsilon_{3\pi}(m_\omega) I_{\omega 3\pi} \qquad (AI.2)$$

where

$$I_{\omega 3\pi} = n\int\frac{\phi(m)\,dm^2}{(m^2-m_\omega^2)^2+m_\omega^2\Gamma_\omega^2} .$$

(Where useful, we can pull slowly varying functions of m like $\epsilon_{3\pi(m)}$ out of the integral since the ω Breit Wigner is so sharply peaked.) Similarly, integrating over the ω term of

Eq. (6) gives the number of $\omega\to 2\pi$ (<u>not including any interference effects</u>) in terms of $\tilde{a}_\omega = a_\omega(m^2-M_p^2)$:

$$N_{\omega\to 2\pi} = n|\tilde{a}_\omega|^2 \int \frac{m_\rho \Gamma_\rho}{(m^2-m_\rho^2)^2+m_\rho^2\Gamma_\rho^2} \frac{1}{(m^2-m_\omega^2)^2+m_\omega^2\Gamma_\omega^2} \phi(m)\epsilon_{2\pi}(m)\,dm^2 \tag{AI.3}$$

$$= |\tilde{a}_\omega|^2 \; I_{OMEGA}$$

The integral $I_{OMEGA} = 7.186 \times 10^{-10}$ and the efficiencies $\epsilon_{2\pi}(m_\omega)$ and $\epsilon_{3\pi}(m_\omega)$ were computed using the Monte Carlo technique described in Sec. IV.B. The integral $I_{\omega 3\pi}$, used for $\omega\to 3\pi$, can be related easily to I_{OMEGA} since

$$I_{OMEGA} \simeq \frac{m_\rho \Gamma_\rho(m_\omega)\epsilon_{2\pi}(m_\omega)}{(m_\omega^2-m_\rho^2)^2+m_\rho^2\Gamma_\rho^2} \; I_\omega = 8.778 \times 10^{-6} \; \epsilon_{2\pi}(m_\omega) I_\omega \; .$$

By integrating the first term of Eq. (6), we have

$$|A_\rho|^2 = N_{\rho\to 2\pi}/I_{RHO} \tag{AI.4}$$

where $N_{\rho\to 2\pi}$ is the number of ρ observed in the data and

$$I_{RHO} = \int BW_\rho^2 \epsilon_{2\pi}(m)\phi(m)\,dm^2 = 0.5607$$

was also determined using a Monte Carlo calculation.

Using Eqs. (4a'), (AI.2) and (AI.3), we have enough information to determine the mixing parameter δ' from the experimental results for $N_{\omega\to 2\pi}$ and $N_{\omega\to 3\pi}$:

$$|\tilde{a}_\omega|^2 = |A_\omega|^2 (m_\omega+m_\rho)^2 \delta'^2$$

$$= 3.405 \times 10^6 \frac{\epsilon_{2\pi}(m_\omega)}{\epsilon_{3\pi}(m_\omega)} N_{\omega\to 3\pi}\delta'^2$$

$$= N_{\omega\to 2\pi}/I_{OMEGA} \; .$$

Thus in terms of the branching ratio, B,

$$|\delta'| = 20.2\left(\frac{\epsilon_{3\pi}(m_\omega)}{\epsilon_{2\pi}(m_\omega)} \frac{N_{\omega\to 2\pi}}{N_{\omega\to 3\pi}}\right)^{1/2}$$

$$= 20.2 \; B^{1/2} \text{ MeV.}$$

APPENDIX II

Decay Angular Distribution of N^{*-} in $\pi^- p \to \pi^+\pi^- n$

We define the z axis to be the direction of the beam in the lab or center of mass. In the <u>rest frame</u> of the $\pi^- n$ system, the neutron has orbital angular momentum $L_n = 1$ since N^* has $J^P = 3/2^+$ and decays into a $\pi^-(J^P = 0^-)$ and neutron $(J^P = 1/2^+)$. The state $L_n = 2$ is forbidden, assuming parity conservation in the strong decay of N^*. We may decompose the N^* wave function $\Psi_{3/2,m}$ into the neutron spin function, $\chi_{+1/2}$, and the orbital angular momentum spherical harmonics, $Y_{Lm_L}(\theta_n,\phi_n)$, as follows:

$$\Psi_{3/2} = Y_{11}\chi_{1/2} = \frac{1}{\sqrt{4\pi}}(-\sqrt{\tfrac{3}{2}}\,\sin\theta_n e^{i\phi_n})\chi_{1/2}$$

$$\Psi_{1/2} = \sqrt{\tfrac{1}{3}}\,Y_{11}\chi_{-1/2} + \sqrt{\tfrac{2}{3}}\,Y_{10}\chi_{1/2} = \frac{1}{\sqrt{4\pi}}(\sqrt{2}\,\cos\theta_n\chi_{1/2} - \sqrt{\tfrac{1}{2}}\,\sin\theta_n e^{i\phi_n}\chi_{-1/2})$$

$$\Psi_{-1/2} = \sqrt{\tfrac{2}{3}}\,Y_{10}\chi_{-1/2} + \sqrt{\tfrac{1}{3}}\,Y_{1-1}\chi_{1/2} = \frac{1}{\sqrt{4\pi}}(\sqrt{2}\,\cos\theta_n\chi_{-1/2} + \sqrt{\tfrac{1}{2}}\sin\theta_n e^{i\phi_n}\chi_{1/2})$$

$$\Psi_{-3/2} = Y_{1-1}\chi_{-1/2} = \frac{1}{\sqrt{4\pi}}(\sqrt{\tfrac{3}{2}}\,\sin\theta_n e^{-i\phi_n})\chi_{-1/2}\,. \qquad \text{(AII.1)}$$

For clarity, we have written only the subscript m on $\Psi_m = \Psi_{3/2,m}$.

The general spin state of a spin 3/2 particle is completely defined by four complex amplitudes, $c_m \cdot |c_m|^2$ is the probability of measuring the spin of the particle to be m, and the only restriction is that $\sum_m |c_m|^2 = 1$. The angular distribution of the state characterized by the set of c_m is

$$f(\theta_n,\phi_n) = (\sum_m c_m\Psi_m)(\sum_{m'} c_{m'}\Psi_{m'})^\dagger$$

$$= \alpha_1\cos^2\theta_n + \alpha_2\sin^2\theta_n(1+\alpha_3\cos 2\phi_n + \alpha_4\sin 2\phi_n) + \alpha_5\cos\theta_n\sin\theta_n$$

$$(\cos\phi_n + \alpha_6\sin\phi_n)$$

where the α_i are related to the various products of the c_m.

If we average $f(\theta_n,\phi_n)$ over the azimuthal angle ϕ_n, taking into account the efficiency of the experimental apparatus, we have

$$f(\theta_n) = A\sin^2\theta_n + B\cos^2\theta_n + C\cos\theta_n\sin\theta_n$$
$$= A(1+a\cos^2\theta_n + b\cos\theta_n\sin\theta_n) \quad . \qquad \text{(AII.2)}$$

Included in A and C are the experimental averages over $\cos\phi_n$ and $\sin\phi_n$. Clearly, if the experimental efficiency were independent of ϕ_n, these averages would be zero and C would be zero. But this is not the case in this experiment so that we must, in general, include the $\cos\theta_n\sin\theta_n$ term.

More may be learned about this distribution by looking in the center of mass. In this frame, the total angular momentum, J, is made up of the center of mass orbital angular momentum of the π^-n system, L, and the spin of that system, S. S is, of course, the same spin that defines the total angular momentum of the π^-n system at rest that we dealt with first. If we look at the <u>incoming</u> π^-p system in the center of mass, it is clear that there can be no z component of orbital angular momentum since both particles move in the z direction. As a result $J_z = \pm 1/2$; all the angular momentum in the z direction comes from the proton spin. By conservation of angular momentum, $J_z = \pm 1/2$ in the $\pi^+\pi^-n$ <u>final</u> state, though J may take any half integral value. N^* production has been analyzed in terms of partial waves of specific J and L, and it is well known that a number of partial waves contribute.[27] For each partial wave, we may predict the <u>decay</u> angular dependence (in the π^-n rest frame), of the wave function $F^{\pm}_{LJ}(\theta_n,\phi_n)$, for

$J_z = \pm 1/2$. This is done by first finding the Clebsch-Gordan decomposition into the different states of m,

$$|JJ_z\rangle = \sum_m |LL_z Sm\rangle\langle LL_z Sm|JJ_z\rangle$$

and then writing $F^{\pm}_{LJ}$ in terms of the Clebsch-Gordan coefficients and the Ψ_m of Eqs. (AII.1):

$$F_{LJ}^{\pm}(\theta_n,\phi_n) = \sum_m \langle LL_z 3/2m|J\pm 1/2\rangle \Psi_m(\theta_n,\phi_n) \ .$$

Then if the relative (complex) weights, X_{LJ}, of the partial waves are known, we may determine the angular distribution

$$f(\theta_n,\phi_n) = \frac{1}{2}\sum_{J_z=\pm 1/2} [\sum_{LJ} X_{LJ} F_{LJ}^{\pm}(\theta_n,\phi_n)][\sum_{L'J'} X_{L'J'} F_{L'J'}^{\pm}(\theta_n,\phi_n)]^{\dagger} \quad \text{(AII.3)}$$

In Eq. (AII.3), we assumed the protons of the target are unpolarized. Listed below are a number of $F^{\pm}_{LJ}$ for low order partial waves:

L_J	$\sqrt{4\pi}\ F^{\pm}_{LJ}(\theta,\ \phi)$
$P_{1/2}$	$\chi_{\pm}[\pm\sin\theta(-\sqrt{\frac{3}{4}}\ e^{\pm i\phi}+\sqrt{\frac{1}{12}}\ e^{\mp i\phi})-\sqrt{\frac{2}{3}}\ \cos\theta]+\chi_{\mp}[\pm\sqrt{\frac{1}{6}}\ \sin\theta e^{\pm i\phi}+\sqrt{\frac{1}{3}}\ \cos\theta]$
$D_{1/2}$	$\chi_{\pm}[\sin\theta(\sqrt{\frac{3}{20}}\ e^{\pm i\phi}-\sqrt{\frac{3}{20}}\ e^{\mp i\phi})\pm\sqrt{\frac{2}{5}}\ \cos\theta]+\chi_{\mp}[\sin\theta(-\sqrt{\frac{1}{10}}\ e^{\pm i\phi}$ $+\sqrt{\frac{3}{5}}\ e^{\mp i\phi})\mp\sqrt{\frac{3}{5}}\ \cos\theta]$
$S_{3/2}$	$\chi_{\pm}[\sqrt{2}\ \cos\theta]\qquad +\chi_{\mp}[\mp\sqrt{1/2}\ \sin\theta e^{\pm i\phi}]$
$P_{3/2}$	$\chi_{\pm}[-\sin\theta(\sqrt{\frac{3}{5}}\ e^{\pm i\phi}+\sqrt{\frac{4}{15}}\ e^{\mp i\phi})\pm\sqrt{\frac{2}{15}}\ \cos\theta]+\chi_{\mp}[-\sqrt{\frac{1}{30}}\ \sin\theta e^{\pm i\phi}\mp\sqrt{\frac{16}{15}}\cos\theta]$
$D_{3/2}$	$\chi_{\pm}[\mp\sin\theta(\sqrt{\frac{3}{5}}\ e^{\pm i\phi})\quad -\sqrt{\frac{2}{5}}\ \cos\theta]+\chi_{\mp}[\pm\sin\theta(\sqrt{\frac{1}{10}}e^{\pm i\phi}+\sqrt{\frac{3}{5}}\ e^{\mp i\phi})]$

N^* produced in states of various combinations of partial waves will decay, in general, according to non-uniform angular distributions. For some combinations of relative weights, X_{LJ}, these distributions may have heavy $\cos^2\theta$ dependence as the data appears to have. For example, a pure S-wave N^* will decay

according to

$$f(\theta_n, \phi_n) = \frac{1}{8\pi} (1+3 \cos^2\theta_n).$$

REFERENCES

1 S.L. Glashow, Phys. Rev. Letters 7, 469 (1961).

2 B.C. Maglic, L.W. Alvarez, A.H. Rosenfeld, M.L. Stevenson, Phys. Rev. Letters 7, 178 (1961).

3 The G parity operator is defined $G = C\, e^{i\pi I_y}$, where C is charge conjugation and I_y is the y component of isotopic spin. See T.D. Lee, C.N. Yang, Nuovo Cimento 3, 749 (1956).

4 Y. Nambu, J.J. Sakurai, Phys. Rev. Letters 8, 79 (1962).

5 G. Feinberg, Phys. Rev. Letters 8, 151 (1962).

6 G. Lütjens, J. Steinberger, Phys. Rev. Letters 12, 517 (1964).

7 S.M. Flatte, D.O. Huwe, J.J. Murray, J.B. Shafer, F.T. Solmitz, M.L. Stevenson, C.G. Wohl, Phys. Rev. 145, 1050 (1966).

8 S.M. Flatte, UCRL Report 18687, 1969, unpublished.

9 Chang-li Yiu has provided a theoretical proof of Eq. (3) making a minimum of assumptions (private communication).

10 J. Bernstein, G. Feinberg, Nuovo Cimento 25, 1343 (1962).

11 The K_1-K_2 problem was treated earlier by T.D. Lee, R. Oehme, C.N. Yang in Phys. Rev. 106, 340 (1957). Still earlier V.F. Weisskopf, E.P. Wigner developed the technique for atomic states in Z. Physik 63, 54 (1930); 65, 18 (1930).

12 M. Gourdin, L. Stodolsky, F.M. Renard, Phys. Letters 30B, 347 (1969).

13 J.D. Jackson, Nuovo Cimento 34, 1644 (1964).

14 A.S. Goldhaber, G.C. Fox, C. Quigg, Phys. Letters 30B, 249 (1969).

15 R.G. Sachs, J.F. Willemson, EFINS 69-102 (unpublished).

[16] G. Goldhaber, W.R. Butler, D.G. Coyne, B.H. Hall, J.N. MacNaughton, G.H. Trilling, Phys. Rev. Letters 23, 1351 (1969).

[17] J.E. Augustin, J.C. Bizot, J. Buon, J. Haissinski, D. Lalanne, P.C. Marin, J. Perez-y-Jorba, F. Rumpf, E. Silva, S. Tavernier, Nuovo Cimento 2, 2141 (1969).

[18] Stephen Stein, Nevis Report 177, Columbia University Ph.D. Thesis (1969), unpublished.

[19] The only changes were the following: a) The field in the spectrometer magnet was increased to 6.9 kG; b) The π^- beam was tuned to 1245 MeV/c; c) The "Mode 1" trigger (see Ref. 18) was not used for neutral decays as in the η experiment.

[20] This probe was calibrated against an NMR probe by Roland Bernhagen.

[21] S.A. Schelkunoff, Applied Mathematics for Engineers and Scientists (Van Nostrand, Princeton, N.J. 1965 2nd Ed.), p. 31.

[22] J.D. Jackson, Classical Electrodynamics (John Wiley & Sons, New York, 1962), p. 458.

[23] H.A. Bethe, Ann. Physik 5, 325 (1930); F. Bloch, Z. Physik 81, 363 (1933); M.S. Livingston, H.A. Bethe, Rev. Mod. Phys. 9, 285 (1937); R.M. Sternheimer, Phys. Rev. 103, 511 (1956).

[24] C. Zemach, Phys. Rev. 133B, 1201 (1964).

[25] M. Gell-Mann, D. Sharp, W. Wagner, Phys. Rev. Letters 8, 261 (1962).

[26] C.G. Howard, C.N. Vittitoe, Phys. Rev. 162, 1323 (1967); D. Huwe, E. Marquit, F. Oppenheimer, W. Schultz, J.R. Wilson, Phys. Letters 24B, 252 (1967); J. Kirz, J. Schwartz, R.D. Tripp, Phys. Rev. 130, 2481 (1963).

[27] M. Banner, J.F. Detoeuf, M.L. Fayoux, J.L. Hamel, J. Zsembery, Phys. Rev. 166, 1346 (1968).

[28] See, for example, S. Gasiorowicz, Elementary Particle Physics, (John Wiley & Sons, New York, 1966), p. 295.

[29] J.P. Merlo, G. Valladas, Proc. Roy. Soc. (London) A289, 489 (1966).

[30] Particle Data Group, "Particle Properties Tables", UCRL-8030, Revised January, 1969.

TABLE I

DT and TP cuts for the Nine Chambers

Chamber Quadrant	TPLO < TP < TPHI TPLO	 TPHI	$\lvert DT-DT_o \rvert$ < DTCUT DT_o	 DTCUT
1 inner	118	145	-4500	52000
middle	127	158	20000	134000
outer	146	178	25000	120600 + 744 r*
2 inner	124	148	0	75000
middle	121	157	-8000	110000
outer	117	156	0	235000
3 inner	117	149	-6000	55800 + 178 r*
middle	100	151	1000	116000
outer	130	162	0	195000

* r is distance from chamber center - see text.

TABLE II

3π Data: Background Subtraction for 28 Dalitz Plot Regions

Dalitz Plot Region (see Fig. 16)	Total 3π Events N	ω Events N_ω (σ=0.836 nsec)	N_ω/N	ω Events (σ=0.855 nsec)
1	502	145.1±41	0.29	146.8±41
2	543	275.0±41	0.51	279.1±39
3	389	237.0±39	0.61	240.6±36
4	388	235.8±38	0.61	239.4±36
5	380	233.2±38	0.61	237.3±35
6	348	190.3±37	0.55	193.8±35
7	376	245.6±38	0.65	249.5±36
8	423	138.0±38	0.33	140.1±37
9	789	377.0±44	0.48	382.8±43
10	612	325.2±41	0.53	330.2±40
11	598	324.8±41	0.54	329.6±39
12	620	317.5±41	0.51	322.9±40
13	628	373.6±42	0.59	379.6±40
14	671	426.1±43	0.63	432.1±40
Left Side of D.P.	7267	3844.2±150	0.314	3903.8±144
15	488	90.4±42	0.19	91.8±42
16	932	405.1±49	0.43	410.2±48
17	718	366.7±43	0.51	372.3±41
18	697	387.7±43	0.56	393.5±41
19	705	349.7±43	0.50	354.4±42
20	638	313.8±42	0.49	319.1±41
21	804	431.9±45	0.54	438.2±43
22	669	71.9±46	0.11	73.3±46
23	635	216.9±44	0.34	220.0±43
24	452	221.6±39	0.49	225.0±37
25	405	223.2±38	0.55	227.2±36
26	392	222.7±39	0.57	226.5±36
27	370	197.1±38	0.53	200.2±35
28	411	238.6±36	0.58	242.7±36
Right Side of D.P.	8316	3737.3±156	0.449	3794.4±152
Whole Dalitz Plot	15583	7581.5±217	0.486	7698.2±209

TABLE III

Monte Carlo Results: Chamber Efficiency for $\omega \to 2\pi$ and $\omega \to 3\pi$ vs ω Spin Alignment

ω Spin Alignment α	Chamber Efficiency ($\times 10^{-2}$) $\epsilon_{2\pi}$	$\epsilon_{3\pi}$	$\frac{\epsilon_{3\pi}}{\epsilon_{2\pi}}$
0	4.350±0.02	2.816±0.013	0.6474±0.004
0.1	4.197	2.750	0.6552
0.2	4.020	2.673	0.6649
0.3	3.815	2.584	0.6773
0.4	3.571	2.478	0.6939
0.5	3.280	2.351	0.7170
0.6	2.924	2.197	0.7513
0.7	2.478	2.003	0.8080
0.8	1.907	1.753	0.9196
0.9	1.145	1.421	1.2410
1.0	0.0798	0.955	11.962

TABLE IV

Table of Mass Spectrum Distribution

Dist.	Description	Function	Integral over Mass Spectrum
BW_ρ^2	ρ Breit Wigner $m_\rho = 760$ MeV $\Gamma_{\rho o}=120$ MeV	$\frac{m_\rho \Gamma_\rho}{(m^2-m_\rho^2)^2+m_\rho^2\Gamma_\rho^2}$ where $\Gamma_\rho=\Gamma_{\rho o}(\frac{q}{q_o})^3 \frac{m}{m_\rho}$ and q=momentum of π in 2π rest frame.	$I_{RHO}= 0.5606$
$BW_\rho^2\lvert F_\omega\rvert^2$	ω Breit Wigner Mixing Term $m_\omega=783.4$ MeV $\Gamma_\omega=12.2$ MeV	$BW_\rho^2 \frac{1}{(m^2-m_\omega^2)^2+m_\omega^2\Gamma_\omega^2}$	$I_{OMEGA}= 7.18\text{x}10^{-10}$
$BW_\rho^2 ReF_\omega$	Real part of ω Breit Wigner Amplitude	$BW_\rho^2\lvert F_\omega\rvert^2(m^2-m_\omega^2+\frac{1}{4}\Gamma_\omega^2)$	$I_{REOM}=-4.13\text{x}10^{-6}$
BG_{flat}	N^{*-} Background Isotropic Decay Term	$\frac{(m_{N^*}\Gamma_{N^*})^2 F(\theta_c)}{(M_{\pi-n}^2-m_{N^*}^2)^2+(M_{N^*}\Gamma_{N^*})^2}$ $F(\theta_c)$ is production angle distribution fit to Legendre Polynomials of Banner et al[27]	$I_{BG_{flat}}=2.937\text{x}10^4$
$BG_{\cos^2}$	$\cos^2\theta_n$ Decay Term	$BG_{flat}\cos^2\theta_n$ $\cos\theta_n=(\hat{P}_n)_z$ in π^- rest frame	$I_{BG_{\cos^2}}=7.446\text{x}10^3$
$BG_{\cos\sin}$	$\cos\theta_n\sin\theta_n$ Decay Term	$BG_{flat}\cos\theta_n\sin\theta_n$	$I_{BG_{\cos\sin}}=$ $1.1439\text{x}10^4$

TABLE V

Study of Systematic Errors Due to ρ Parameters

m_ρ MeV	Γ_ρ MeV	Branching Ratio ($\times 10^{-2}$) incoh.	$\phi=+\pi/2$	$\phi=-\pi/2$	$\phi=\pi$	Mixing Parameter - δ' (MeV) incoh.	$\phi=+\pi/2$	$\phi=-\pi/2$	$\phi=\pi$
755	105	1.53 ±.81	11.6 ±1.5	0.201 ±.200	1.73 ±.82	2.51 +.60 -.80	6.93 +.43 -.46	0.91 +.37 -.85	2.66 +.57 -.73
755	125	1.71 ±.80	13.0 ±1.6	0.225 ±.197	1.87 ±.80	2.83 +.60 -.76	7.80 +.46 -.49	1.02 +.38 -.66	2.95 +.58 -.72
755	145	1.91 ±.79	14.6 ±1.7	0.250 ±.195	2.00 ±.79	3.16 +.60 -.74	8.72 +.51 -.54	1.14 +.38 -.60	3.23 +.59 -.72
765	105	0.27 ±.89	11.4 ±1.5	0.007 ±.042	0.96 ±.93	0.98 +1.04 -.98	6.34 +.41 -.44	0.15 +.26 -.15	1.84 +.74 -1.49
765	125	0.64 ±.86	12.8 ±1.6	0.032 ±.084	1.22 ±.88	1.62 +.85 -1.62	7.24 +.45 -.47	0.36 +.33 -.36	2.23 +.70 -1.06
765	145	0.97 ±.83	14.2 ±1.7	0.067 ±.111	1.43 ±.85	2.13 +.77 -1.32	8.14 +.48 -.51	0.56 +.35 -.56	2.58 +.68 -.93
775	105	-1.16* ±1.03	11.6 ±1.7	0.115 ±.212	0.26 ±1.11	*	5.98 +.42 -.45	0.60 +.41 -.60	0.90 +1.16 -.90
775	125	-0.55* ±0.96	13.1 ±1.7	0.023 ±.082	0.59 ±1.02	*	6.92 +.44 -.47	0.29 +.33 -.29	1.47 +.96 -1.47
775	145	-0.05* ±.91	14.4 ±1.8	0.0002 ±.0062	0.87 ±.95	*	7.81 +.48 -.51	0.027 +.14 -.27	1.92 +.80 -1.92

* A negative branching ratio for the incoherent case indicates a small negative effect near the ω mass.

FIGURE CAPTIONS

Fig. 1 Beam transport system.

Fig. 2 Location of spark chambers in magnet. Left: looking upstream. Right: looking downstream.

Fig. 3 Overall view of experiment.

Fig. 4 Photograph of spark chambers.

Fig. 5 Schematic layout of a typical spark chamber

Fig. 6 Corrected time of flight spectrum for events corresponding to the reaction $\pi^- p \rightarrow \pi^+ \pi^- \pi^o n$.

Fig. 7 Schematic drawing of experiment showing distances involved in time of flight correction and neutron momentum reconstruction.

Fig. 8 T_p and DT distributions for the inner chamber of quadrant 1.

Fig. 9 Histograms of DZ for 3 different regions of θ and $p\beta$.

Fig. 10 Histograms of vertex separation: a) s_x; b) s_y; c) and d) s_z for different ranges of $\cos\theta$ for $2\pi n$ final state events.

Fig. 11 Schematic drawing of liquid hydrogen target and enclosure showing obstructions and limits on V_z.

Fig. 12 Histogram of M_y^2, missing mass squared of y in $\pi^- p \rightarrow \pi^+ \pi^- y$, for events that went into quadrants 1, 3.

Fig. 13 Histograms of M_x^2, missing mass squared of x in $\pi^- p \rightarrow \pi^+ \pi^- xn$. Above: preliminary $3\pi n$ final state events. Below: preliminary $2\pi n$ final state events.

Fig. 14 Histograms of $\Delta E = E_{beam} + E_{target} - E_n - E_{\pi^+} - E_{\pi^-}$. Above: preliminary $3\pi n$ events. Below: preliminary $2\pi n$ events.

Fig. 15 Comparisons of Monte Carlo predictions of resolution

functions with $2\pi n$ data. Monte Carlo functions are drawn as solid curves, data as histograms.
a) DZ; b) ΔE; c) Δm^2. $\sigma_{CH} = 0.037$ cm. $\sigma_{TOF} = 0.78$ nsec.

Fig. 16 $\omega \to \pi^+\pi^-\pi^o$ Dalitz plot showing 28 regions used for matrix element analysis and background subtraction.

Fig. 17 Corrected time of flight histograms for 3π events in a) Region 1; b) Region 4; c) Region 7; d) Region 9.

Fig. 18 Matrix element of $\omega \to 3\pi$ data (background corrected) vs q^2.

Fig. 19 Search for ρ dominance in matrix element of background corrected $\omega \to 3\pi$ data. Plots of matrix element/q^2 (see text) vs a) $m_{\pi^+\pi^o}$, b) $m_{\pi^-\pi^o}$, c) $m_{\pi^+\pi^-}$.

Fig. 20 Production and decay state vectors for measurement of ω polarization. Above: lab frame. Below: center of mass of pions.

Fig. 21 Background corrected distribution of q_z^{lab} for $\omega \to 3\pi$ events. Solid curve is best fit to Monte Carlo distributions with $0 \le \alpha \le 1$.

Fig. 22 Histogram of 2π mass for $\pi\pi n$ data. Solid curve is pure phase space including experimental efficiency.

Fig. 23 Data/Monte Carlo vs m. Best fits to Eqs. (30) and (33) are shown as solid curves.

Fig. 24 Histogram of momentum transfer for $\pi\pi n$ events.

Fig. 25 Histograms of a) M_{π^-n} and b) M_{π^+n} for $\pi\pi n$ events. Curves show Monte Carlo predictions for pure phase space and N^{*-} production at $M_{\pi^-n} = 1236$ (Γ=120) including efficiency.

Fig. 26 Efficiency corrected data vs $\cos\theta_c = \hat{\underset{\sim}{P}}_{\pi-n} \cdot \hat{\underset{\sim}{P}}_{inc}$. Points with error bars are data from this experiment. Solid curve shows Legendre polynomial fit by Banner et al to data taken at $P_{inc} = 1000$ MeV/c.

Fig. 27 Monte Carlo generated functions vs 2π mass for various dynamical assumptions defined in Table IV.

Fig. 28 Dalitz plot of $M_{\pi-n}{}^2$ vs m^2 (in units of $M_{N^*}{}^2 = 1236^2 \text{MeV}^2$ and $m_\omega{}^2 = 783.4^2 \text{MeV}^2$, respectively) for efficiency corrected $\pi\pi n$ data.

Fig. 29 Data/Monte Carlo vs m with N^* cuts. a) $M_{\pi-n} > 1300$ MeV; b) $M_{\pi-n} > 1360$ MeV.

Fig. 30 Data corrected for efficiency vs 2π rest frame decay angle θ for 4 regions of m.

Fig. 31 Data/Monte Carlo vs m for 4 regions of 2π rest frame decay angle θ.

Fig. 32 Phase space plot of m vs momentum transfer for $\pi\pi n$ data.

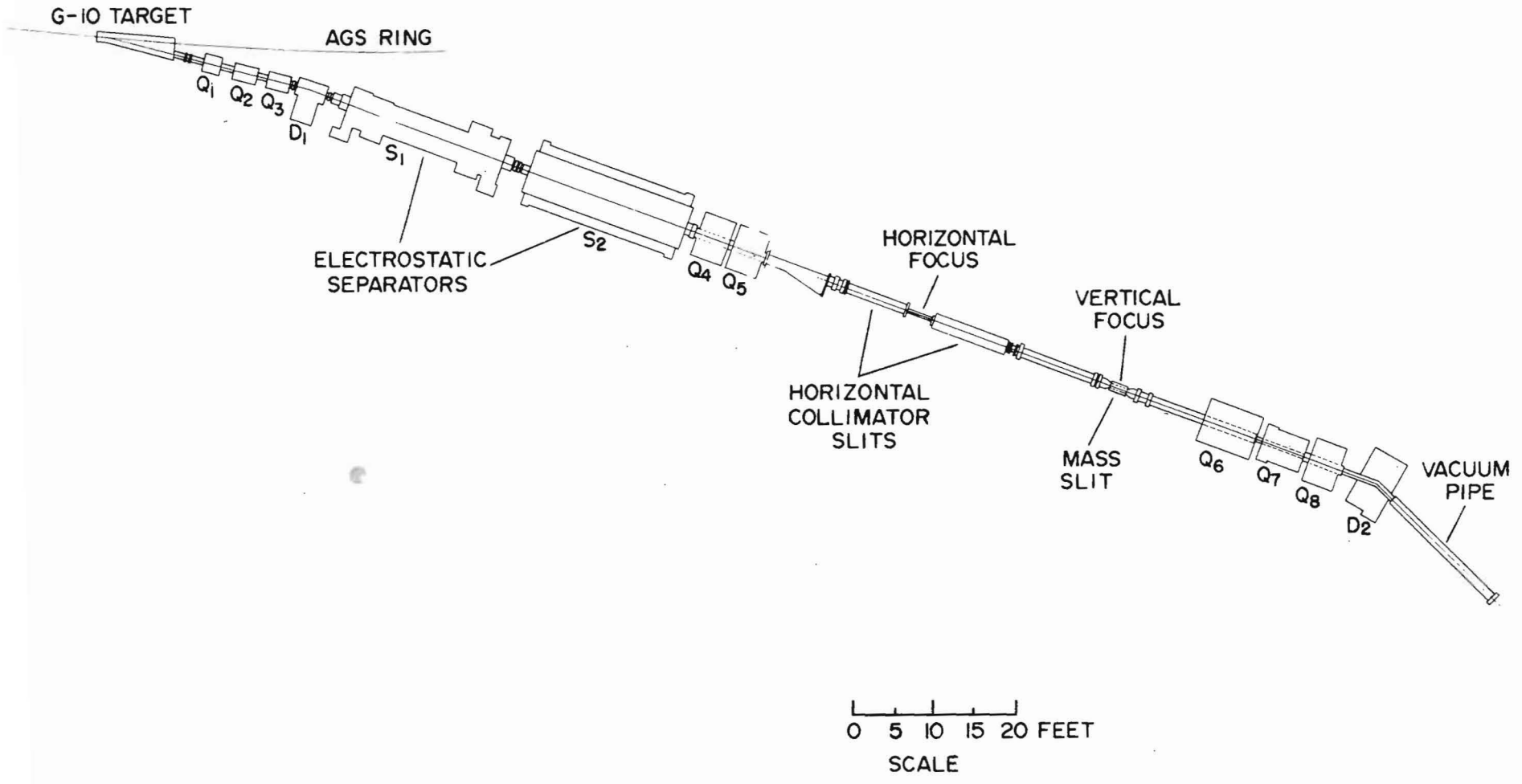
G-10 TARGET
AGS RING
Q1
Q2
Q3
D1
S1
ELECTROSTATIC SEPARATORS
S2
Q4
Q5
HORIZONTAL FOCUS
VERTICAL FOCUS
HORIZONTAL COLLIMATOR SLITS
MASS SLIT
Q6
Q7
Q8
D2
VACUUM PIPE
0 5 10 15 20 FEET
SCALE

Fig. 1

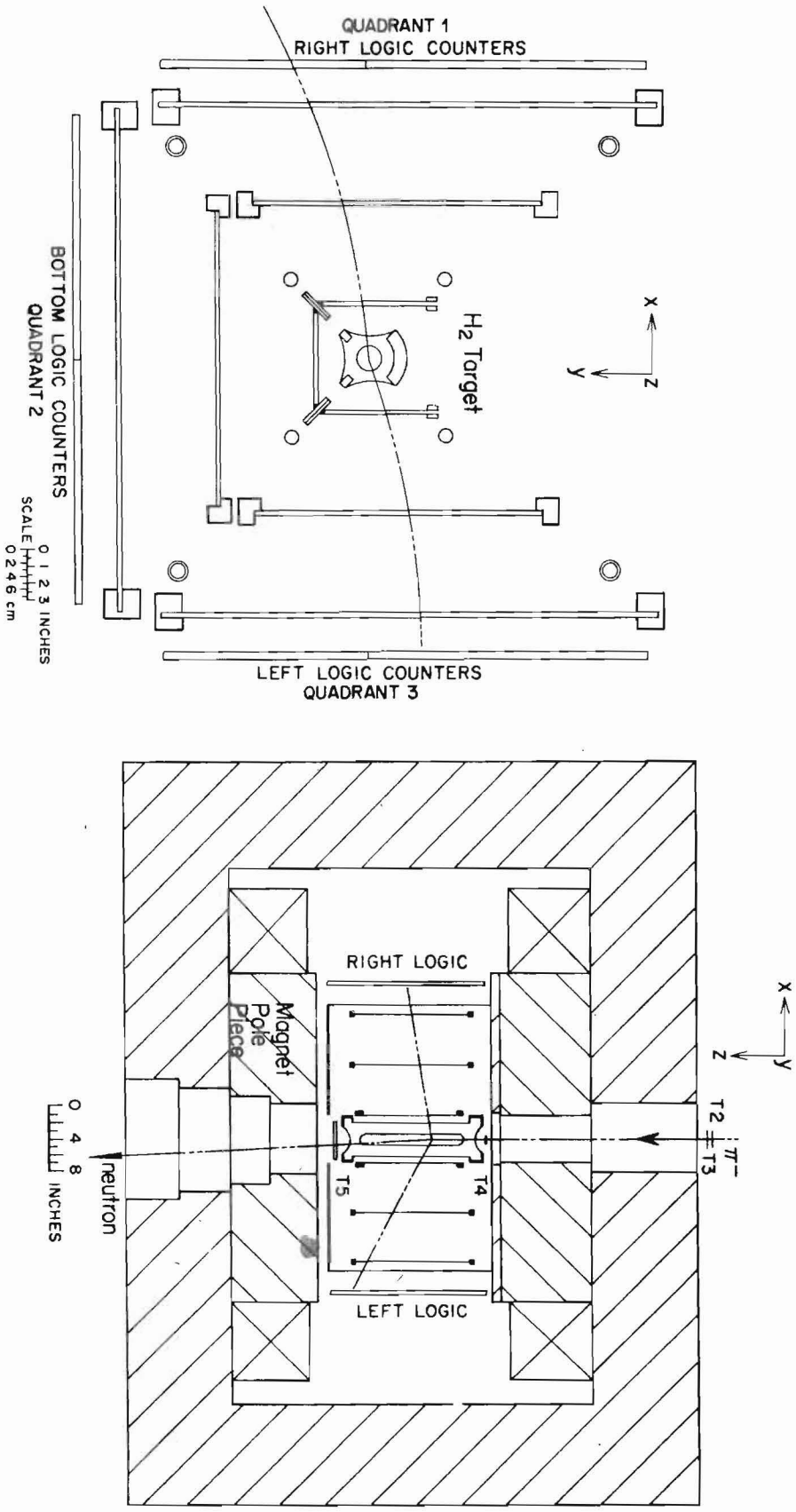
QUADRANT 1
RIGHT LOGIC COUNTERS
BOTTOM LOGIC COUNTERS
QUADRANT 2
SCALE
0 1 2 3 INCHES
0 2 4 6 cm
H_2 Target
x
y
z
LEFT LOGIC COUNTERS
QUADRANT 3
RIGHT LOGIC
Magnet Pole Piece
LEFT LOGIC
T2
T3
T4
T5
π^-
neutron
0 4 8
INCHES
x
y
z

Fig. 2

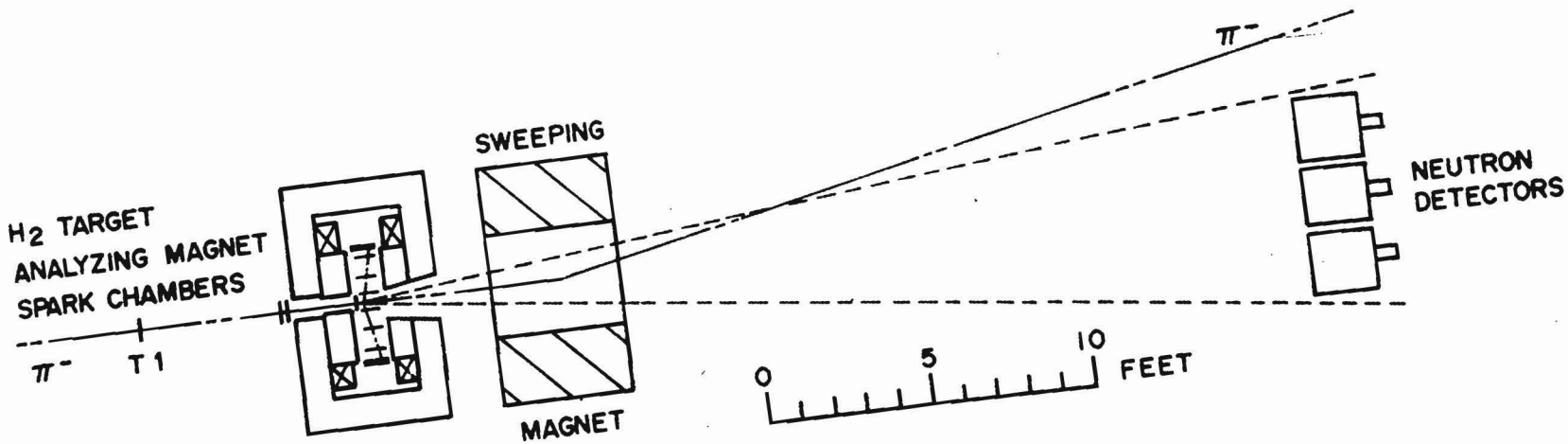
H2 TARGET
ANALYZING MAGNET
SPARK CHAMBERS
π-
T1
SWEEPING
MAGNET
π-
NEUTRON
DETECTORS
0
5
10
FEET

Fig. 3

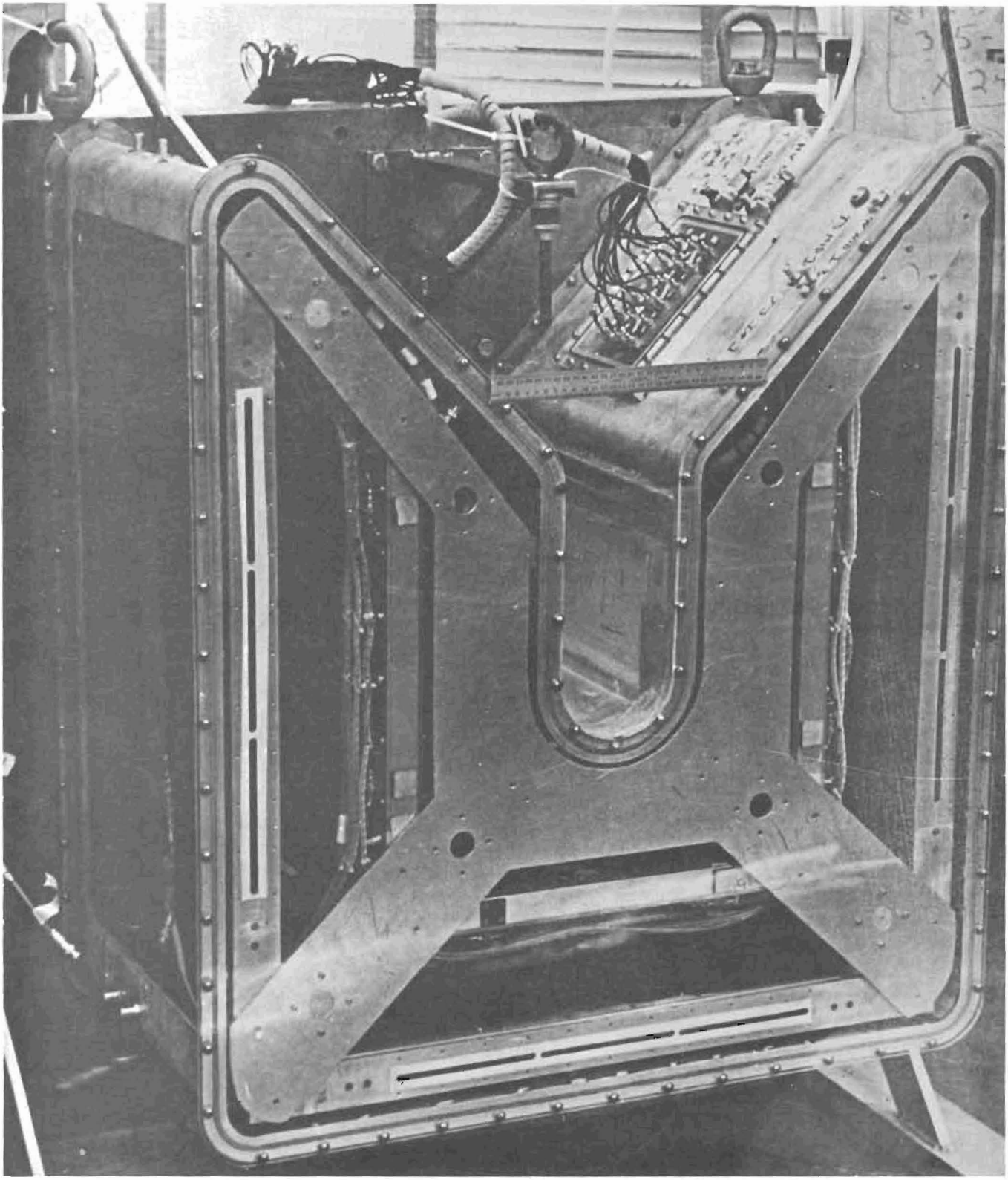

Fig. 4

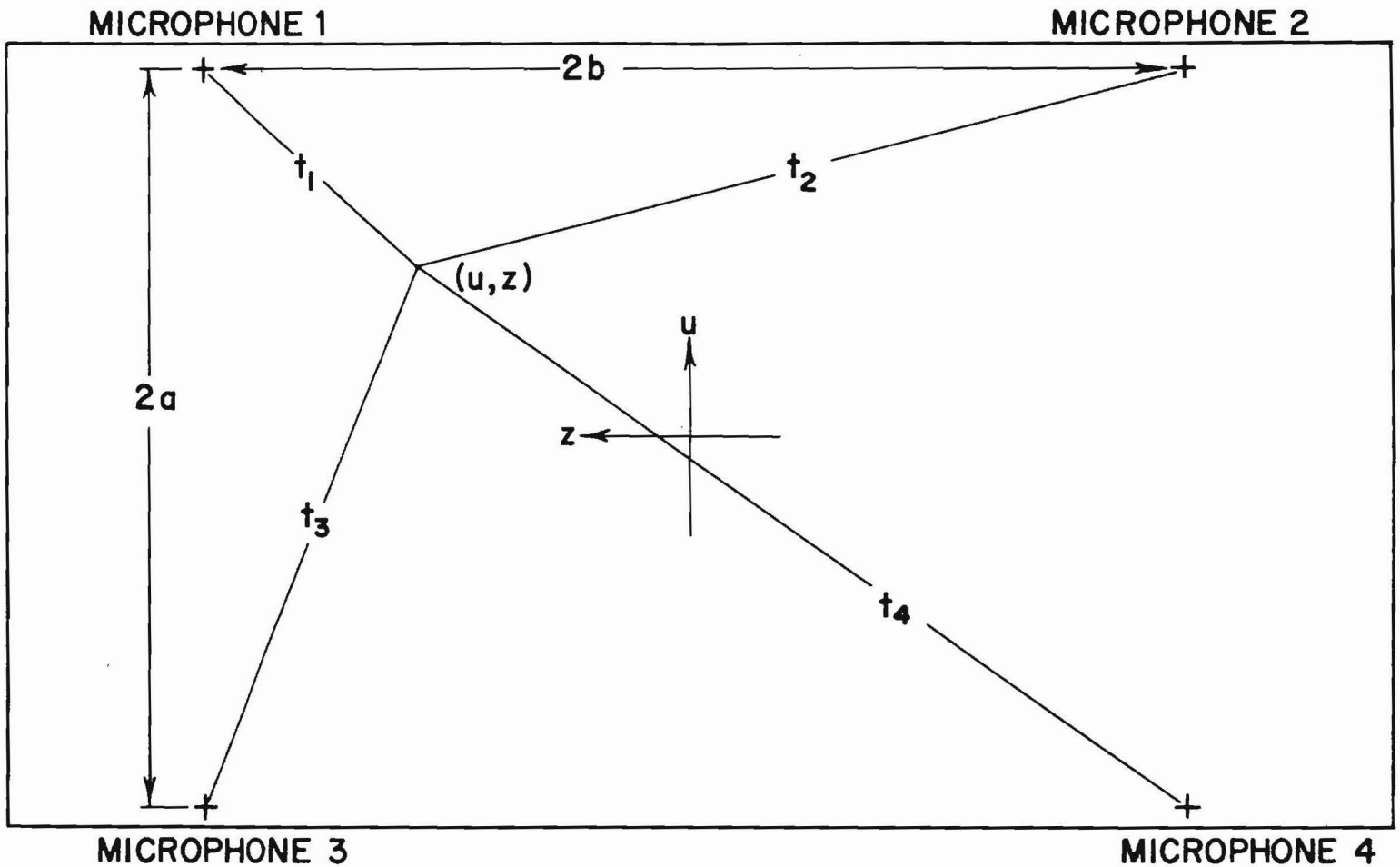
MICROPHONE 1
MICROPHONE 2
2b
t_1
t_2
(u,z)
u
z
2a
t_3
t_4
MICROPHONE 3
MICROPHONE 4

Fig. 5

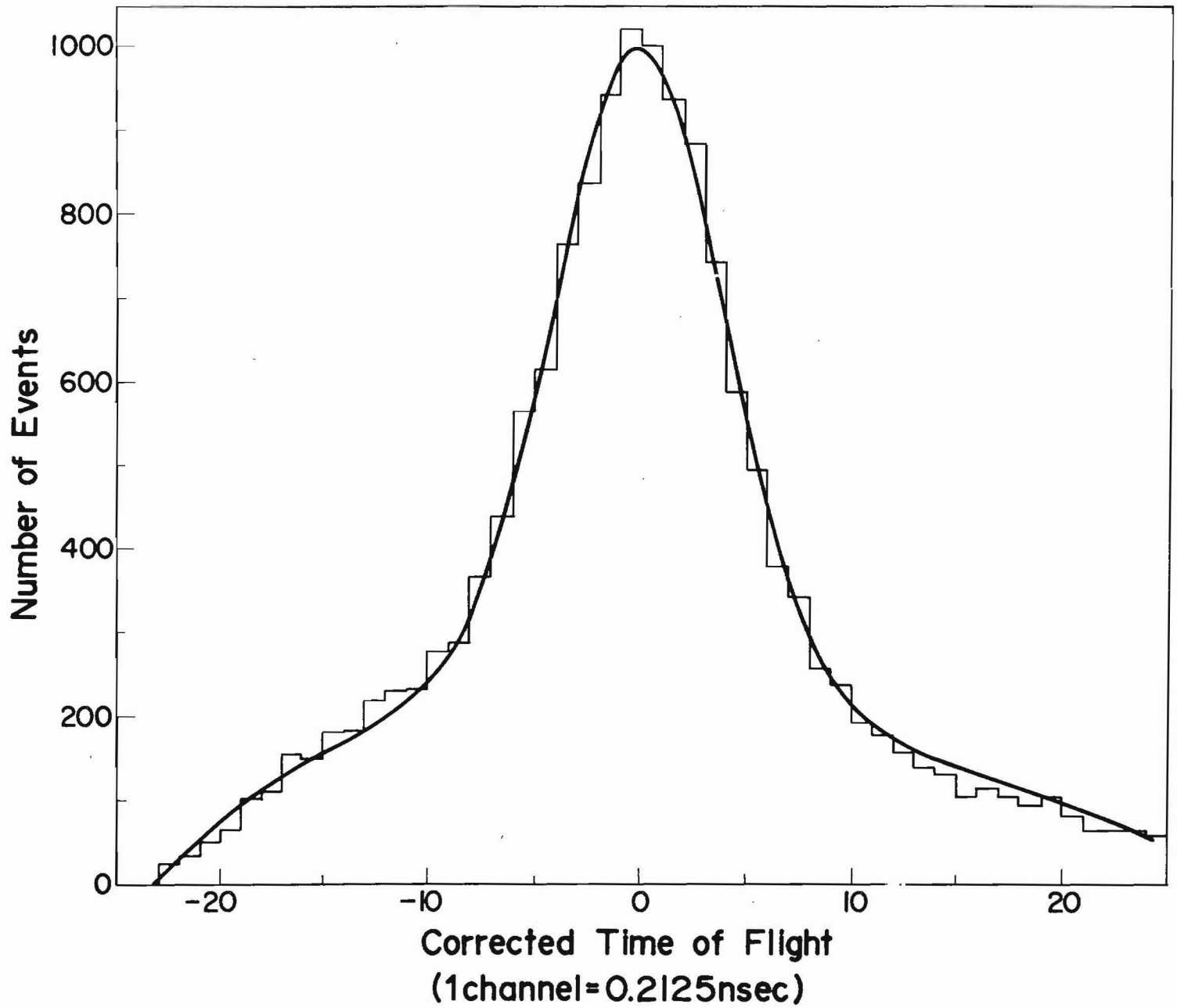
1000
800
600
400
200
0
Number of Events
-20
-10
0
10
20
Corrected Time of Flight
(1channel=0.2125nsec)

Fig. 6

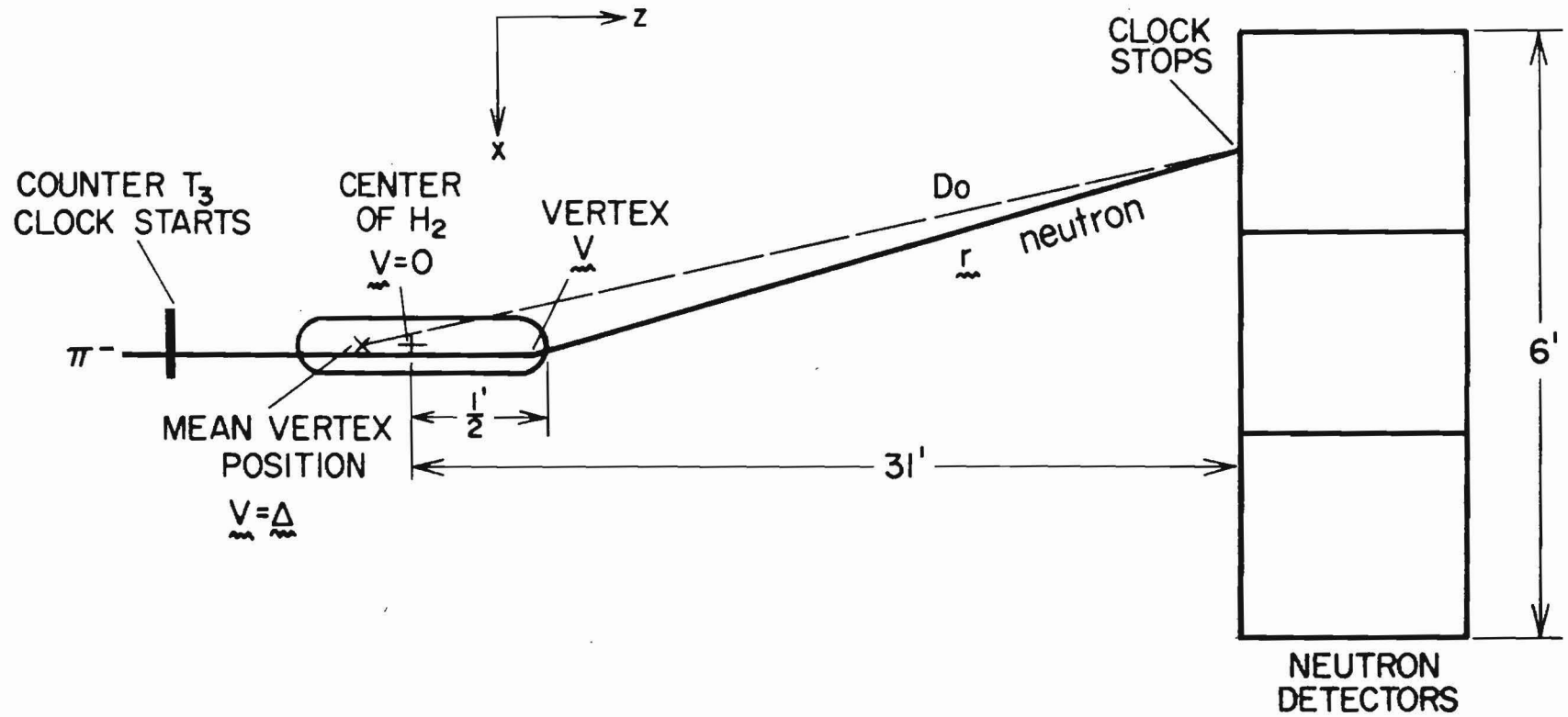
z
x
COUNTER T_3
CLOCK STARTS
CENTER
OF H_2
V=0
VERTEX
V
Do
r
neutron
CLOCK
STOPS
π^-
MEAN VERTEX
POSITION
V=Δ
1'/2
31'
6'
NEUTRON
DETECTORS

Fig. 7

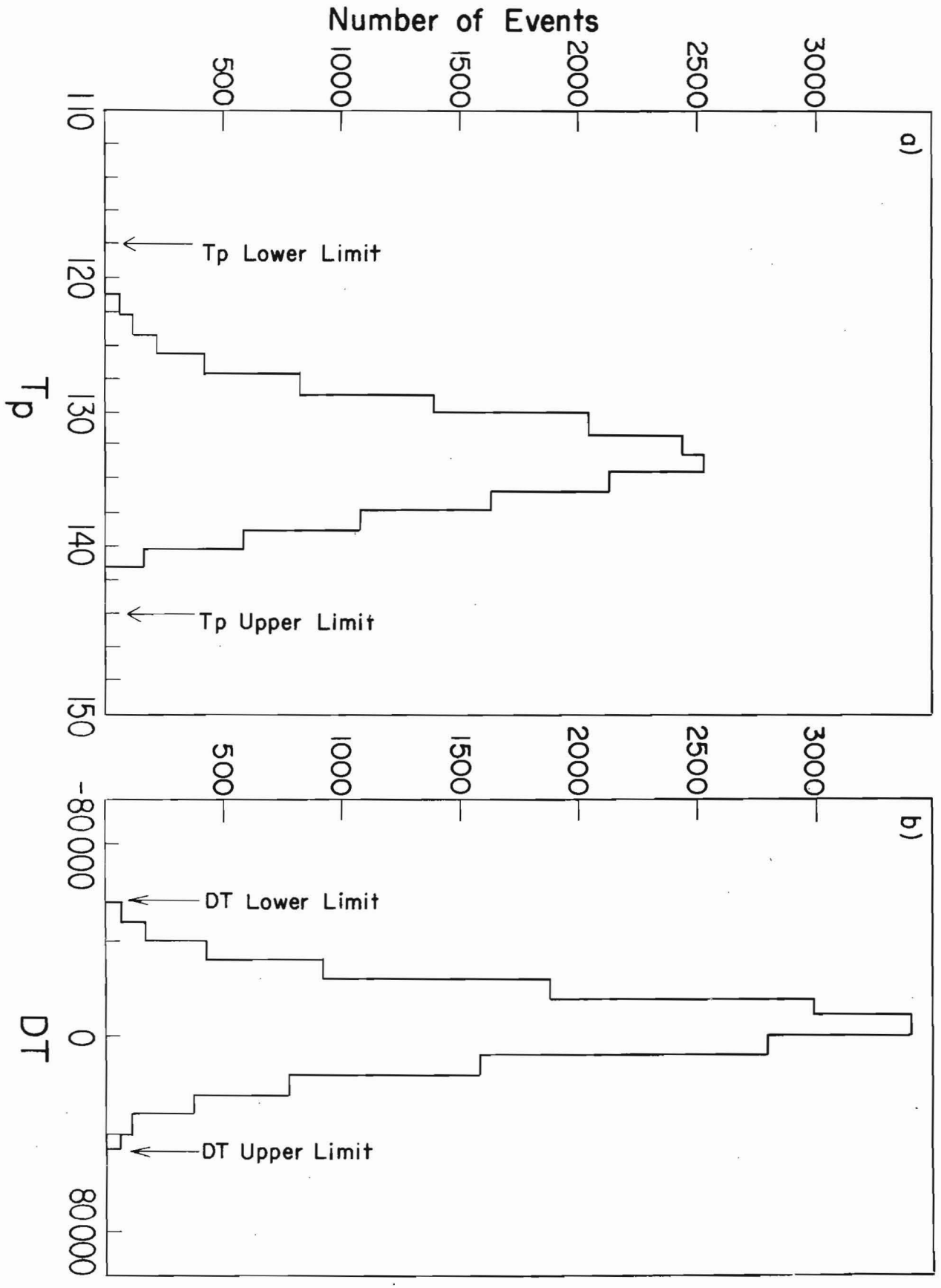
Number of Events
500
1000
1500
2000
2500
3000
a)
Tp Lower Limit
Tp Upper Limit
110
120
130
140
150
Tp
b)
DT Lower Limit
DT Upper Limit
-80000
0
80000
DT

Fig. 8

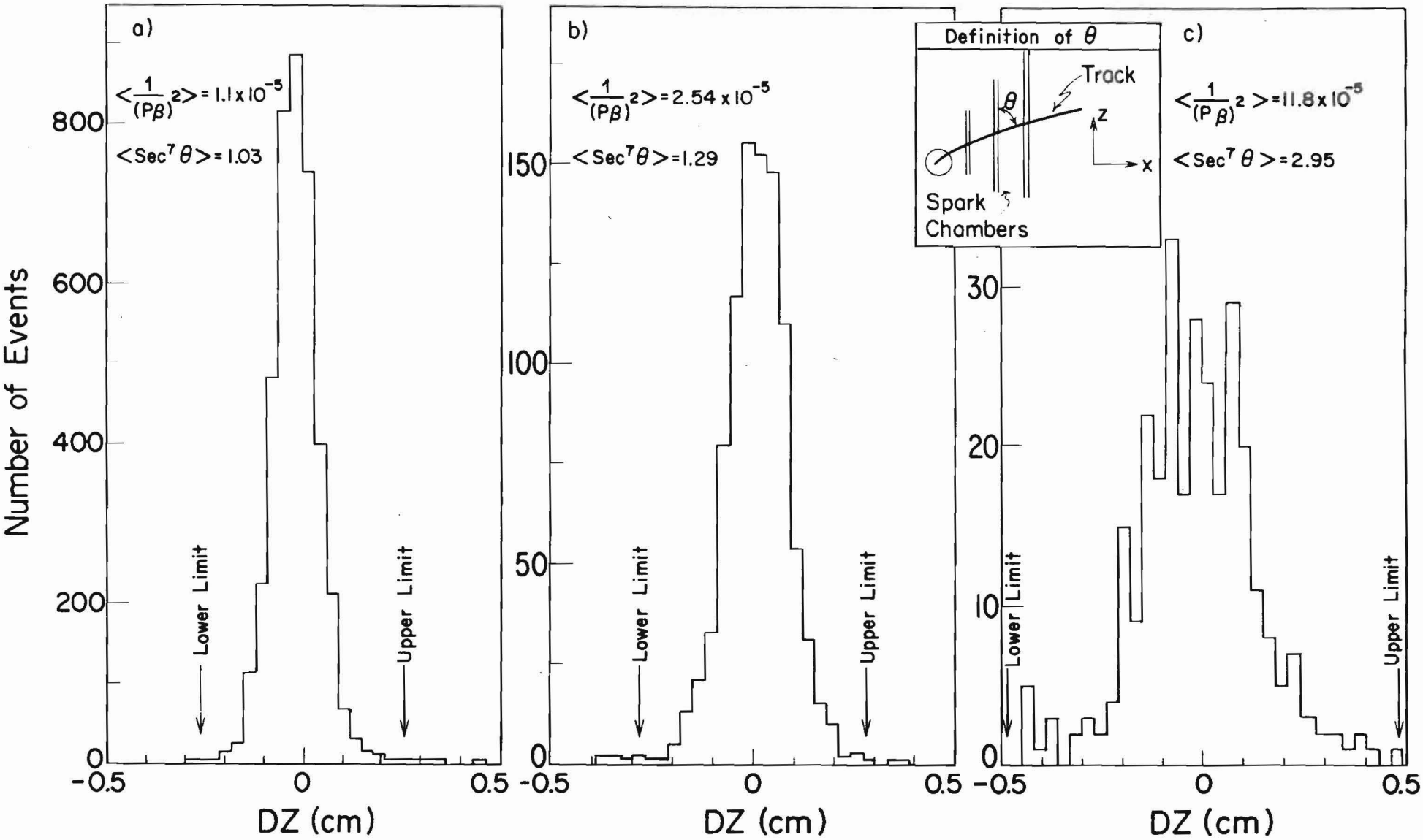
a)
$\langle \frac{1}{(P\beta)^2} \rangle = 1.1 \times 10^{-5}$
$\langle \mathrm{Sec}^7\theta \rangle = 1.03$
b)
$\langle \frac{1}{(P\beta)^2} \rangle = 2.54 \times 10^{-5}$
$\langle \mathrm{Sec}^7\theta \rangle = 1.29$
c)
$\langle \frac{1}{(P\beta)^2} \rangle = 11.8 \times 10^{-5}$
$\langle \mathrm{Sec}^7\theta \rangle = 2.95$
Definition of θ
Track
θ
Z
X
Spark Chambers
Number of Events
Lower Limit
Upper Limit
DZ (cm)
-0.5
0
0.5
0
200
400
600
800
50
100
150
10
20
30

Fig. 9

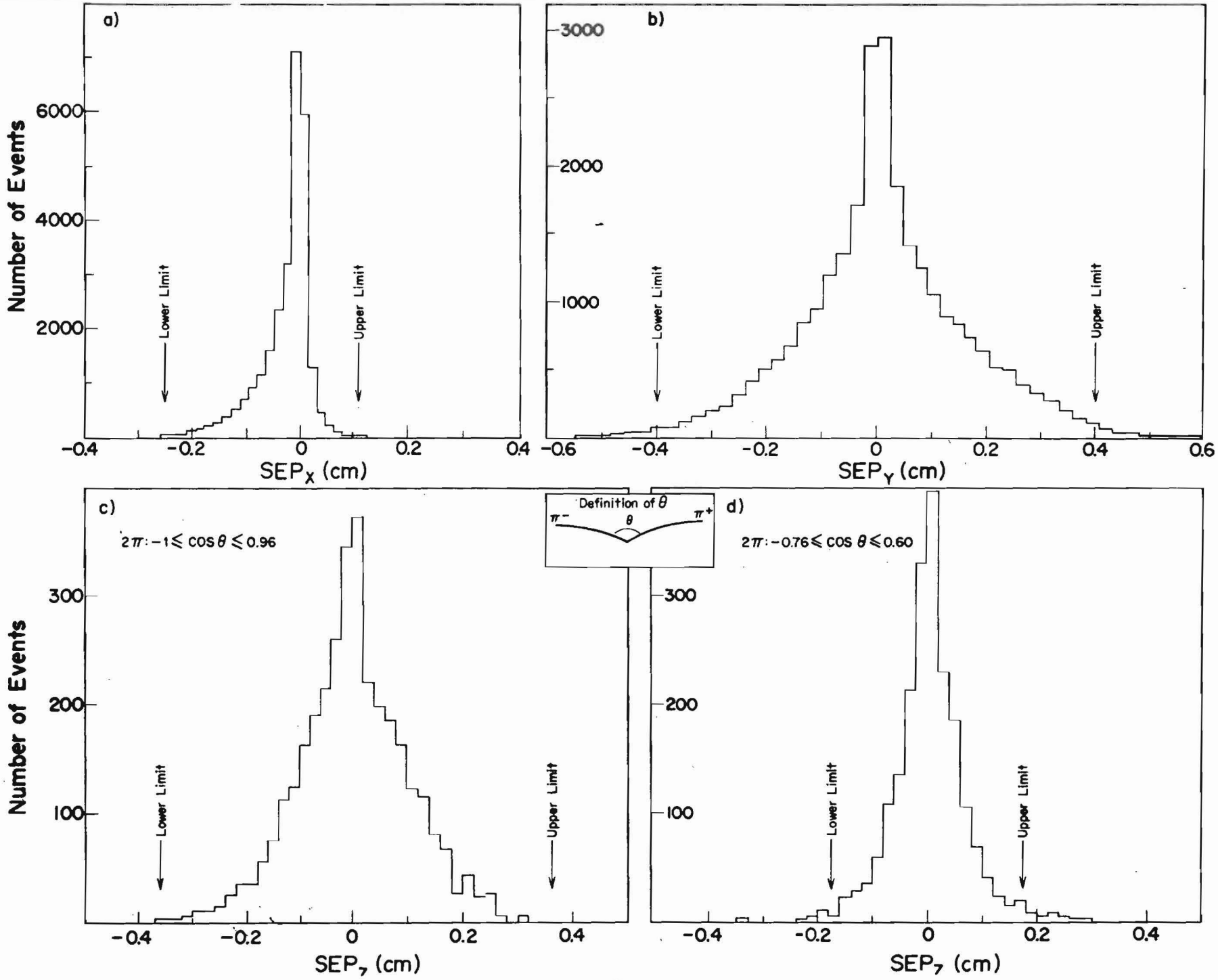
a)
b)
c)
d)
Number of Events
Lower Limit
Upper Limit
SEP$_X$ (cm)
SEP$_Y$ (cm)
SEP$_Z$ (cm)
2π: $-1 \leq \cos\theta \leq 0.96$
2π: $-0.76 \leq \cos\theta \leq 0.60$
Definition of θ
π^-
θ
π^+

F 10

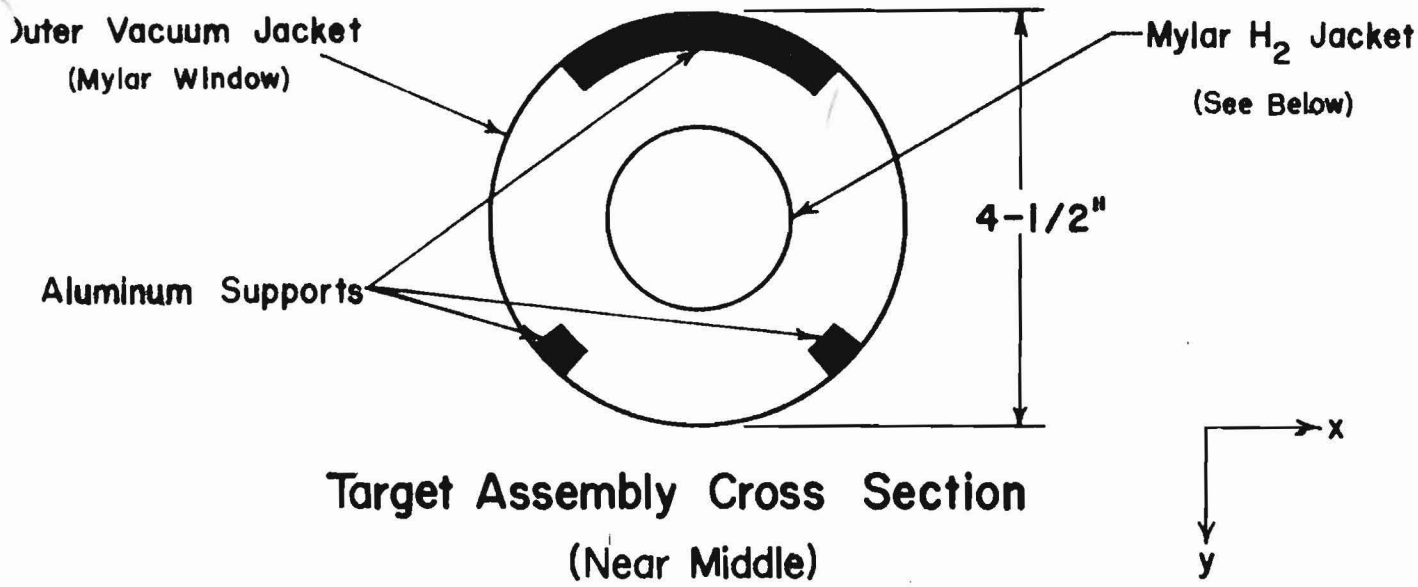

Target Assembly Cross Section
(Near Middle)

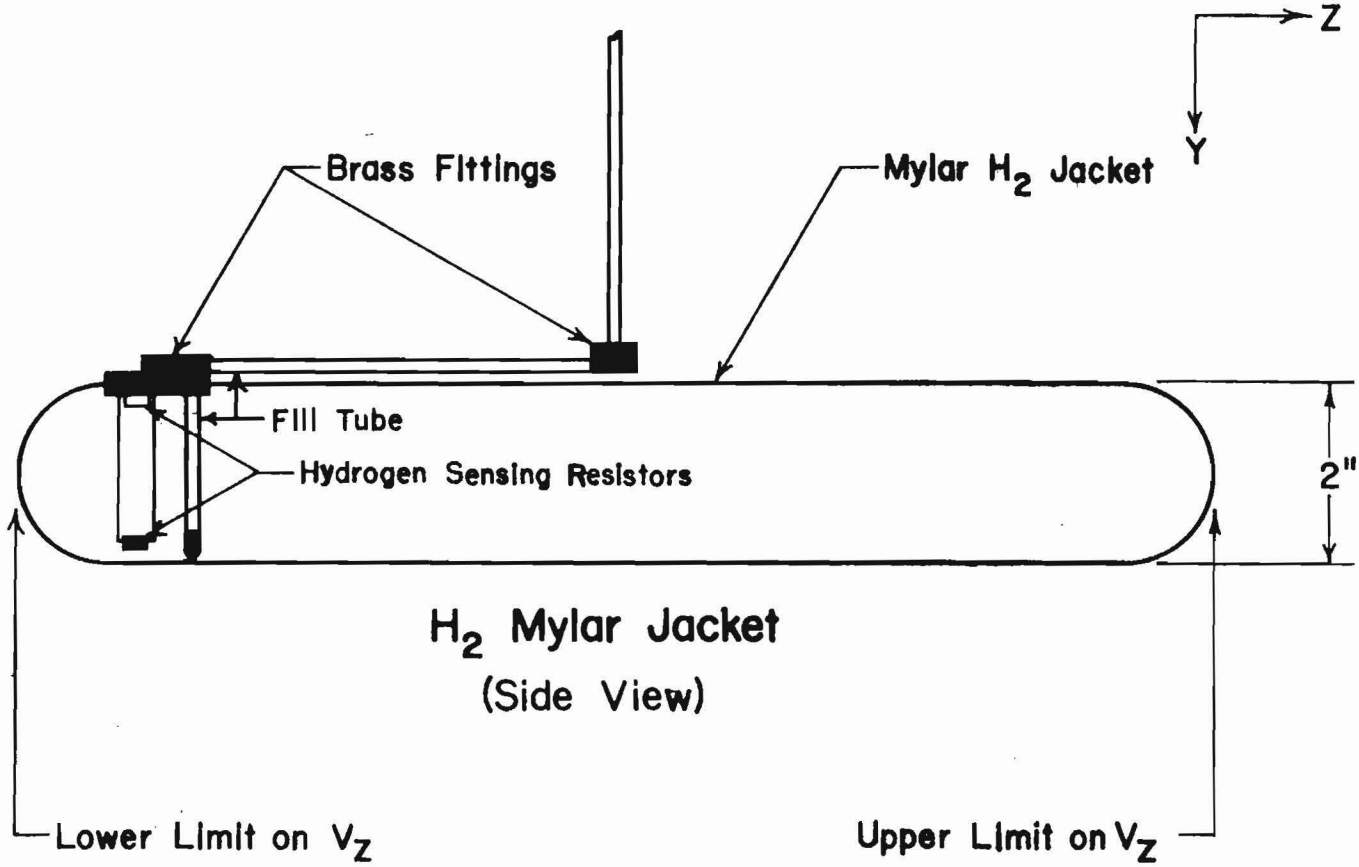

H_2 Mylar Jacket
(Side View)

Fig. 11

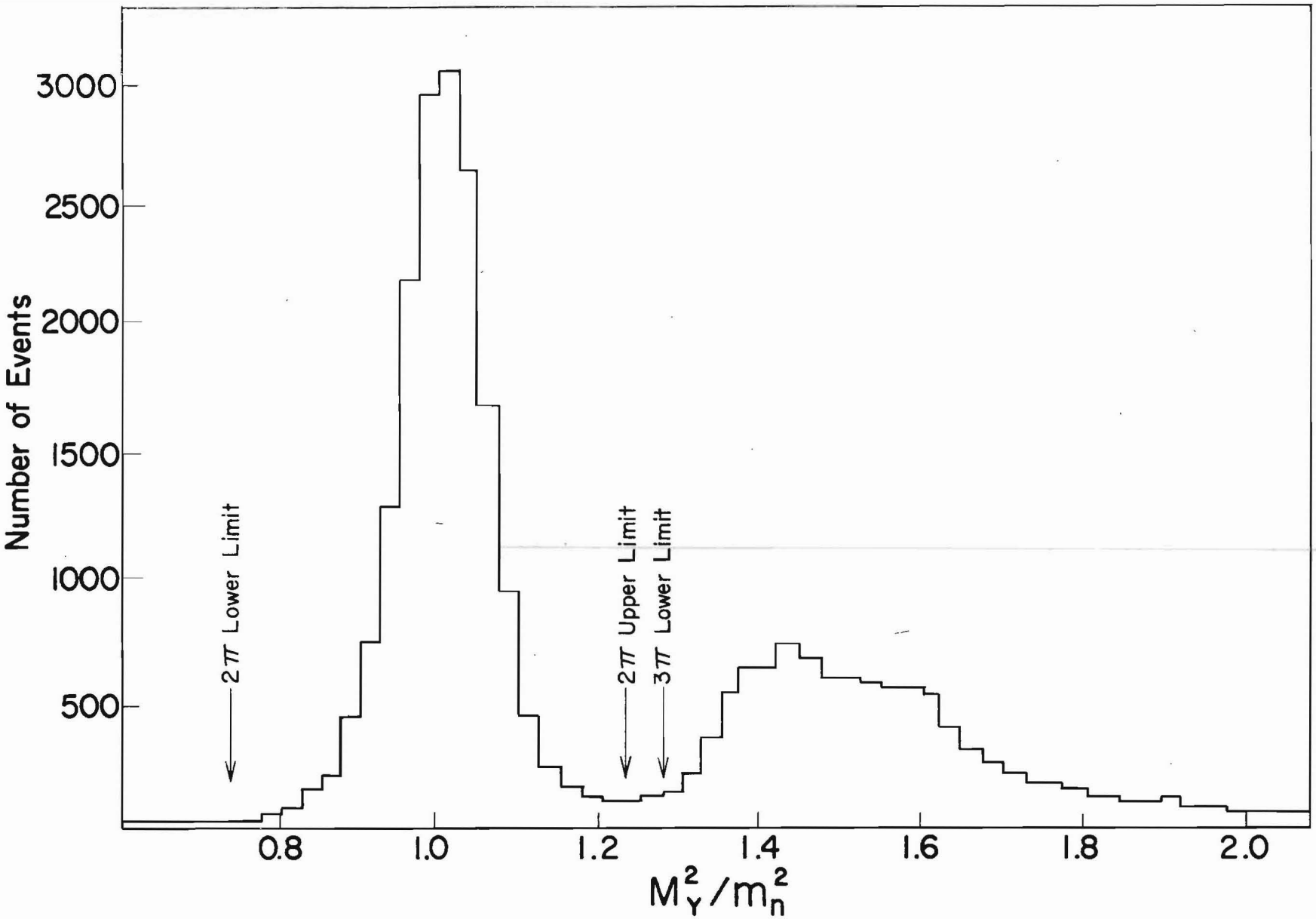
Number of Events
3000
2500
2000
1500
1000
500
2π Lower Limit
2π Upper Limit
3π Lower Limit
0.8
1.0
1.2
1.4
1.6
1.8
2.0
M_Y^2/m_n^2

Fig. 1

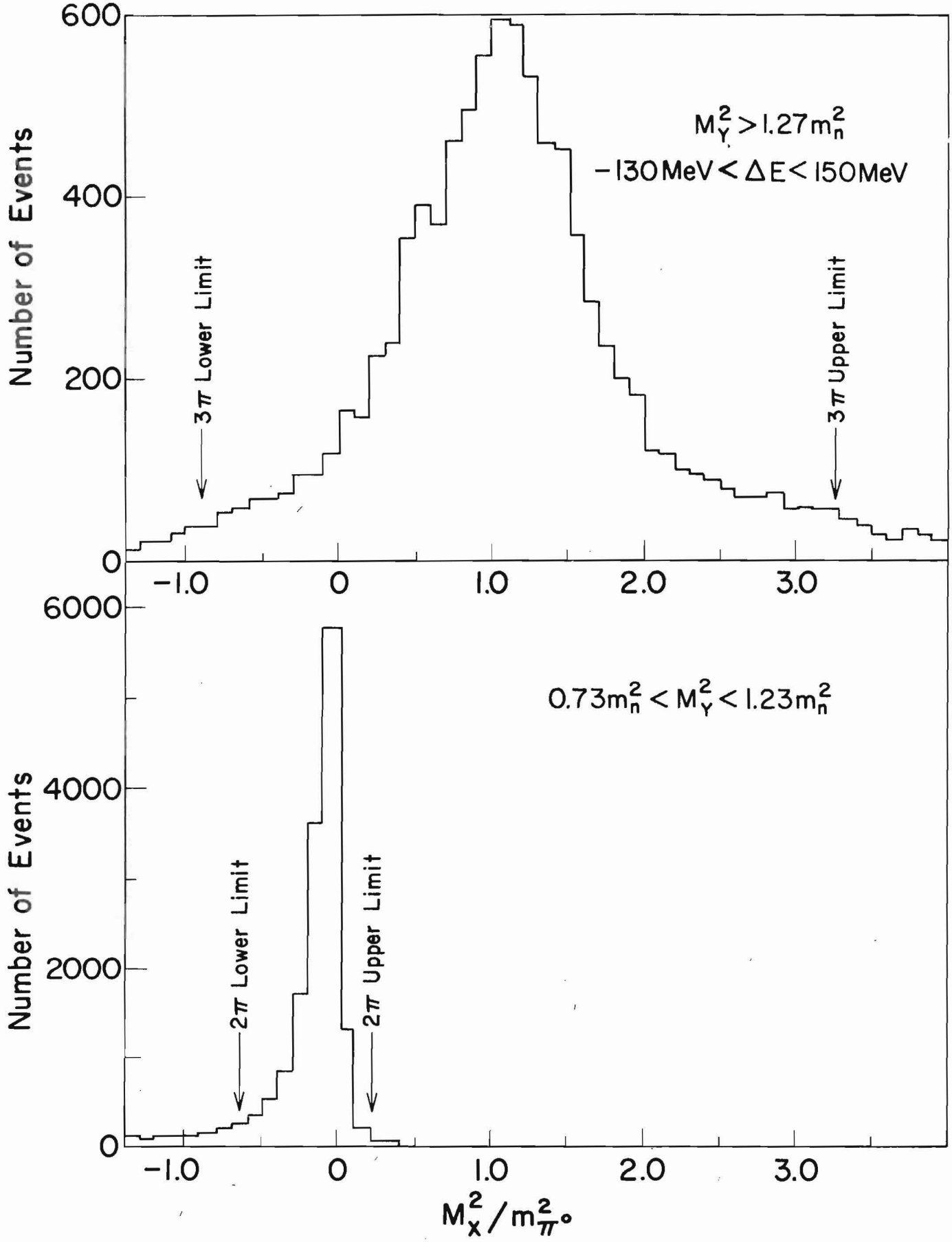
600
400
200
0
Number of Events
$M_Y^2 > 1.27 m_n^2$
$-130\,MeV < \Delta E < 150\,MeV$
3π Lower Limit
3π Upper Limit
-1.0
0
1.0
2.0
3.0
6000
4000
2000
0
Number of Events
$0.73 m_n^2 < M_Y^2 < 1.23 m_n^2$
2π Lower Limit
2π Upper Limit
-1.0
0
1.0
2.0
3.0
$M_X^2 / m_{\pi^0}^2$

Fig. 13

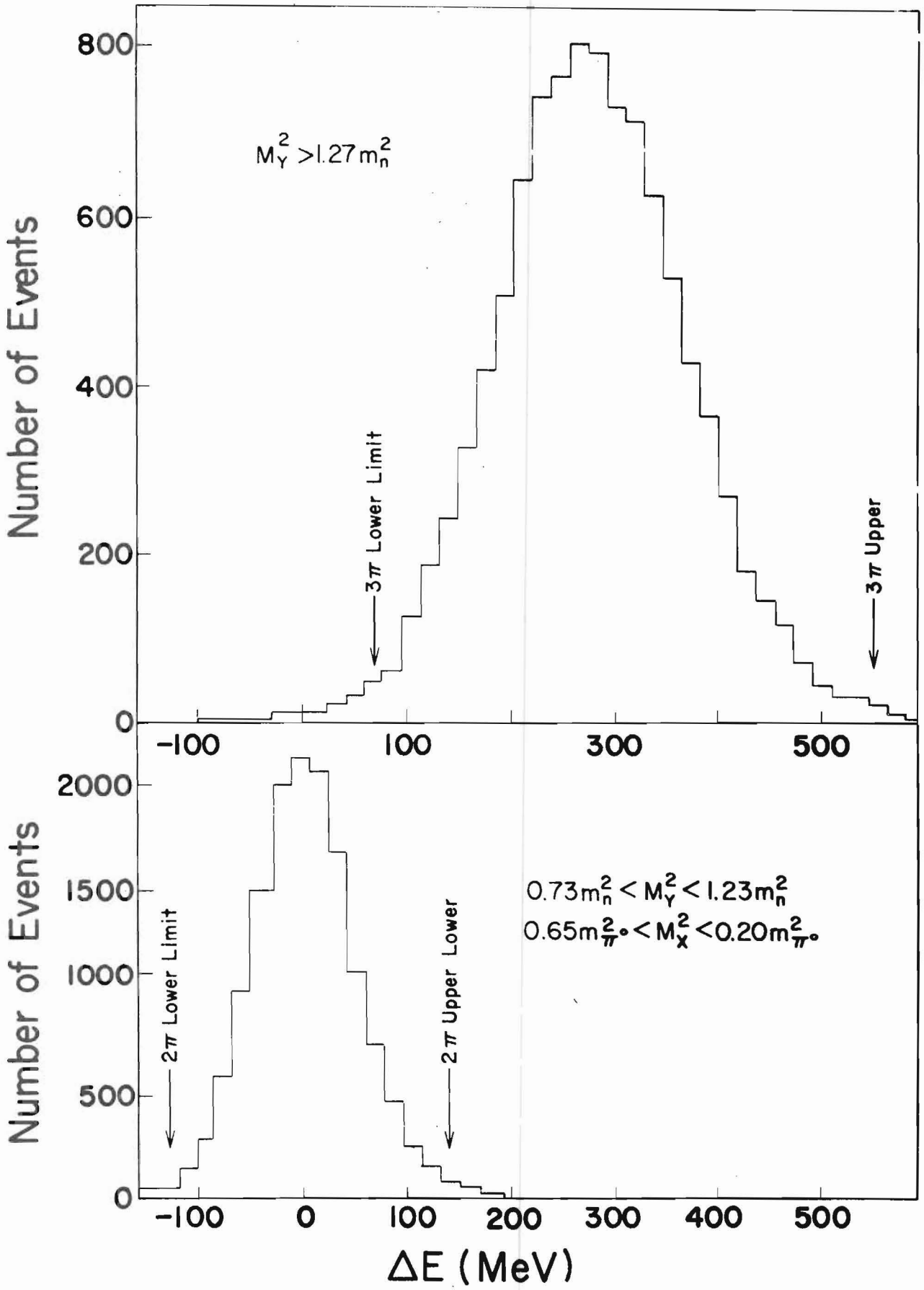
800
600
400
200
0
Number of Events
$M_Y^2 > 1.27 m_n^2$
3π Lower Limit
3π Upper
-100
100
300
500
2000
1500
1000
500
0
Number of Events
2π Lower Limit
2π Upper Lower
$0.73 m_n^2 < M_Y^2 < 1.23 m_n^2$
$0.65 m_{\pi^0}^2 < M_X^2 < 0.20 m_{\pi^0}^2$
-100
0
100
200
300
400
500
ΔE (MeV)

Fig. 14

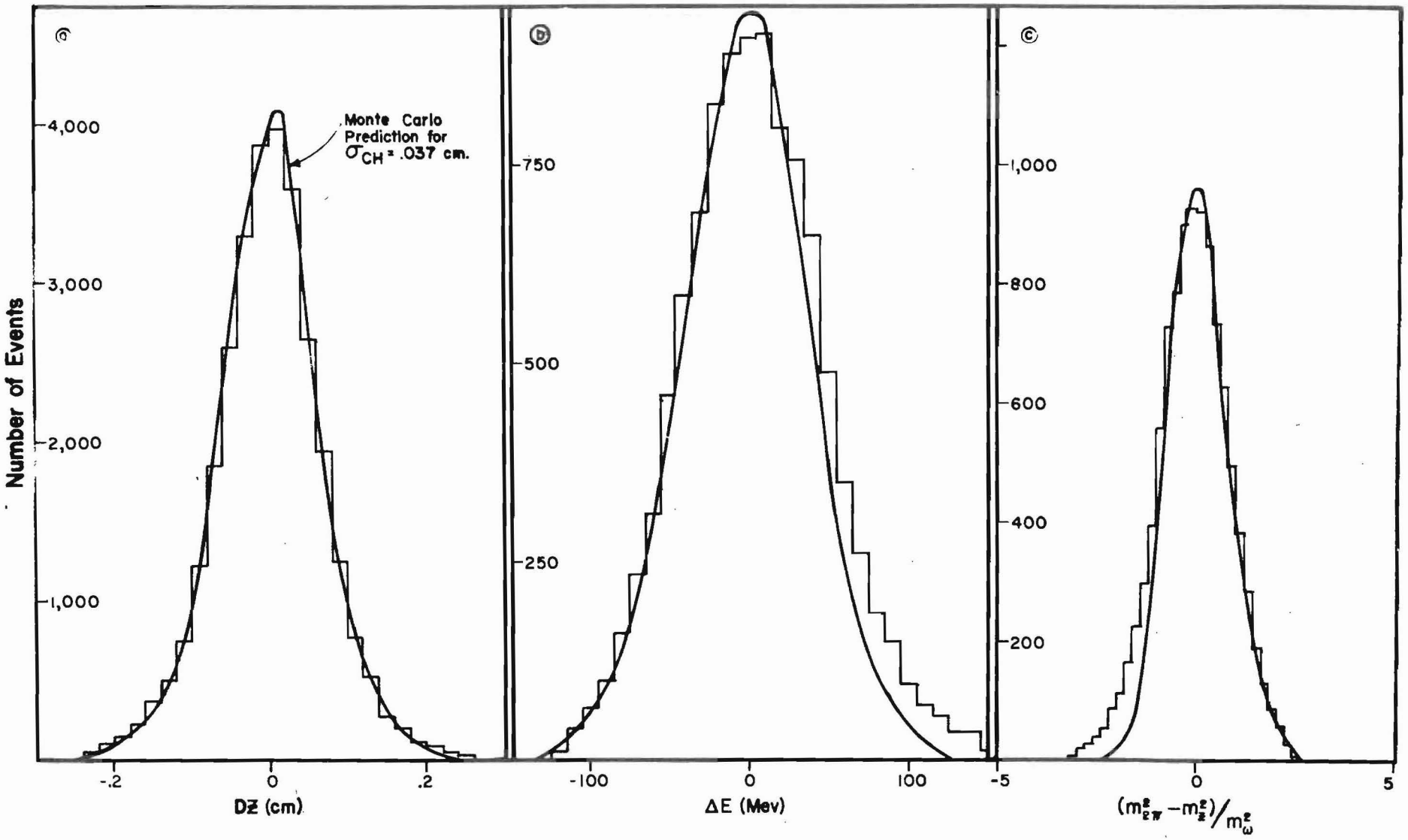
Number of Events
4,000
3,000
2,000
1,000
Monte Carlo Prediction for σ_{CH} = .037 cm.
-.2
0
.2
Dz (cm)
750
500
250
-100
0
100
ΔE (Mev)
1,000
800
600
400
200
-5
0
5
$(m_{2\pi}^2 - m_\pi^2)/m_\omega^2$

Fig. 15

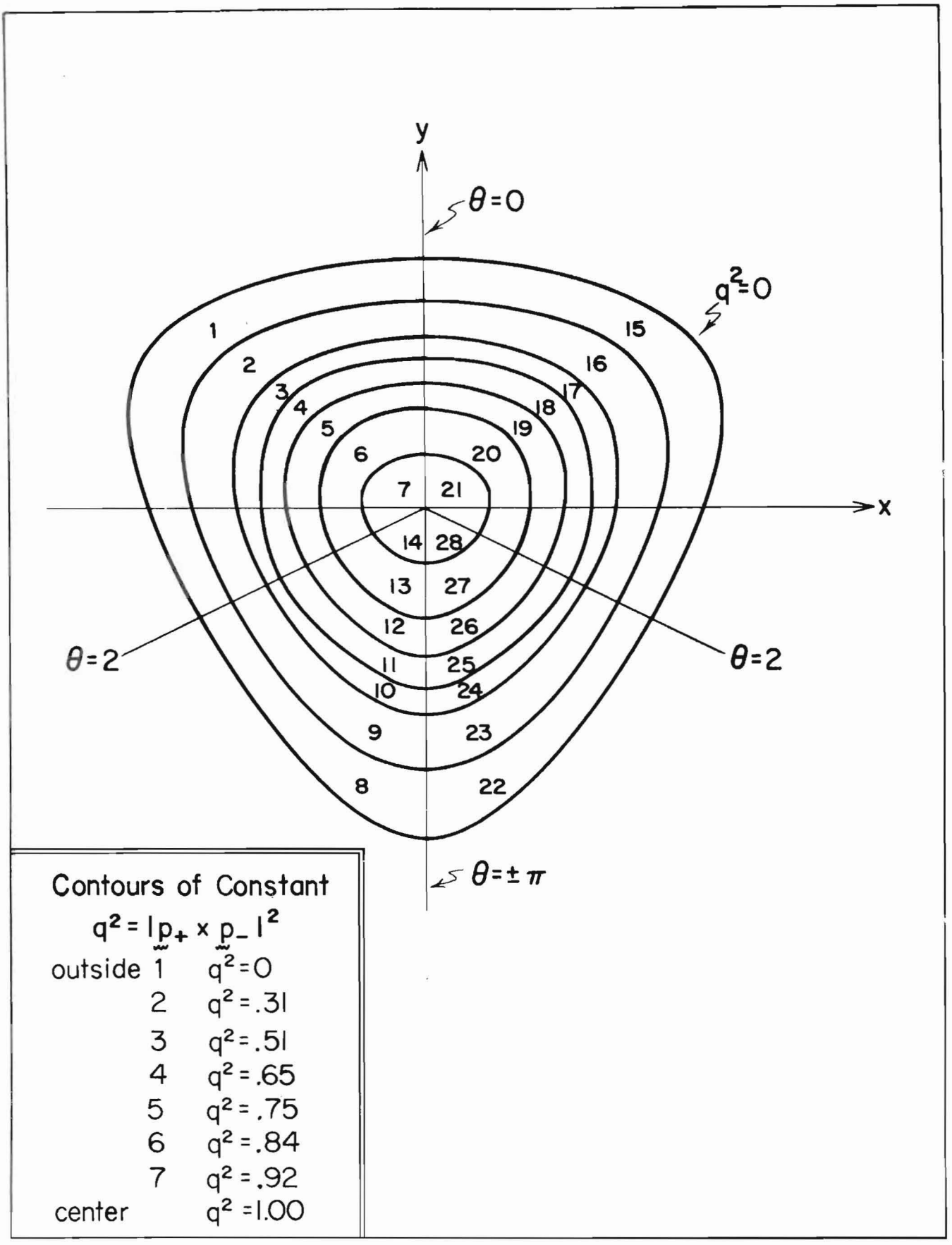

Contours of Constant

$q^2 = |\underset{\sim}{p}_+ \times \underset{\sim}{p}_-|^2$

outside	1	$q^2 = 0$
	2	$q^2 = .31$
	3	$q^2 = .51$
	4	$q^2 = .65$
	5	$q^2 = .75$
	6	$q^2 = .84$
	7	$q^2 = .92$
center		$q^2 = 1.00$

Fig. 16

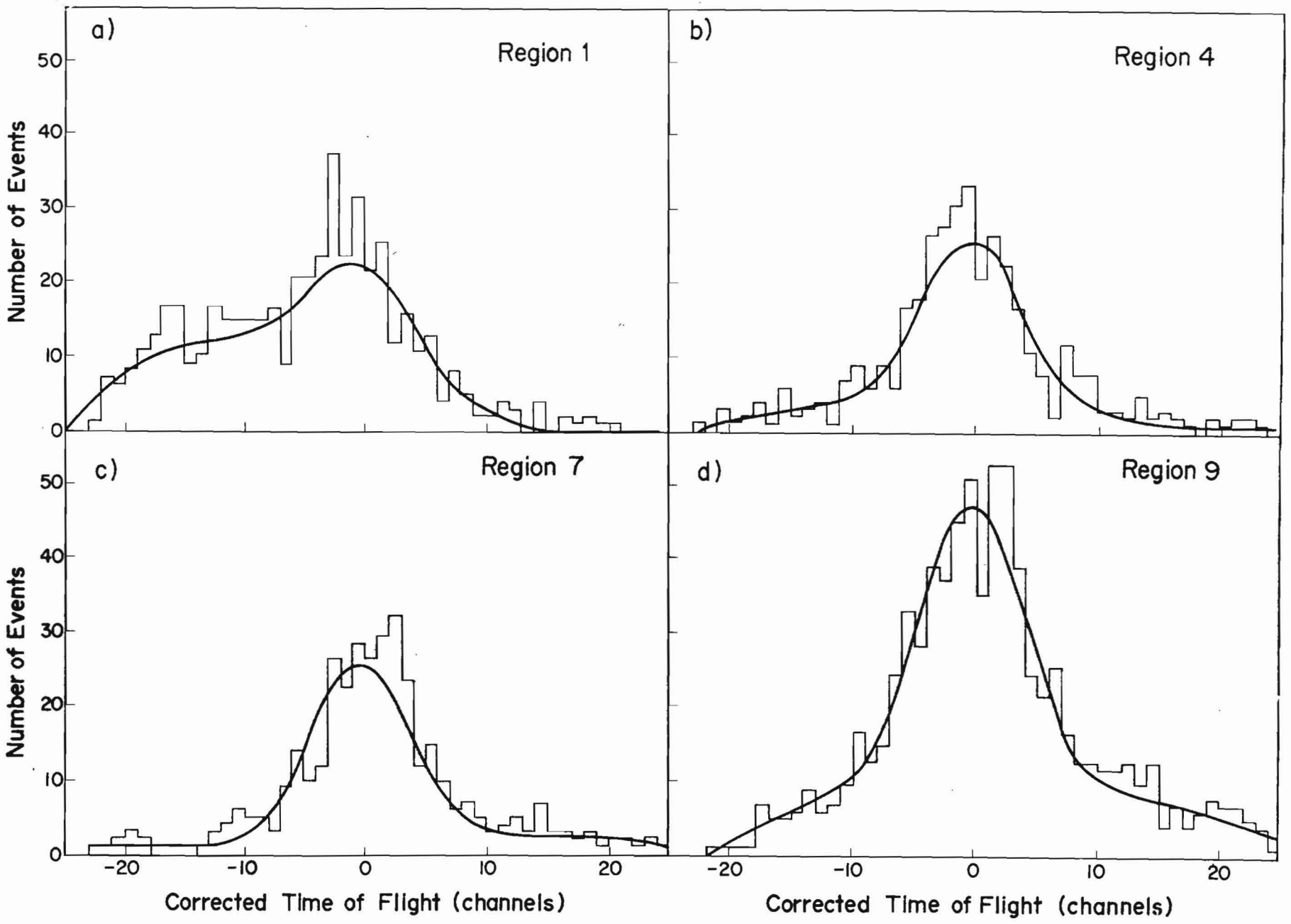
a)
Region 1
b)
Region 4
c)
Region 7
d)
Region 9
Number of Events
Number of Events
0
10
20
30
40
50
-20
-10
0
10
20
Corrected Time of Flight (channels)
Corrected Time of Flight (channels)

Fig. 17

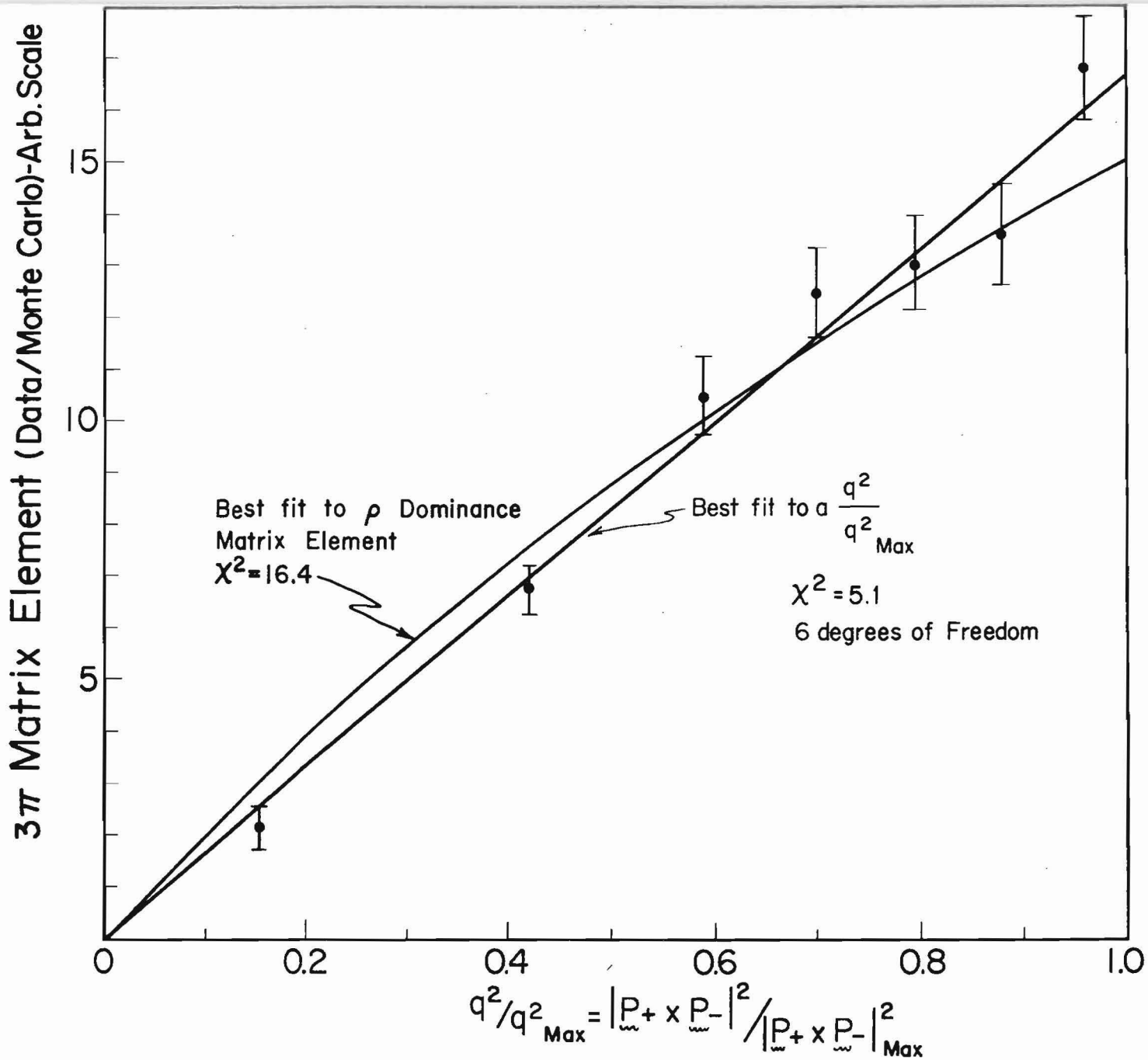
3π Matrix Element (Data/Monte Carlo)-Arb. Scale
15
10
5
0
0.2
0.4
0.6
0.8
1.0
Best fit to ρ Dominance Matrix Element
$\chi^2 = 16.4$
Best fit to a $\frac{q^2}{q^2_{Max}}$
$\chi^2 = 5.1$
6 degrees of Freedom
$q^2/q^2_{Max} = |\underset{\sim}{P}_+ \times \underset{\sim}{P}_-|^2 / |\underset{\sim}{P}_+ \times \underset{\sim}{P}_-|^2_{Max}$

Fig. 18

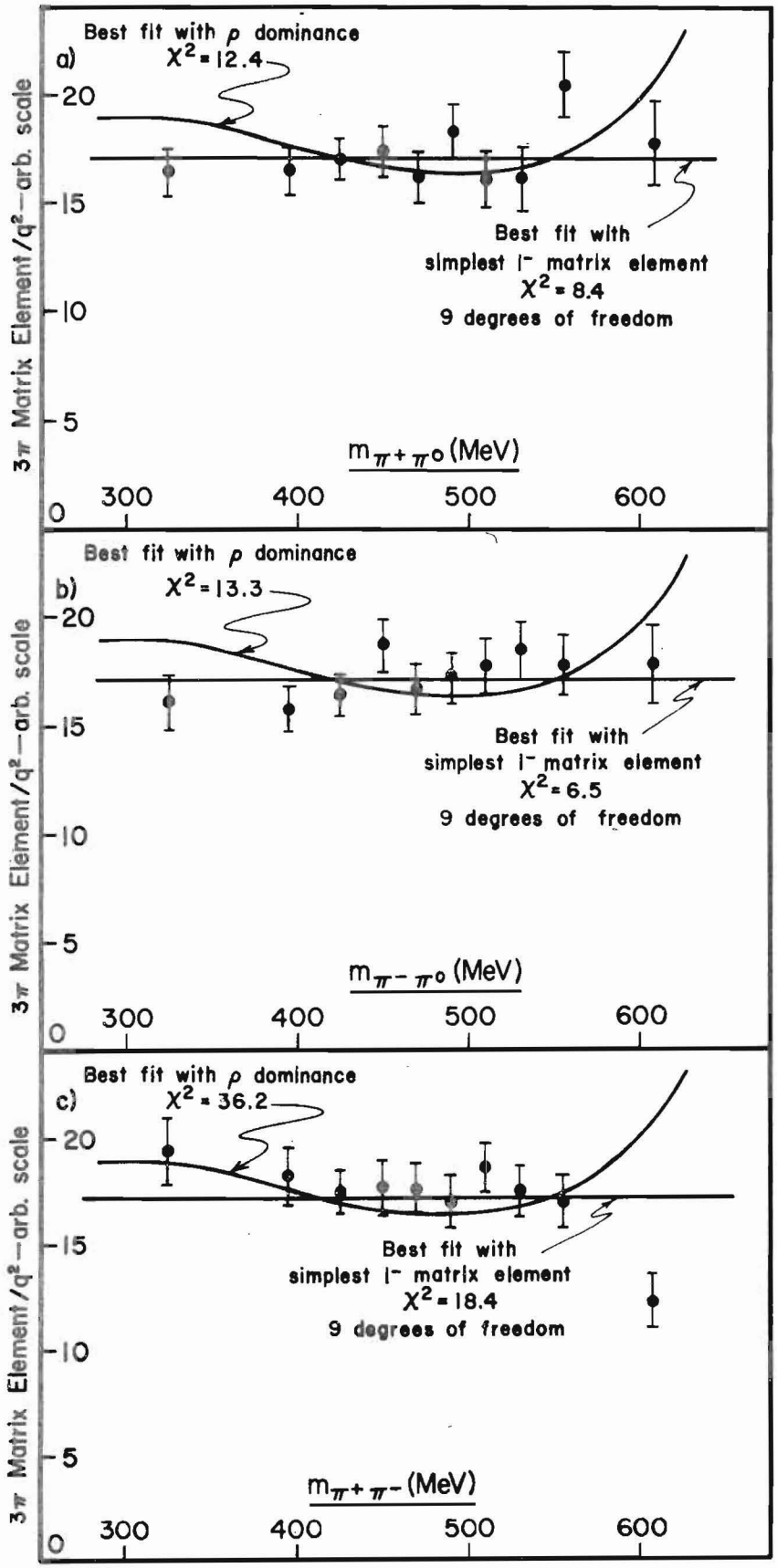
Best fit with ρ dominance
a)
$\chi^2 = 12.4$
Best fit with
simplest 1^- matrix element
$\chi^2 = 8.4$
9 degrees of freedom
$m_{\pi^+\pi^0}$ (MeV)
3π Matrix Element/q^2—arb. scale
Best fit with ρ dominance
b)
$\chi^2 = 13.3$
Best fit with
simplest 1^- matrix element
$\chi^2 = 6.5$
9 degrees of freedom
$m_{\pi^-\pi^0}$ (MeV)
3π Matrix Element/q^2—arb. scale
Best fit with ρ dominance
c)
$\chi^2 = 36.2$
Best fit with
simplest 1^- matrix element
$\chi^2 = 18.4$
9 degrees of freedom
$m_{\pi^+\pi^-}$ (MeV)
3π Matrix Element/q^2—arb. scale

Fig. 19

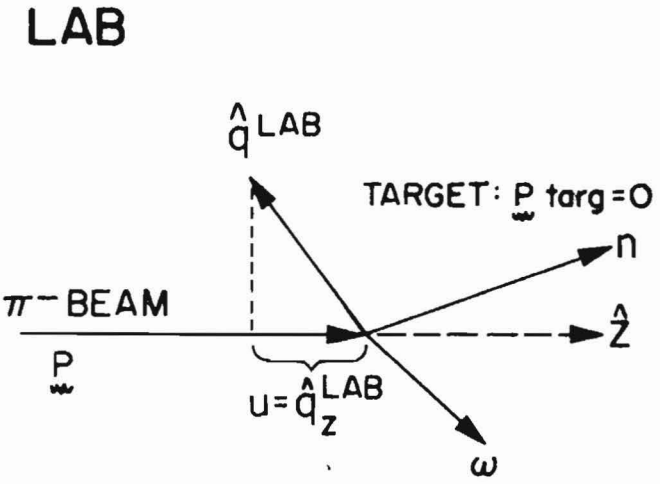
LAB
$\hat{q}^{LAB}$
TARGET: $\underset{\sim}{P}$ targ = 0
n
π^- BEAM
$\hat{Z}$
$\underset{\sim}{P}$
$u = \hat{q}_z^{LAB}$
ω

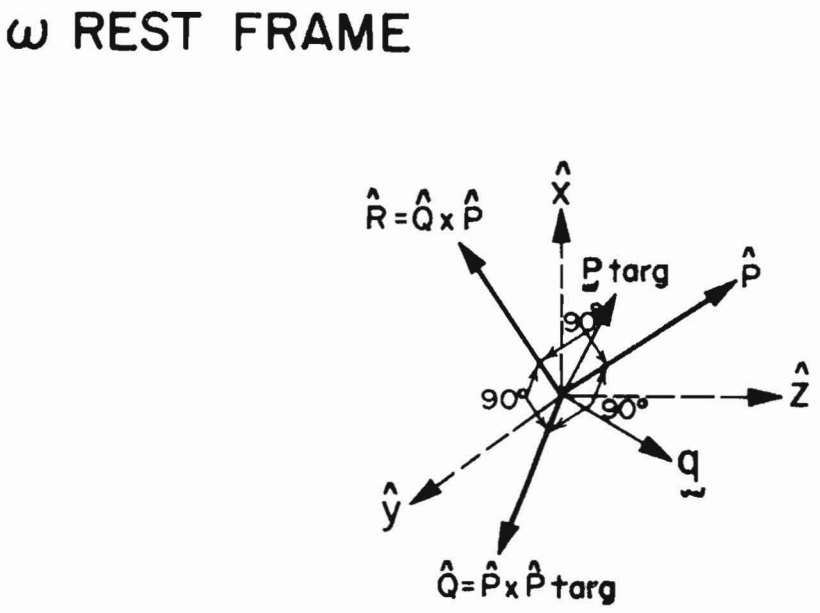
ω REST FRAME
$\hat{R} = \hat{Q} \times \hat{P}$
$\hat{X}$
$\underset{\sim}{P}$ targ
$\hat{P}$
90°
90°
90°
$\hat{Z}$
$\underset{\sim}{q}$
$\hat{y}$
$\hat{Q} = \hat{P} \times \hat{P}$ targ

Fig. 20

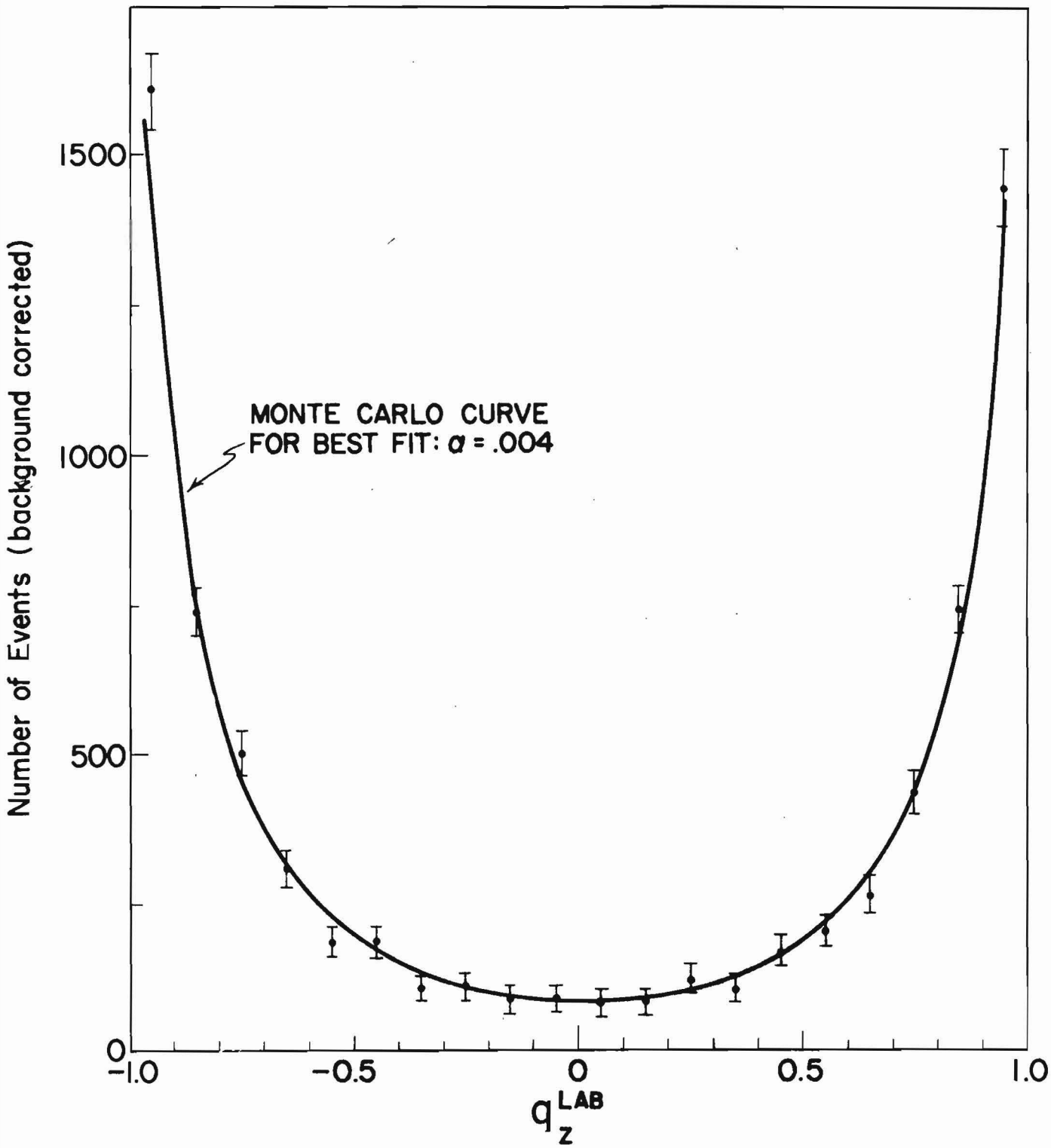
1500
1000
500
0
Number of Events (background corrected)
MONTE CARLO CURVE
FOR BEST FIT: α = .004
-1.0
-0.5
0
0.5
1.0
q_z^{LAB}

Fig. 21

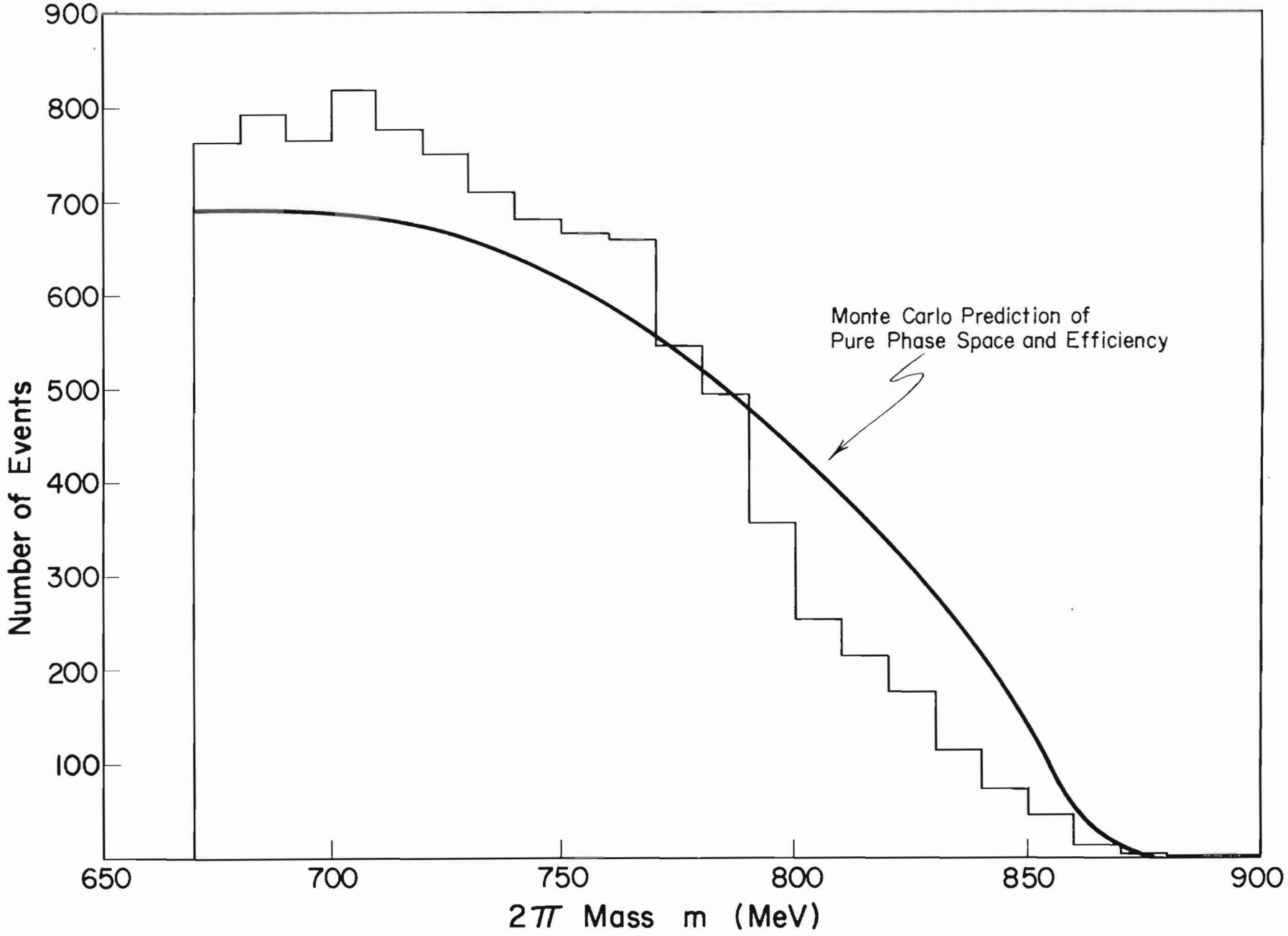
900
800
700
600
500
400
300
200
100
Number of Events
650
700
750
800
850
900
2π Mass m (MeV)
Monte Carlo Prediction of
Pure Phase Space and Efficiency

Fig. 22

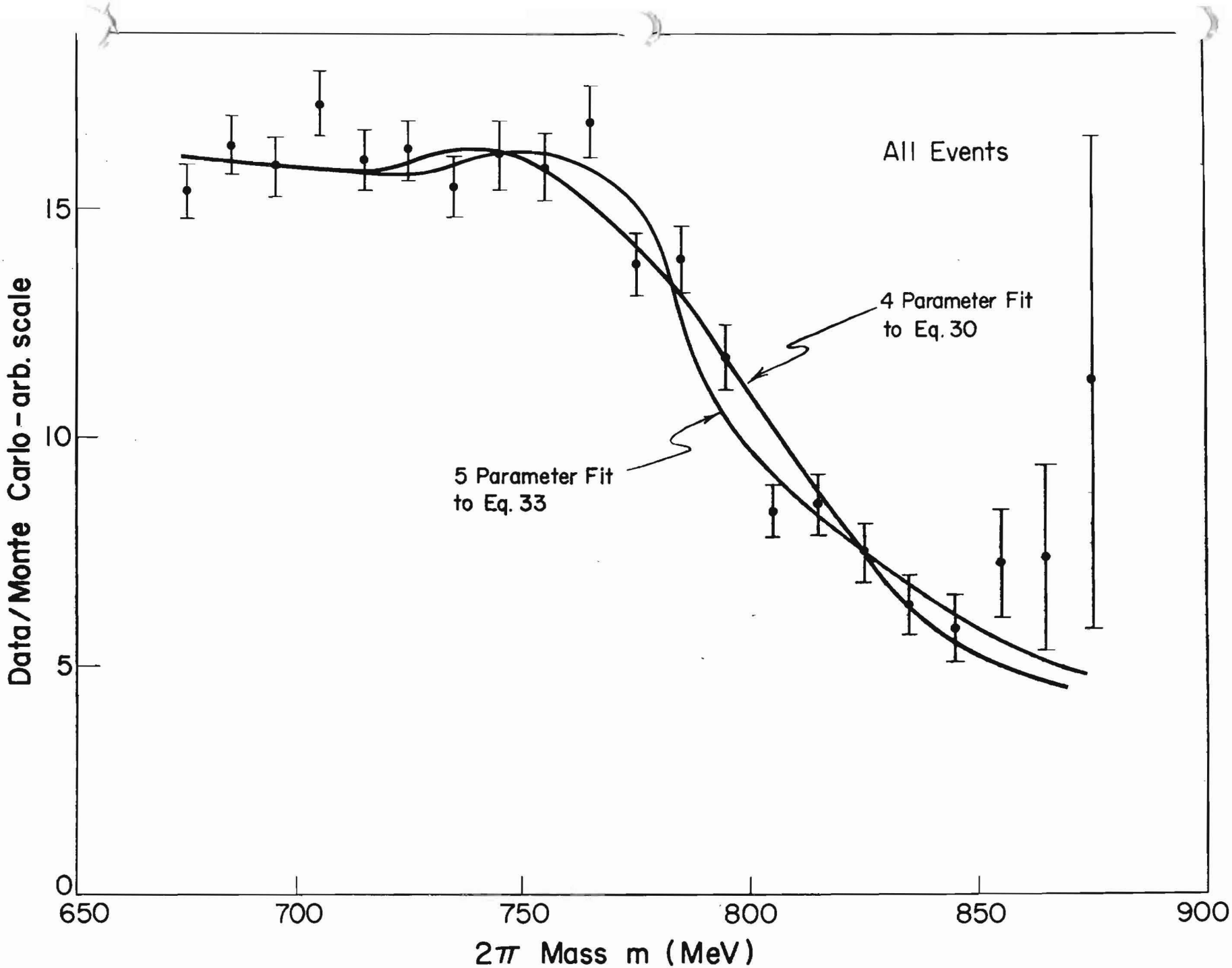
All Events
4 Parameter Fit
to Eq. 30
5 Parameter Fit
to Eq. 33
Data/Monte Carlo-arb. scale
0
5
10
15
650
700
750
800
850
900
2π Mass m (MeV)

Fig. 23

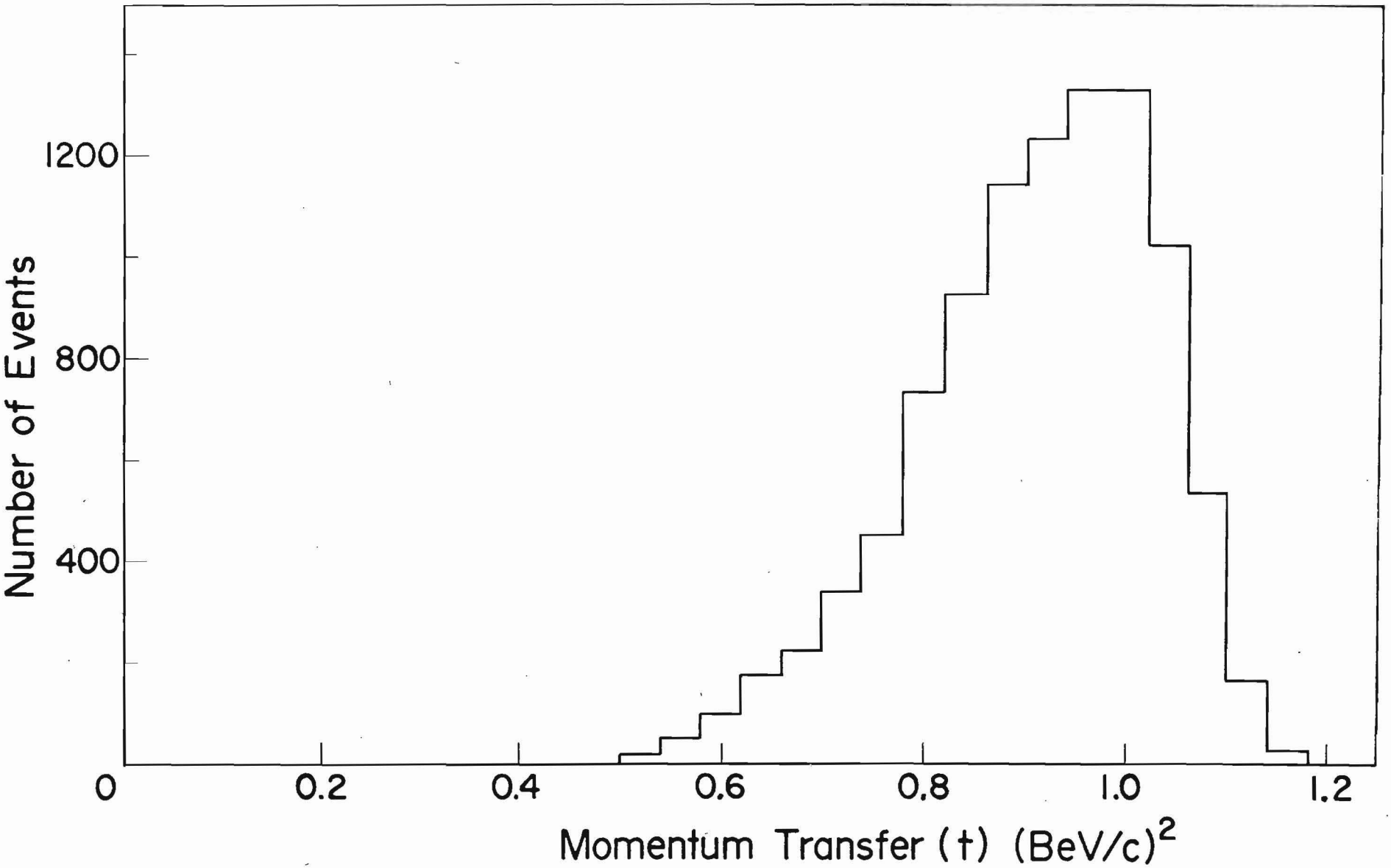
Number of Events
1200
800
400
0
0.2
0.4
0.6
0.8
1.0
1.2
Momentum Transfer (t) (BeV/c)^2

Fig. 24

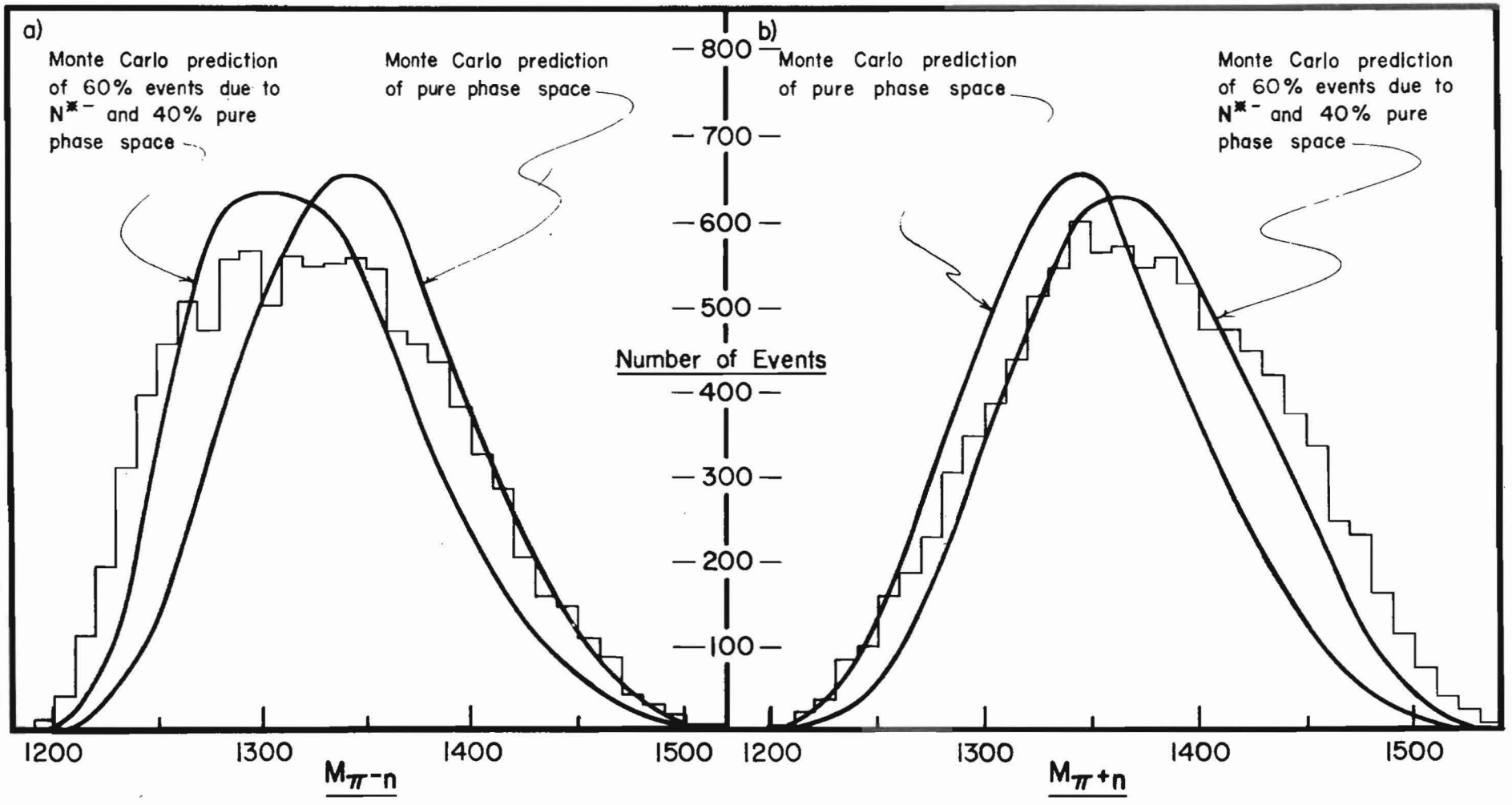
a)
Monte Carlo prediction of 60% events due to N*⁻ and 40% pure phase space
Monte Carlo prediction of pure phase space
b)
Monte Carlo prediction of pure phase space
Monte Carlo prediction of 60% events due to N*⁻ and 40% pure phase space
800
700
600
500
400
300
200
100
Number of Events
1200
1300
1400
1500
$M_{\pi^- n}$
1200
1300
1400
1500
$M_{\pi^+ n}$

Fig. 25

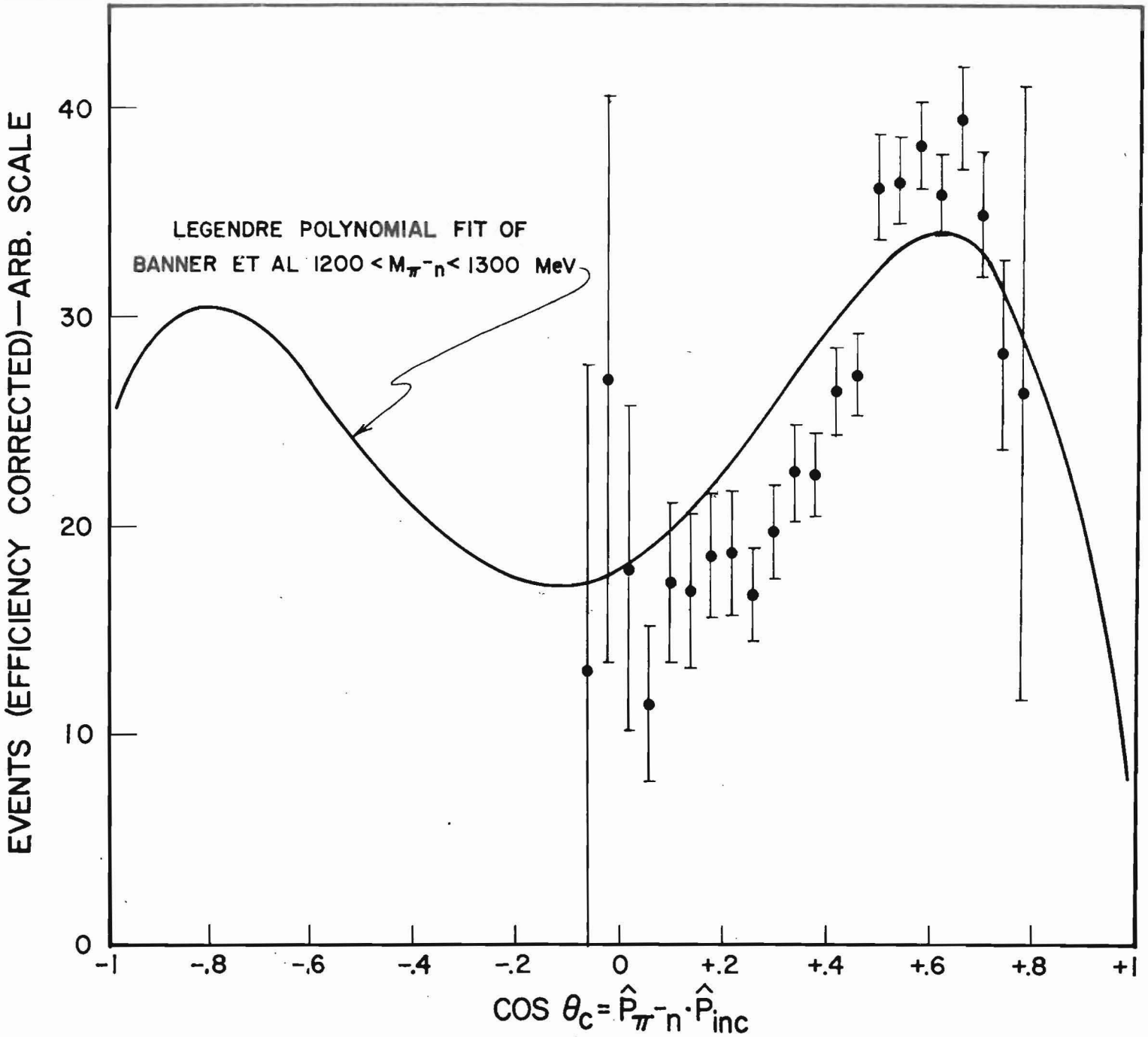
EVENTS (EFFICIENCY CORRECTED)—ARB. SCALE
40
30
20
10
0
LEGENDRE POLYNOMIAL FIT OF
BANNER ET AL 1200 < $M_{\pi^- n}$ < 1300 MeV
-1
-.8
-.6
-.4
-.2
0
+.2
+.4
+.6
+.8
+1
COS $\theta_c = \hat{P}_{\pi^- n} \cdot \hat{P}_{inc}$

Fi 26

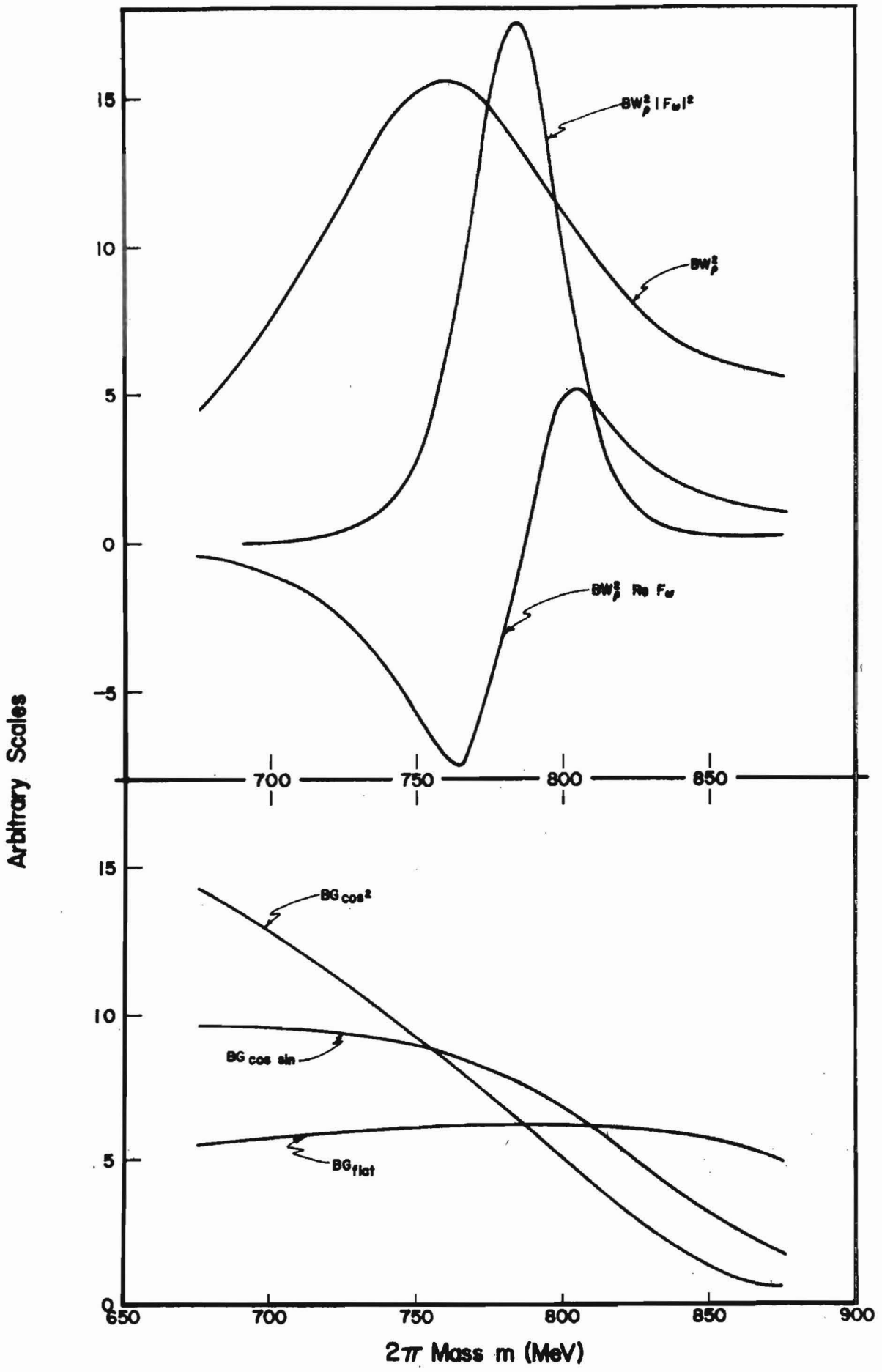
15
10
5
0
-5
$BW_\rho^2 |F_\omega|^2$
BW_ρ^2
BW_ρ^2 Re F_ω
700
750
800
850
Arbitrary Scales
15
10
5
0
$BG_{\cos^2}$
$BG_{\cos \sin}$
BG_{flat}
650
700
750
800
850
900
2π Mass m (MeV)

Fig. 27

$M^2_{\pi^-n}/M^2_{N^*}$	.72–.80	.80–.88	.88–.96	.96–1.04	1.04–1.12	1.12–1.20	1.20–1.28	1.28–1.36	1.36–1.44	1.44–1.52	1.52–1.60	1.60–1.68	1.68–1.76	1.76–1.84
1.54–1.62	303 ±163	91 ±98												
1.46–1.54	177 ± 63	188 ±87	182 ±121	80 ±88										
1.38–1.46	95 ± 23	105 ±29	137 ±43	149 ±55	194 ±90	400 ±327								
1.30–1.38	121 ± 19	135 ±23	112 ±23	117 ±30	103 ±35	380 ±125	400 ±242	500 ±456						
1.22–1.30	89 ± 12	88 ±13	134 ±20	143 ±23	174 ±33	176 ±41	189 ±57	185 ± 74	148 ±91					
1.14–1.22	85 ± 10	103 ±12	118 ±14	79 ±12	118 ±18	122 ±19	117 ±24	154 ± 37	143 ±44	209 ±94		250 ±354		
1.06–1.14	98 ± 10	102 ±10	103 ±11	115 ±12	134 ±16	111 ±14	114 ±16	80 ± 16	110 ±23	80 ±26	80 ±35	375 ±342		
.98–1.06	89 ± 9	108 ±10	103 ± 9	101 ±10	117 ±12	106 ±12	94 ±11	84 ± 12	53 ±10	71 ±17	32 ±11	50 ± 21		
1360 MeV	90 ± 9	112 ±10	106 ± 9	114 ±10	96 ± 9	103 ±10	121 ±12	87 ± 11	72 ±11	35 ± 7	35 ± 8	30 ± 11	25 ±19	50 ±55
1300 MeV	101 ± 9	97 ± 9	121 ±11	115 ±10	101 ±10	119 ±12	97 ± 9	90 ± 10	50 ± 7	62 ±10	36 ± 8	46 ± 12	94 ±37	125 ±153
	114 ± 11	122 ±12	154 ±14	132 ±12	101 ±11	126 ±12	111 ±11	90 ± 11	64 ± 9	54 ± 8	65 ±11	57 ± 14	105 ±44	167 ±152
	181 ± 17	193 ±19	169 ±17	181 ±18	181 ±17	164 ±18	150 ±17	137 ± 16	81 ±12	73 ±11	88 ±15	85 ± 22	62 ±40	
	305 ± 30	304 ±31	308 ±32	250 ±28	292 ±34	244 ±29	231 ±29	153 ±25	171 ±31	135 ±26	85 ±23	78 ±40	62 ±70	
	658 ± 78	483 ±57	533 ±71	381 ±56	562 ±93	428 ±69	269 ±54	242 ±58	250 ±88	212 ±87	500 ±612			
	541 ±117	825 ±179	656 ±158	878 ±264	406 ±111	510 ±221	444 ±339							
	1000 ±645													

$M^2_{\pi\pi}/M^2_{\omega}$

Fig. 2

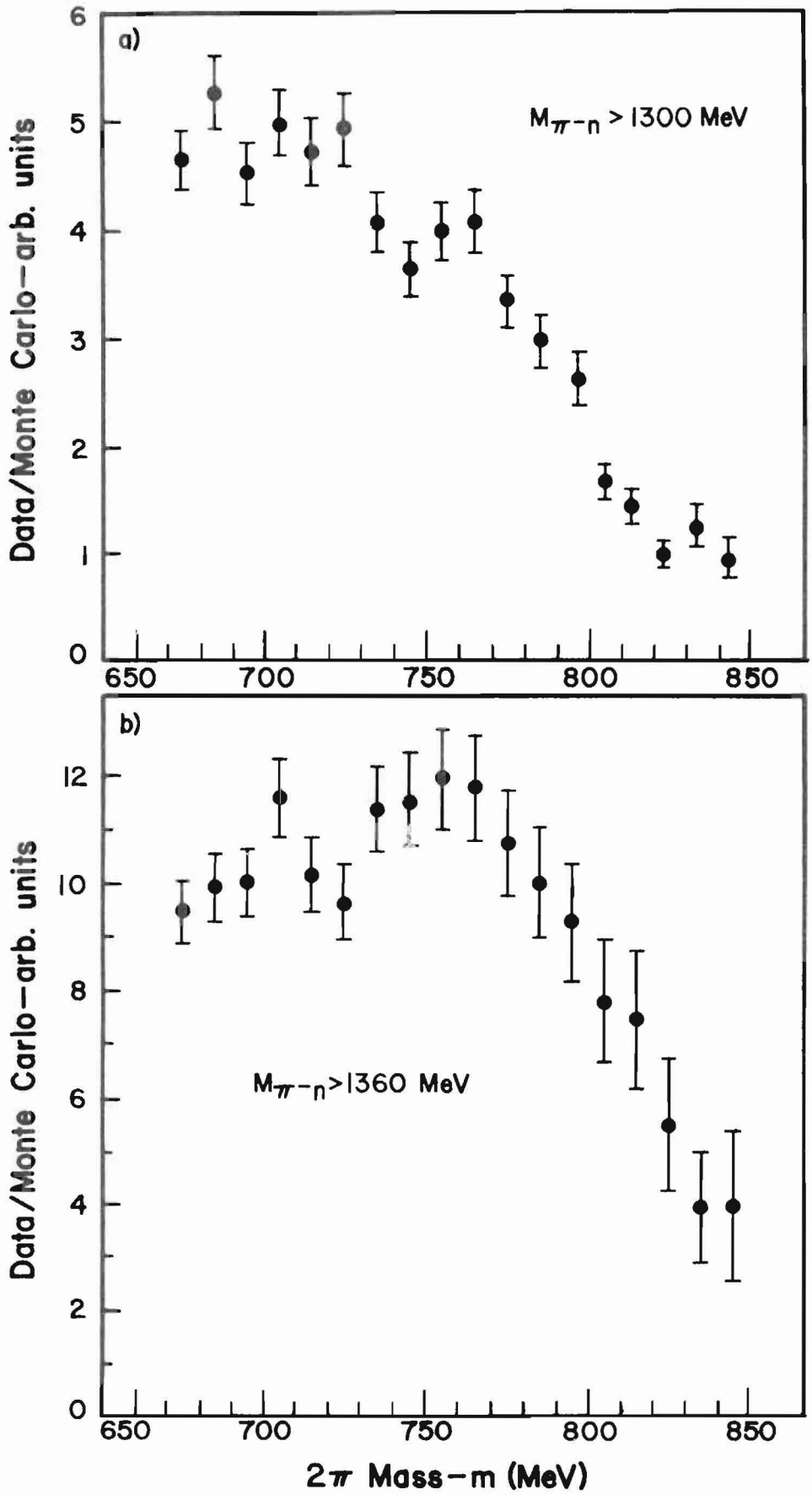
a)
$M_{\pi-n}$ > 1300 MeV
Data/Monte Carlo—arb. units
0
1
2
3
4
5
6
650
700
750
800
850
b)
$M_{\pi-n}$>1360 MeV
Data/Monte Carlo—arb. units
0
2
4
6
8
10
12
650
700
750
800
850
2π Mass—m (MeV)

Fig. 29

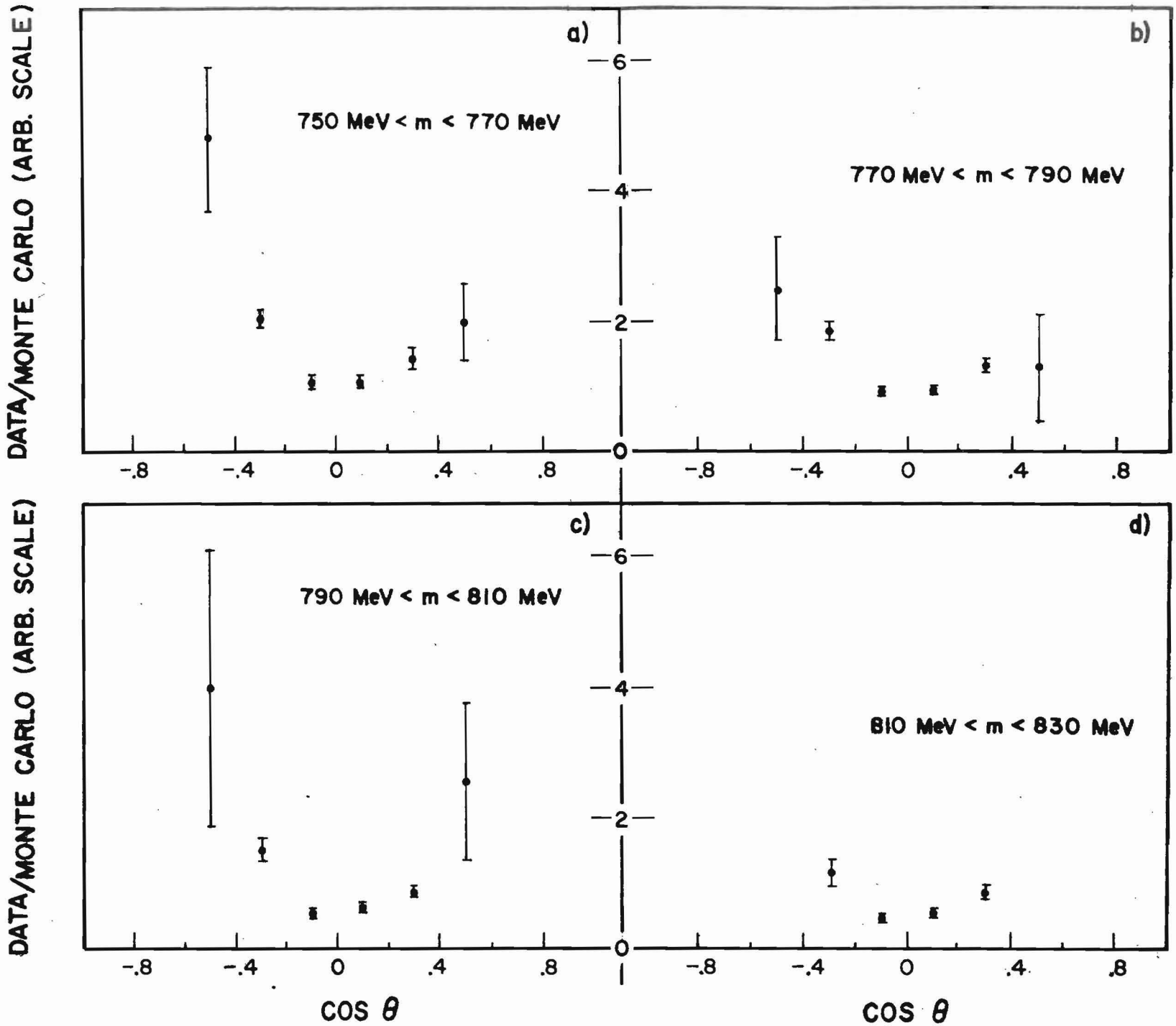
a)
b)
c)
d)
750 MeV < m < 770 MeV
770 MeV < m < 790 MeV
790 MeV < m < 810 MeV
810 MeV < m < 830 MeV
DATA/MONTE CARLO (ARB. SCALE)
DATA/MONTE CARLO (ARB. SCALE)
0
2
4
6
-.8
-.4
0
.4
.8
COS θ
COS θ

Fig. 30

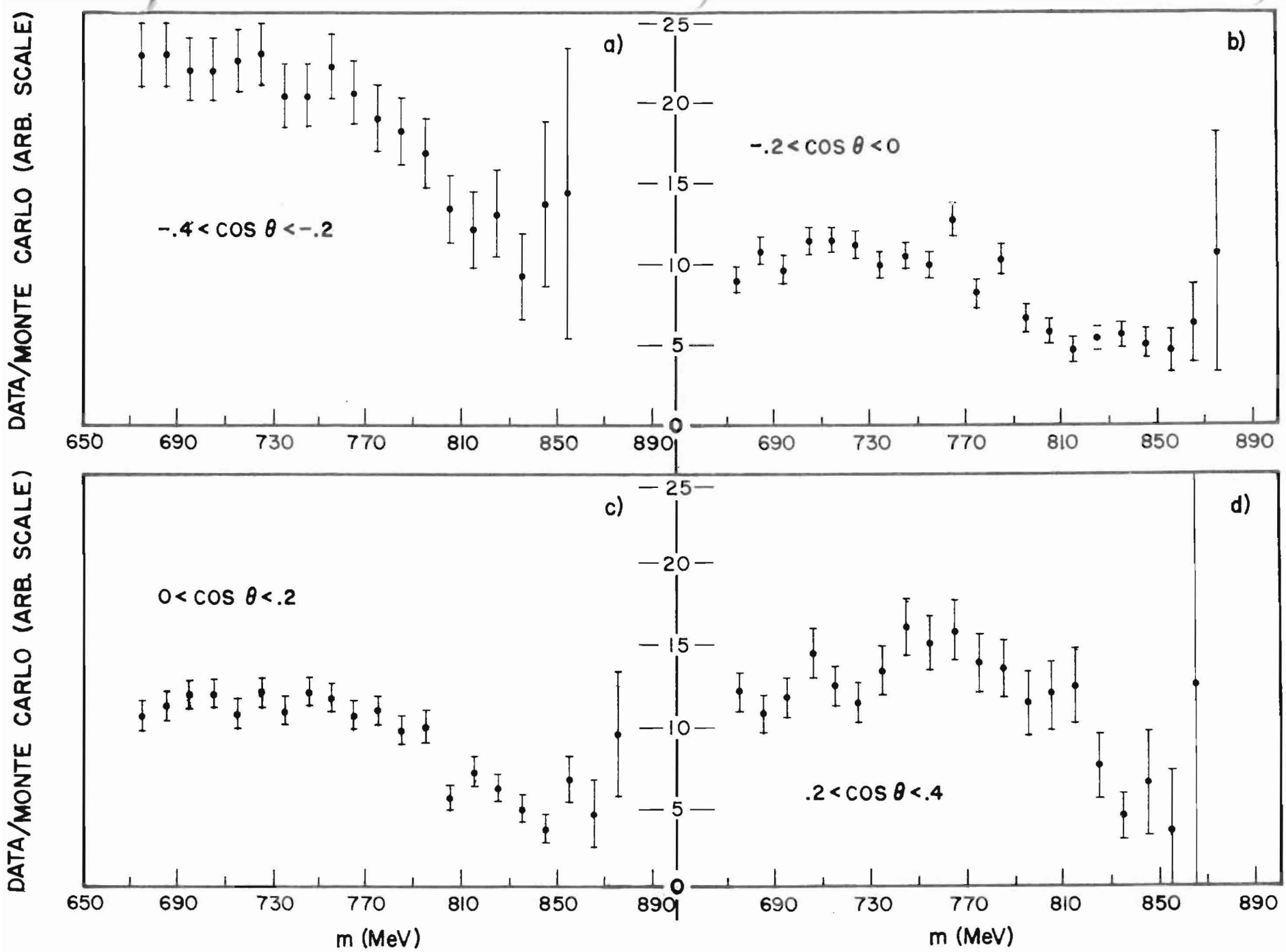
DATA/MONTE CARLO (ARB. SCALE)
a)
b)
c)
d)
-.4 < cos θ < -.2
-.2 < cos θ < 0
0 < cos θ < .2
.2 < cos θ < .4
0
5
10
15
20
25
650
690
730
770
810
850
890
m (MeV)

Fig. 31

MOMENTUM TRANSFER $(GeV/c)^2$	680	700	720	740	760	780	800	820	840	860	880	900
.5							1	3	2	5	15	24	37	20	13	6		1
.6									4	10	13	36	44	90	102	78	37	27	3		1	
.7					2	9	20	27	83	144	241	228	175	113	59	15	3					
.8	1	6	14	38	72	138	218	336	435	485	363	236	91	34	8	1						
.9	111	193	314	426	520	526	463	318	204	87	28	4										
1.0	546	532	427	353	183	86	20	7														
1.1	105	63	10	2	1																	
1.2																						

m (MeV)

Fig. 32